**Title**
Survival of the Resilient: An Exploration of Tipping Cascades with Positive Change



**Author**
Mallela, Abhishek

**Publication Date**
2022

Peer reviewed|Thesis/dissertation

**Survival of the Resilient: An Exploration of Tipping Cascades with Positive Change**

By

ABHISHEK MALLELA
DISSERTATION

Submitted in partial satisfaction of the requirements for the degree of

DOCTOR OF PHILOSOPHY

in

Applied Mathematics

in the

OFFICE OF GRADUATE STUDIES

of the

UNIVERSITY OF CALIFORNIA

DAVIS

Approved:

---

Alan Hastings, Chair

---

Louis Botsford

---

Robert Guy

Committee in Charge

2022

To my mother and father, who have always supported me unconditionally.

# Contents

Survival of the Resilient: An Exploration of Tipping Cascades with Positive Change

**Abstract**

The most important global challenges in these uncertain times can be characterized by critical transitions – for instance, political instability, loss of biodiversity, and climate change. Critical transitions in complex systems, the sudden and abrupt changes that occur at tipping points when thresholds are passed, are at the heart of many different phenomena in ecology and evolution. How does noise-induced tipping impact the transition of a system between dynamic regimes? What are the roles of noise and network connectivity in the detection of early-warning signals? Can tipping be used to generate a positive cascade of behaviors? In this dissertation, I address all of these central questions in the context of a specific model system. First, I use a minimal, individual-based stochastic model to show how demographic stochasticity affects the dynamics of a cascade of tipping elements. Next, I develop a fast-slow stochastic model to explain the critical interplay between environmental noise and network connectivity in forecasting a tipping cascade. In the last chapter, I turn toward a useful ecological application of the work described thus far, in the context of invasive species eradication.

**Acknowledgments**

First and foremost, I am grateful for my thesis adviser, Alan Hastings. Simply put, I could not have asked for a kinder and more understanding advisor. I have learned a lot from him about communicating effectively. Alan has always supported me in my research interests and in many other ways.

I am also thankful for the helpful guidance and mentorship of my thesis committee members, Louis Botsford and Robert Guy, as well as the gracious presence of John Hunter and Eric Deeds on my qualifying exam committee. In particular, I will never forget Eric's enthusiasm and willingness to take me on as a research associate in his lab at the University of Kansas, which helped in shaping me into a collaborative and highly interdisciplinary researcher.

A special mention goes to Naveen Vaidya, my former research mentor at the University of Missouri-Kansas City. It is through his superb guidance that I was introduced to both infectious disease modeling and Suzanne Lenhart, a leading expert in optimal control theory.

I would also like to thank several wonderful people at UC Davis for ensuring no loss of continuity in my time here – during the unprecedented global COVID-19 pandemic – especially Tina Denena, Vanessa Bravo, Victoria Whistler, Sarah Driver, and my lab colleagues. I acknowledge as well the fantastic support that I received from UC Davis Graduate Studies for allowing me to conduct my teaching duties remotely over the past year.

I also thank my mother, father, and sister, who have supported me unconditionally throughout my life. I am truly blessed for my tight-knit, extended family for their constant support and encouragement throughout the years. They have believed in me every step of the way. Without them, I would be living in a very different world today.

CHAPTER 1

# Introduction

Nature is inherently complex and is comprised of complex systems. Given our rapidly growing understanding of life at microscopic scales, it seems surprising that our insights at the macroscopic level are remarkably limited. However, complex systems can exhibit a plethora of behaviors that make elucidation of phenomena extremely challenging. A classic example of such behavior, known as a regime shift, typically occurs in the vicinity of a tipping point in a complex dynamical system (Biggs et al., 2009; Hastings and Gross, 2012; Scheffer, 2009). The ubiquity of tipping points has been demonstrated both in a wide variety of fields and across many spatial scales, including the Dansgaard-Oeschger events during the last Ice Age and the switch-like, ultrasensitive response of the Goldbeter-Koshland loop at the molecular level (Cimatoribus et al., 2013; Gennaretti et al., 2014; Goldbeter and Koshland Jr, 1984; Lade et al., 2015; Lovejoy and Nobre, 2018; Mallela et al., 2020; Murray and King, 2012; Scheffer, 2010).

In ecology, a metapopulation that is slowly worsening in quality is a key instance of a spatially extended dynamical system that can have a tipping point. Mathematically, this system can be described by local growth via a strong Allee effect and is characterized by a saddle node bifurcation at the tipping point. Specifically, population densities exceeding the Allee threshold will persist, but those below the Allee threshold will face extinction (Courchamp et al., 2008). Allee effects have been demonstrated in a wide variety of biological systems (Brashares et al., 2010; Courchamp et al., 2006; Johnson et al., 2019; Kramer et al., 2009; Stoner and Ray-Culp, 2000; Tanaka et al., 2009). Mechanisms that induce an Allee effect, including anti-predator behavior and difficulties in mate finding, are well-understood (Courchamp et al., 2008; Hastings and Gross, 2012).

Another universal feature of physical systems is the presence of stochasticity, or noise (Horsthemke and Lefever, 1984). Noise can significantly impact physical processes over a wide range of scales. In biology, noise can present in sub-cellular processes, tissue dynamics, as well as at the population level (Tsimring, 2014). In population ecology, noise may be the result of environmental

factors or may occur due to demography (Coulson et al., 2004). Stochasticity manifests as either internal or external noise. Internal noise is inherent within the system and is caused by random interactions among discrete agents (e.g., noise due to randomly occurring births and deaths). This type of noise is typically represented with a master equation. External noise originates from a source other than the system itself and is often modeled using a stochastic process.

Although biological systems can be intractable, have several sources of uncertainty, and exist in high dimensions, considerable insight can often be gleaned from low-dimensional models that are formulated relatively simply (Hastings, 2013). A recurring theme among Chapters 2 to 4 of this dissertation is the principle of model parsimony. Another aspect that unifies the upcoming chapters relates to methodological advances in mathematical ecology. In Chapter 2, I investigate how demographic stochasticity, or internal noise, influences the dynamics of a cascade of tipping points. I consider a concrete and minimal individual-based stochastic model that exhibits noise-induced tipping. Parameterized with a strong Allee effect, this model operates in a regime with alternative, stable steady-states. From an ecological perspective, I explore the role of rescue effects in the system, whereby connected populations can rely on each other for survival. Then, using the theory of Markov chains, I effectively reduce the dimensionality of the system. Analysis of the reduced model illustrates the scenarios corresponding to a population recovering from the brink of extinction, as well as when a catastrophic collapse is inevitable. This work has been published in *Bulletin of Mathematical Biology* (Mallela and Hastings, 2021a).

In Chapter 3, I discuss the interplay between spatial coupling and multiplicative environmental stochasticity, a form of external noise, in an ecological tipping element. I develop a spatial model with two interacting populations that gradually approach a state of population extinction when the quality of their habitats is degraded. I initially formulate a simple spatial model, then introduce a version of the model with multiple timescales, and finally augment the system with noise. Using techniques from the theory of early-warning signals, I derive analytic expressions for leading indicators of extinction in each patch and assess their performance with simulations. Based on my findings, I conclude that this theoretical study can be applied to problems of biological control, including the control of invasive species. This work has also been published in *Bulletin of Mathematical Biology* (Mallela and Hastings, 2021b).

In Chapter 4, I address the degree of manageability of a non-native, invasive species from a standpoint of optimality. Two factors, in particular, play crucial roles in ensuing analyses: namely, the aspects of observability and detectability of the species. Here, I build upon the foundations of the model described in Chapter 2. The model for this study consists of a network of three interacting populations that live in separate locations, or patches, and are mutually connected through passive diffusion. For each possible network configuration, I adopt the individual-based modeling approach previously used in Chapter 2, to obtain a reduced Markov chain model. In the reduced model, each state is mapped to a combination of population thresholds. Then, I employ a powerful framework – known as a Partially Observable Markov Decision Process (POMDP), widely used in the fields of Operations Research and Artificial Intelligence – to answer my research questions in an ecological context. By analyzing the output of the POMDP, I describe the information that the manager of a system would need to achieve optimal outcomes. This work is currently under revision at *Journal of Theoretical Biology*.

CHAPTER 2

# The role of stochasticity in noise-induced tipping point cascades: a master equation approach

## 2.1. Abstract

Tipping points have been shown to be ubiquitous, both in models and empirically in a range of physical and biological systems. The question of how tipping points cascade through systems has been less explored and is an important one. A study of noise-induced tipping, in particular, could provide key insights into tipping cascades. Here, we considered a specific example of a simple model that could have cascading tipping points. This model consists of two interacting populations with underlying Allee effects and stochastic dynamics, in separate patches connected by dispersal, which can generate bistability. From an ecological standpoint, we look for rescue effects whereby one population can prevent the collapse of a second population. As a way to investigate the stochastic dynamics, we used an individual-based modeling approach rooted in chemical reaction network theory. Then, using continuous-time Markov chains and the theory of first-passage times, we essentially approximated, or emulated, the original high-dimensional model by a Markov chain with just four states, where each state corresponds to a combination of population thresholds. Analysis of this reduced model shows when the system is likely to recover, as well as when tipping cascades through the whole system.

## 2.2. Introduction

Many systems in nature can transition into a qualitatively distinct dynamic regime when a critical threshold is approached. The associated threshold of such a system, defined in the context of bifurcation theory, is the bifurcation point or tipping point of the system. Tipping points manifest in systems including lake eutrophication (ecology), social contagion (sociology), disease spread (epidemiology), epileptic seizures (physiology), stock market crashes (finance), and even

the earth system (Klose et al., 2020; Lenton, 2020; O'Regan, 2018; Scheffer, 2009; Scheffer et al., 2012). Tipping points arise in the presence of strongly self-amplifying (mathematically positive) feedbacks (Lenton, 2020). This characterization of tipping points is important in the sense that only sufficiently strong, self-propelling feedbacks are recognized.

A prime example of a tipping point is an ecological system with an Allee effect (Courchamp et al., 2008; Hastings and Gross, 2012; Johnson and Hastings, 2018; Vortkamp et al., 2020). Allee effects occur in populations with low abundances and are believed to be common in ecological systems (Courchamp et al., 2008; Drake and Kramer, 2011). In a population exhibiting an Allee effect, the per capita growth rate is a unimodal function of the population abundance with a global maximum. The sign of the growth rate at low population levels distinguishes a weak Allee effect from a strong one. In particular, a weak Allee effect does not result in a negative growth rate for small population sizes but its strong counterpart presents with a negative rate. Therefore, the existence of a strong Allee effect implies the existence of a critical threshold for survival. The possibility of alternative stable states in systems that are analogous to those with a strong Allee effect has significant implications at many levels, from the microscopic scale of budding yeast (Dai et al., 2012) to the macroscopic scale of tipping elements for the Earth system (Klose et al., 2020; Lenton, 2020).

In order to investigate how tipping points manifest in systems with a strong Allee effect, one needs to formulate a model that can exhibit this behavior. A fundamental question in this setting concerns the propagation of tipping points through an ecosystem consisting of multiple patches. To what extent are interacting populations interdependent and how is this relationship influenced by the parameters governing the model behavior? Stated more simply, how do tipping points cascade through systems?

A simple analysis considers multiple populations in a network that are connected by passive, symmetric diffusion. In this work, we study a model consisting of two populations to analyze how their dynamics are related, conditional on the quality of their internal environments. One case of interest is when one population has fallen below the Allee threshold and we ask whether the next transition puts both populations above, or alternatively, below, the Allee threshold. A similar study was conducted in a deterministic setting (Johnson and Hastings, 2018). That study laid the

foundations for an eventual treatment in a stochastic setting. Hence, in our work, we adopt the definition of ecological resilience formulated by Holling (Holling, 1973) as well as the framework proposed by Johnson and Hastings, but we also account for stochasticity in the system.

The literature on single, isolated tipping points is vast. However, studies of cascades of tipping points are less common. We begin with the background needed to formulate a stochastic, individual-based model that accounts for strong Allee effects. Our model follows a Markovian birth-death process, inspired by the theory of chemical reaction networks. We find that this representation naturally lends itself to a treatment with Markov chains and first-passage times. Then, we employ dimensionality reduction techniques and novel approximations to propose a reduced model that we study in detail.

### 2.3. Model Description

Much of the work done on modeling deterministic systems with one population that manifest Allee effects are based on either empirical observations or phenomenology. The crux of these models dates back to 1954 (Odum and Allee, 1954), where the observed per-capita growth rate was fit with a suitable function. The general form of such a deterministic model in continuous time is the following ordinary differential equation (ODE):

$$\frac{d\rho(t)}{dt} = \rho f(\rho), \tag{2.1}$$

where $\rho(t)$ denotes the average population density at time $t$, and $f(\rho)$ is a function specifying the form of the per-capita population growth rate at density $\rho$. There have been many functional forms proposed for $f(\rho)$ in the literature. A review of various specifications used in models can be found (Boukal and Berec, 2002).

In particular, a simple and important model was proposed early in the twentieth century (Volterra, 1938), where $f(\rho)$ is a quadratic polynomial function of $\rho$. The underlying assumptions of the model are as follows. Given a constant sex ratio, the number of meetings between males and females is proportional to $\rho^2$. The ratio of births to meetings can be affected by the population density and is hence assumed to be linearly decreasing in $\rho$. Also, the mortality rate of

individuals in the population is assumed to be proportional to $\rho$. Hence, the Volterra model takes the following form:

$$\frac{d\rho(t)}{dt} = -a_1\rho + (a_2 - a_3\rho)\rho^2 = -a_1\rho + a_2\rho^2 - a_3\rho^3, \tag{2.2}$$

where $a_1, a_2, a_3 > 0$. If we define the two real-valued roots,

$$k_1 = \frac{1}{2a_3}\left[a_2 - \sqrt{a_2^2 - 4a_1a_3}\right], \tag{2.3a}$$

$$k_2 = \frac{1}{2a_3}\left[a_2 + \sqrt{a_2^2 - 4a_1a_3}\right], \tag{2.3b}$$

with $a_2^2 > 4a_1a_3$, then the model is often shown in the following form (Courchamp et al., 1999):

$$\frac{d\rho(t)}{dt} = a_1\rho\left(1 - \frac{\rho}{k_2}\right)\left(\frac{\rho}{k_1} - 1\right), \tag{2.4}$$

resembling the logistic model with the addition of a new unstable steady state, $\rho = k_1$.

For the strong Allee effect, the Volterra model has three steady states: two stable states at $\rho = 0$ and $\rho = k_2$ and an unstable state at $\rho = k_1$. If the initial population size exceeds $k_1$, the population grows over time and converges to the stable steady state $\rho = k_2$, the carrying capacity of the system. If the initial population size is less than $k_1$, the population decays over time to the stable steady state $\rho = 0$ and goes extinct.

In order to investigate the effects of internal fluctuations or demographic stochasticity in a two-population system with both weak and strong Allee effects, we consider the temporal evolution of the system as specified by a Markovian birth-death process. Demographic stochasticity is included both in the dynamics of the locations and in the dispersal parameter. We account for the individual reaction kinetics explicitly, in a mechanistic manner, without relying on phenomenological considerations. Here, we follow the approach of Méndez and colleagues (Méndez et al., 2019) by casting the system as a chemical reaction network that results in an individual-based model (IBM). The minimal IBM that displays both the weak and strong Allee effect and also accounts for dispersal can be described as follows. It consists of two birth processes (linear and binary birth), a ternary

competition process, a linear death process, and an exchange process. We provide our reaction scheme below.

(2.5a) $$X_1 \xrightarrow{\mu_1} (1+b)X_1$$

(2.5b) $$2X_1 \xrightarrow{\lambda_1} (2+a)X_1$$

(2.5c) $$X_1 \xrightarrow{\gamma_1} \emptyset$$

(2.5d) $$3X_1 \xrightarrow{\tau_1} (3-c)X_1$$

(2.5e) $$X_1 \xrightarrow{d} X_2$$

(2.5f) $$X_2 \xrightarrow{\mu_2} (1+b)X_2$$

(2.5g) $$2X_2 \xrightarrow{\lambda_2} (2+a)X_2$$

(2.5h) $$X_2 \xrightarrow{\gamma_2} \emptyset$$

(2.5i) $$3X_2 \xrightarrow{\tau_2} (3-c)X_2$$

(2.5j) $$X_2 \xrightarrow{d} X_1$$

The first reaction is a linear birth process, which occurs at a constant rate $\mu_1$, and describes the baseline reproductive success of the first population in the absence of cooperative effects. It accounts for the fact that the typical individual produces $b$ offspring that reach reproductive age. The second reaction is a binary process that occurs at a constant rate $\lambda_1$. It describes cooperative interactions, such as breeding, anti-predator behavior, or foraging, that result in producing $a$ additional offspring which reach reproductive age. The third reaction is a linear death process, occurring at constant rate $\gamma_1$, which accounts for mortality due to natural causes. The fourth reaction is a ternary competition process, accounting for the results of overcrowding and resource depletion, where $c$ individuals die at rate $\tau_1$. Note that $1, 2$, and $3$ are the only meaningful values for $c$. The next reaction is an exchange process of symmetric dispersal between the two populations. This occurs at a constant rate of $d$. The last five reactions in the scheme describe the dynamics of the second population, respectively.

The reaction scheme (2.5) defines a Markovian process, and the temporal evolution of $P(n_1, n_2, t)$, the probability of having $n_i$ individuals from the $i^{th}$ population at time $t$ for $i = 1, 2$, is described by the following master equation, also known as the forward Kolmogorov equation (Gardiner, 2004):

$$\frac{dP(\boldsymbol{n}, t)}{dt} = \sum_{\boldsymbol{r}} [W(\boldsymbol{n} - \boldsymbol{r}, \boldsymbol{r}) P(\boldsymbol{n} - \boldsymbol{r}, t) - W(\boldsymbol{n}, \boldsymbol{r}) P(\boldsymbol{n}, t)], \tag{2.6}$$

where $P(\boldsymbol{n} < \boldsymbol{0}, t) = P(n_1 < 0, n_2 < 0, t) = 0$. Here $W(\boldsymbol{n}, \boldsymbol{r})$ denotes the set of transition rates between the states with $\boldsymbol{n}$ and $\boldsymbol{n} + \boldsymbol{r}$ individuals, where

$$\begin{aligned} \boldsymbol{r} &= \{\boldsymbol{r_1}, \boldsymbol{r_2}, \ldots, \boldsymbol{r_{10}}\} \\ &= \{(b, 0), (a, 0), (-1, 0), (-c, 0), (-1, 0), (0, b), (0, a), (0, -1), (0, -c), (0, -1)\} \end{aligned}$$

is the vector of transition increments corresponding to the system given by (2.5). The transition rates corresponding to each reaction, $W(\boldsymbol{n}, \boldsymbol{r})$, are obtained from the reaction kinetics (Gardiner (2004); Van Kampen (1992)):

$$W(\boldsymbol{n}, \boldsymbol{r_1}) = \mu_1 n_1, \tag{2.7a}$$

$$W(\boldsymbol{n}, \boldsymbol{r_2}) = \frac{\lambda_1}{2} n_1 (n_1 - 1), \tag{2.7b}$$

$$W(\boldsymbol{n}, \boldsymbol{r_3}) = \gamma_1 n_1, \tag{2.7c}$$

$$W(\boldsymbol{n}, \boldsymbol{r_4}) = \frac{\tau_1}{6} n_1 (n_1 - 1)(n_1 - 2), \tag{2.7d}$$

$$W(\boldsymbol{n}, \boldsymbol{r_5}) = d n_2, \tag{2.7e}$$

$$W(\boldsymbol{n}, \boldsymbol{r_6}) = \mu_2 n_2, \tag{2.7f}$$

$$W(\boldsymbol{n}, \boldsymbol{r_7}) = \frac{\lambda_2}{2} n_2 (n_2 - 1), \tag{2.7g}$$

$$W(\boldsymbol{n}, \boldsymbol{r_8}) = \gamma_2 n_2, \tag{2.7h}$$

$$W(\boldsymbol{n}, \boldsymbol{r_9}) = \frac{\tau_2}{6} n_2 (n_2 - 1)(n_2 - 2), \tag{2.7i}$$

$$W(\boldsymbol{n}, \boldsymbol{r_{10}}) = d n_1 \tag{2.7j}$$

Deterministic ODEs for the average population sizes can be obtained from Eq. (2.6). Multiplying Eq. (2.6) by $n_1 n_2$, using transition rates (2.7), and summing over all values of $n_1$ and $n_2$, we find

$$\frac{d\rho_1}{dt} = (b\mu_1 - \gamma_1 - d)\rho_1 + \frac{a\lambda_1}{2}\rho_1^2 - \frac{c\tau_1}{6}\rho_1^3 + d\rho_2, \tag{2.8a}$$

$$\frac{d\rho_2}{dt} = (b\mu_2 - \gamma_2 - d)\rho_2 + \frac{a\lambda_2}{2}\rho_2^2 - \frac{c\tau_2}{6}\rho_2^3 + d\rho_1 \tag{2.8b}$$

where $\rho_i = \langle n_i \rangle$ is the mean number of individuals in population $i$ for $i = 1, 2$. We note that this pair of deterministic equations holds strictly when the demographic fluctuations vanish. This occurs in the macroscopic limit as the population size and spatial extent of each population increase to infinity such that their ratio, the population density, stays constant or approaches a finite limit.

For the sake of simplicity, in what follows, we focus on the simplest version of this IBM. Namely, we treat the Markovian process as a single-step process with $a = b = c = 1$. The set of reactions (2.5) then becomes

$$X_1 \xrightarrow{\mu_1} 2X_1 \tag{2.9a}$$

$$2X_1 \xrightarrow{\lambda_1} 3X_1 \tag{2.9b}$$

$$X_1 \xrightarrow{\gamma_1} \emptyset \tag{2.9c}$$

$$3X_1 \xrightarrow{\tau_1} 2X_1 \tag{2.9d}$$

$$X_1 \xrightarrow{d} X_2 \tag{2.9e}$$

$$X_2 \xrightarrow{\mu_2} 2X_2 \tag{2.9f}$$

$$2X_2 \xrightarrow{\lambda_2} 3X_2 \tag{2.9g}$$

$$X_2 \xrightarrow{\gamma_2} \emptyset \tag{2.9h}$$

$$3X_2 \xrightarrow{\tau_2} 2X_2 \tag{2.9i}$$

$$X_2 \xrightarrow{d} X_1 \tag{2.9j}$$

The mean-field rate equations corresponding to (2.9) are

$$\frac{d\rho_1}{dt} = (\mu_1 - \gamma_1 - d)\rho_1 + \frac{\lambda_1}{2}\rho_1^2 - \frac{\tau_1}{6}\rho_1^3 + d\rho_2, \tag{2.10a}$$

$$\frac{d\rho_2}{dt} = (\mu_2 - \gamma_2 - d)\rho_2 + \frac{\lambda_2}{2}\rho_2^2 - \frac{\tau_2}{6}\rho_2^3 + d\rho_1 \tag{2.10b}$$

For this set of reactions, the master equation can be explicitly obtained as

$$\begin{aligned}\frac{dP(n_1,n_2,t)}{dt} &= (n_1-1)\left[\frac{\lambda_1}{2}(n_1-2)+\mu_1\right]P(n_1-1,n_2,t)\\ &+ (n_1+1)\left[\frac{\tau_1}{6}n_1(n_1-1)+\gamma_1+d\right]P(n_1+1,n_2,t)\\ &+ (n_2-1)\left[\frac{\lambda_2}{2}(n_2-2)+\mu_2\right]P(n_1,n_2-1,t)\\ &+ (n_2+1)\left[\frac{\tau_2}{6}n_2(n_2-1)+\gamma_2+d\right]P(n_1,n_2+1,t)\\ &- n_1\left[\frac{\lambda_1}{2}(n_1-1)+\mu_1+\frac{\tau_1}{6}(n_1-1)(n_1-2)+\gamma_1+d\right]P(n_1,n_2,t)\\ &- n_2\left[\frac{\lambda_2}{2}(n_2-1)+\mu_2+\frac{\tau_2}{6}(n_2-1)(n_2-2)+\gamma_2+d\right]P(n_1,n_2,t)\end{aligned} \tag{2.11}$$

We note that the master equation (2.11) includes only single-step processes where the transitions take place between the states $\boldsymbol{n}$ and $\boldsymbol{n}\pm(1,0)$ or $\boldsymbol{n}$ and $\boldsymbol{n}\pm(0,1)$. Next, we can define dimensionless quantities in terms of the reaction rates as follows:

$$N_i = \frac{3\lambda_i}{2\tau_i}, \tag{2.12a}$$

$$\delta_i^2 = 1 + \frac{8\tau_i(\mu_i - \gamma_i - d)}{3\lambda_i^2}, \tag{2.12b}$$

$$R_0^{(i)} = \frac{\mu_i}{\gamma_i + d} \tag{2.12c}$$

Note that $N_i$ defines the scale of the typical size of population $i$ prior to extinction. The identities (2.12) establish a relation between the microscopic $(\lambda_i, \mu_i, \gamma_i, \tau_i)$ and macroscopic $(N_i, \delta_i, R_0^{(i)})$ parameters, which are obtainable through field observations.

Observe that the individual-based model displays the strong Allee effect, if $\mu_i < \gamma_i + d$, or $R_0^{(i)} < 1$. Furthermore, for $R_0^{(i)} < 1$ we have $\delta_i < 1$. For the strong Allee effect, we must also demand that $\delta_i > 0$.

As mentioned in the Introduction, our starting point for the model used in this work is the deterministic skeleton for the non-dimensionalized model described by Johnson and Hastings, reproduced here for convenience.

$$\dot{X}_1 = X_1(\beta_1 - (X_1 - 1)^2) + D(X_2 - X_1), \tag{2.13a}$$

$$\dot{X}_2 = X_2(\beta_2 - (X_2 - 1)^2) + D(X_1 - X_2) \tag{2.13b}$$

In the model above, the parameter $\beta_i$ represents a measure for the quality of the environment by the population denoted by $X_i$. The parameter $D$ denotes passive diffusion in the system and is an indicator of network connectivity. See the work by Johnson and Hastings for a detailed exposition of the model.

In order to make our subsequent analyses feasible, we aim to reduce the dimensionality of the parameter space for our stochastic model. So, for the sake of illustration, we treat the stochastic rate parameters in (2.9) as identical for both populations. This assumption appears to be reasonable in many cases, because of the presence of dispersal between populations in close proximity. Moreover, this assumption is consistent with the model parameterization in the work by Johnson and Hastings.

Thus, our matching scheme can be written as follows:

$$\mu_1 := \beta_1, \tag{2.14a}$$

$$\mu_2 := \beta_2, \tag{2.14b}$$

$$\lambda := \lambda_1 = \lambda_2 \equiv 4, \tag{2.14c}$$

$$\gamma := \gamma_1 = \gamma_2 \equiv 1, \tag{2.14d}$$

$$\tau := \tau_1 = \tau_2 \equiv 6, \tag{2.14e}$$

$$d := D, \tag{2.14f}$$

$$\widetilde{N} := \widetilde{N}_1 = \widetilde{N}_2 \tag{2.14g}$$

So for $i = 1$ and 2,

$$\widetilde{N} = 1, \quad \delta_i^2 = \beta_i - D, \quad R_0^{(i)} = \frac{\beta_i}{D+1}. \tag{2.15}$$

In what follows, we are interested in the case of bistability, which is manifest in the case of the strong Allee effect. Because the regime of the strong Allee effect requires $0 < \delta_i < 1$ and $R_0^{(i)} < 1$, we have that $\beta_i > D$ and $\beta_i < D + 1$. Thus, the following condition is obtained:

$$D < \beta_i < D + 1 \tag{2.16}$$

## 2.4. Methods

We note that our stochastic model operates over a two-dimensional state space. We argue that the dimension of the state space is as low as possible but nevertheless captures the desired phenomenology. Due to the presence of Allee effects, the deterministic skeleton of our model has cubic nonlinearities. In order to tackle this complexity, Johnson and Hastings conducted numerical simulations to understand how the transition rate $D$ between the two patches determines the bifurcation structure for this system (Johnson and Hastings, 2018). In this study, however, we restrict our attention to the case of bistability, which is properly addressed with a stochastic model.

As discussed in the previous section, we adopted a master equation approach for our model (Méndez et al., 2019). Instead of specifying a model with carrying capacities, we used an individual-based modeling approach using a chemical reaction network. This allows for a fine-grained representation of the underlying discrete, stochastic process. Using this approach, we then wrote down the two-dimensional chemical master equation for the process. Given that this stochastic process is a continuous-time Markov chain (CTMC), it can be explicitly described by a generator $\mathcal{Q}$-matrix with a countable state space. A nice feature of most ecological models is that they are built around processes that will approach a compact region exponentially quickly. Any reasonable ecological model should not have unbounded population growth. Density dependence in ecology models typically ensures this. Thus, our model effectively operates over a finite state space as the probability of arbitrarily large populations is negligibly small. Using this insight, we were able to obtain a finite-state CTMC in two dimensions.

Since the multi-dimensional master equation was relatively unwieldy to work with, we reduced the two-dimensional state space to one dimension (Allen, 2010; Allen and Allen, 2003). Denoting $N := N_1 = N_2$ as the maximum number of individuals in either population, the specific mapping function used was $f(x, y) = (N + 1)x + y + 1$, for $x, y \in [0, N]$. We could also exploit the sparsity

of the banded $\mathcal{Q}$-matrix to reduce computational cost (van Doorn and Pollett, 2013). Specifically, the $\mathcal{Q}$-matrix has size $(N+1)^2 \times (N+1)^2$ with $7N^2 + 4N - 2$ nonzero entries, yielding a matrix density of $\mathcal{O}(N^{-2})$. Thus, the sparsity of the matrix increases quadratically in $N$.

For the ensuing analyses, we specified population thresholds by treating them as identical across patches. Denoting $L := L_1 = L_2$ and $H := H_1 = H_2$ as the low and high thresholds, we defined $A := A_1 = A_2$ as the Allee threshold, noting that $0 < L < A < H \leq N$. Here $N$ is defined as previously and can be understood as a system size parameter. The linear ordering of the thresholds guarantees that $L$ is always less than $H$. Note that the smallest $L$ threshold, $L = 1$, behaves as a state corresponding to quasi-extinction. Moreover, with $2 \leq A \leq N - 1$, we have $A + 1 \leq H \leq N$ and $1 \leq L \leq A - 1$. It can be shown that this results in $\binom{N}{3}$ combinations of the thresholds.

In order to probe the system under consideration, we numerically computed the mean first-passage times (MFPTs) for model (2.9) with the state-space parameterized by $N$ for all combinations of the parameters $\beta_i, D, L$, and $H$ (Chou and D'Orsogna, 2014; Polizzi et al., 2016). The procedure can be described as follows. First, we formed the $\mathcal{Q}$-matrix for each point in parameter space. We also formed a vector of initial state probabilities $p_0$ governing the subsequent evolution of the CTMC. Then, the rows and columns of $\mathcal{Q}$ corresponding to the trap states (e.g., extinction) were removed. Similarly, the corresponding entry in $p_0$ was removed. Next, using the truncated $\mathcal{Q}$-matrix, $\widetilde{\mathcal{Q}}$, we computed the matrix of mean residence times, or $-\widetilde{\mathcal{Q}}^{-1}$. Finally, we computed the sum of the entries in $-\widetilde{\mathcal{Q}}^{-1}p_0$ to yield the MFPT from the initial state to the desired end state.

We could then construct a compartmental system with a reduced state space consisting of just four states: $HH$, $HL$, $LL$, and $LH$. Each of these states corresponds to a combination of population thresholds. For instance, $HL$ means that the first population is at a high abundance and the second population is at a low level. The MFPTs from the original model were used as input rates for the transition rate matrix of the reduced model. Thus we used an emulator, or meta-model, as a proxy to analyze the original system.

Throughout this work, we analyze a simple system that exhibits noise-induced tipping point cascades in the vicinity of saddle-node bifurcations. We can use the emulator described previously to construct the schematic diagram in Fig. 2.1.

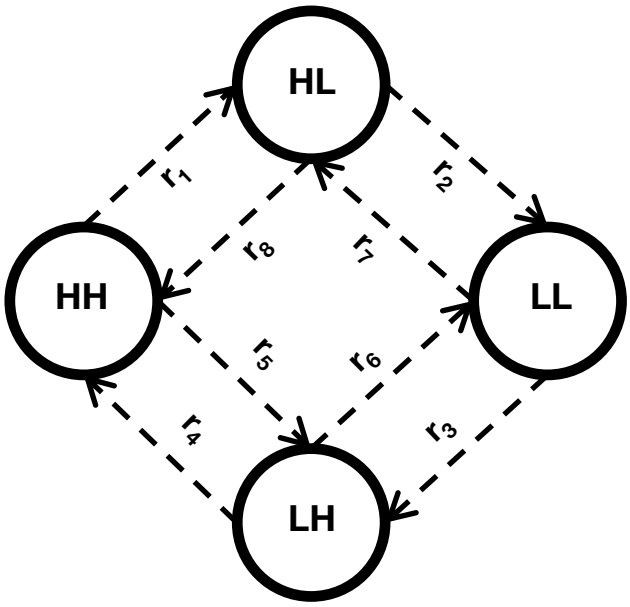


FIGURE 2.1. **Schematic diagram of the complete emulator.** Each state in the compartmental system is indicated as a circle and denoted by capital letters. The letter $H$ corresponds to the high threshold and the letter $L$ corresponds to the low threshold. The first (second) letter refers to the first (second) population. Each $r_i$ for $i = 1, \ldots, 8$ describes the transition rate, or inverse of the corresponding mean first-passage time, between appropriate states.

In the diagram, each $r_i$ for $i = 1, \ldots, 8$ represents the rate of the transition between the relevant compartments. Each rate can be obtained as the inverse of the corresponding mean first-passage time. Given that the process is represented as a CTMC, we can write down the transition rate matrix $\mathcal{S}$ for the emulator. The transition probability matrix of the embedded discrete-time Markov chain gives the one-step transition probabilities of the system.

The $\mathcal{S}$-matrix is given as:

$$\mathcal{S} = \begin{pmatrix} -r_1 - r_5 & r_1 & r_5 & 0 \\ r_8 & -r_2 - r_8 & 0 & r_2 \\ r_4 & 0 & -r_4 - r_6 & r_6 \\ 0 & r_7 & r_3 & -r_3 - r_7 \end{pmatrix}$$

where the ordering of the states is $(HH, HL, LH, LL)$. Note that $\mathcal{S}$ satisfies the properties of a generator matrix, namely:

- All off-diagonal elements are non-negative.
- All diagonal elements are negative.
- Each row sums to zero.

Now, we obtain the transition probability matrix $\mathcal{T}$ corresponding to the system:

$$\mathcal{T} = \begin{pmatrix} 0 & \frac{r_1}{r_1+r_5} & \frac{r_5}{r_1+r_5} & 0 \\ \frac{r_8}{r_2+r_8} & 0 & 0 & \frac{r_2}{r_2+r_8} \\ \frac{r_4}{r_4+r_6} & 0 & 0 & \frac{r_6}{r_4+r_6} \\ 0 & \frac{r_7}{r_3+r_7} & \frac{r_3}{r_3+r_7} & 0 \end{pmatrix}$$

Note that $\mathcal{T}$ is a row-stochastic matrix. The probability of a system collapse differs from the likelihood of system resiliency in a manner that is quantified by the following rates:

$$r_2 = \frac{1}{\text{MFPT}(HL \to LL)} \tag{2.17a}$$

$$r_4 = \frac{1}{\text{MFPT}(LH \to HH)} \tag{2.17b}$$

$$r_6 = \frac{1}{\text{MFPT}(LH \to LL)} \tag{2.17c}$$

$$r_8 = \frac{1}{\text{MFPT}(HL \to HH)} \tag{2.17d}$$

From (2.17),

$$p_1 := \Pr(HL \to HH) = \frac{r_8}{r_2 + r_8}$$

and

$$p_2 := \Pr(LH \to HH) = \frac{r_4}{r_4 + r_6}$$

. Using the inclusion-exclusion principle for probabilities, we obtain the probability $p$ of the system recovering to high population abundances (i.e., when the terminal state is $HH$) as

$$p = p_1 + p_2 - p_1 p_2.$$

Our aim henceforth is to explore the multi-dimensional region of parameter space that corresponds to the desired probability of system resiliency. In symbols, for a fixed $N$, we want to

identify all combinations $(D, \beta_1, \beta_2, A, H, L)$ where $D > 0,\ \beta_1 \in (D, D+1),\ \beta_2 \in (D, D+1)$, $A \in [2, N-1]$, $H \in [A+1, N]$, and $L \in [1, A-1]$, such that the system recovers to a high-high state. In order to explore the parameter space numerically, we began by specifying an upper bound of 1 for the dispersal parameter $D$. This value for $D$ could be considered as large, because $D$ should be commensurate with the per-capita rate of the system, which was chosen as $r = 1$ in the non-dimensionalization of the model (2.13) (Johnson and Hastings, 2018). This implies that $D \in (0, 1)$. Then, we chose $N = 9$. This was the largest $N$ such that the largest 1-norm condition number among the space of all matrices $\widetilde{\mathcal{Q}}$ taken over the subset of parameter space considered, was less than $10^7$. For our chosen value of $N$, we found this condition number to be approximately $5.92 \times 10^6$. We note that numerical linear algebra was used here instead of Monte-Carlo methods, including the Doob-Gillespie algorithm (Gillespie, 1976, 1977)). The primary justification for this choice of method was that some of the simulated mean first-passage times were large, causing long runtimes with Monte-Carlo simulations. All computations were performed in MATLAB (MATLAB, 2021).

### 2.5. Results

By defining $p$ as the probability of transitioning from the $LH$ state to the $HH$ state, we can explore how the behavior of the system depends on the parameters. For purposes of display, we chose three values for the parameters governing patch quality, for each value of $D$ (i.e., $\beta_i = D + 0.01, D + 0.5, D + 0.99$). By analyzing simulation output, we found that the minimum value of $p$ over the parameter space was approximately 0.73, and the maximum value was 0.81. This indicates the probability of the system transitioning from the $LH$ to the $LL$ state, and collapsing, is never more than 0.27. We also varied a threshold $\eta$, such that $p > \eta$, with values of $\eta = 0.75, 0.76$, and 0.77 (Fig. 2.2). We can expect that the fraction of parameter space $\nu$ for which the system recovers will decrease monotonically with the threshold $\eta$. If the goal is population persistence, we would like to find a region of parameter space that yields relatively large values for both $\nu$ and $\eta$.

Referring to Fig. 2.2, several observations can be made. For instance, low dispersal ($D = 0.01$) guarantees that the desired probability of system resiliency is never 76% or higher (i.e., $\nu = 0$). This makes sense because rescue effects, by which the stronger patch "rescues" the weaker patch, are reduced at low dispersal rates. Also, $\nu$ decreases as $\eta$ is increased. This is plausible since $\eta$ acts

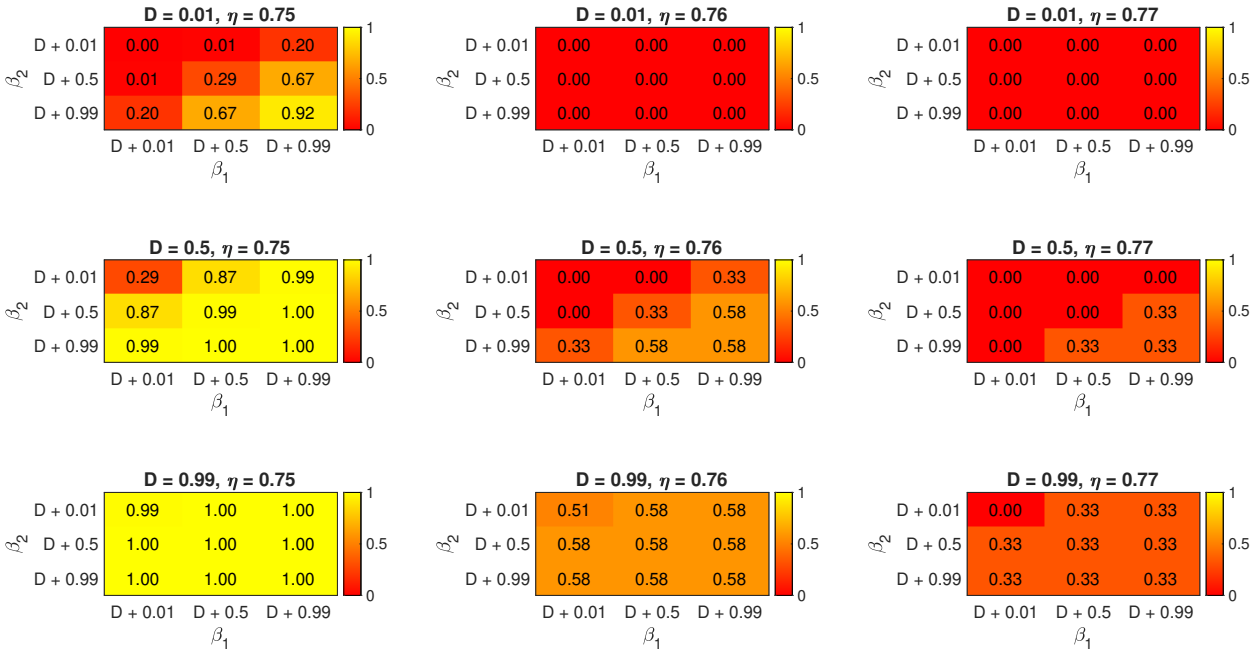


FIGURE 2.2. **System resilience as a function of model parameters.** A matrix of heatmaps summarizing the simulation study. Each heatmap indicates the value of $\nu$, the fraction of parameter space for which the system recovers to high abundances, corresponding to a parameter combination $(\beta_1, \beta_2, D, \eta)$. The range of $\beta_1$ values are on the x-axis and the range of values for $\beta_2$ are on the y-axis of each heatmap. In the $3 \times 3$ matrix comprising the entire figure, $D$ increases by row and $\eta$ increases by column.

as a constraint on the parameter space and increasing $\eta$ implies greater specificity. In all cases, if both Allee effects are weakly strong (i.e., $(\beta_1, \beta_2) = (D+0.99, D+0.99)$), then $\nu$ is maximized for a given combination of $D$ and $\eta$. This is especially noticeable when $D = 0.99$, regardless of the value of the threshold parameter $\eta$ (i.e., see the third row of Fig. 2.2). Lastly, if each heatmap is treated as a matrix, we see that the column (row) of a given matrix is increasing in $\nu$, as the corresponding column (row) index is increased. This observation is also reflected within the coloring scheme of each matrix. As expected, $\nu$ is maximal with a value of 1.00, for $D = 0.99, \eta = 0.75, \beta_1 > D + 0.01$, and $\beta_2 > D + 0.01$.

We made explicit the correspondence between various combinations of the high threshold and Allee threshold, with $L$ fixed at a value of 1 (Fig. 2.3). We focused here on the case of low dispersal (i.e., $D = 0.01$). We see that the combination $(A, H) = (2, 3)$ is undesirable for the

system, as it always results in the lowest value of $p = 0.726$ for a given pair $(\beta_1, \beta_2)$. However, as the high threshold is increased while the Allee threshold is held constant, we see that $p$ increases monotonically. This is true for any value of the Allee threshold (i.e., with only $H$ increased). Both of the Allee effects need to be very strong (i.e., $\beta_1 = \beta_2 = D + 0.01$) to see a marked increase in $p$. We also explored the case of moderate dispersal (Fig. 2.4), with $D = 0.5$. Here, we notice that the lowest value for $p$ is 0.738, which is attained for $(A, H) = (2, 3)$, as in Fig. 2.3. The key difference between Figs. 2.3 and 2.4 is that $p$ now has a moderate dependence on $H$ for any fixed combination $(\beta_1, \beta_2, D, L)$. At most one of the Allee effects can be very strong (i.e., either $\beta_1 = D + 0.01$ or $\beta_2 = D + 0.01$) in order for a clear improvement in system resilience, or an increase in $p$, to be visible. Finally, in Fig. 2.5, we address the scenario of high dispersal ($D = 0.99$.) It is clear that $(A, H) = (2, 3)$ is a consistent minimizer across all levels of dispersal covered thus far, as the lowest value for $p$ is achieved here with a value of 0.750 (in Fig. 2.5). Also, a vast majority of scenarios in the presence of high dispersal ($D = 0.99$) yield better outcomes for the system, compared with the case of low dispersal ($D = 0.01$). In other words, $p$ is relatively high throughout the subcases shown in Fig. 2.5, compared with Fig. 2.3.

For the sake of completeness, we also explored the analogues of Figs. 2.3 to 2.5 by fixing $H = N$ and varying $L$. As shown in Fig. 2.6 corresponding to the case of low dispersal ($D = 0.01$), $L = 1$ is an undesirable value for the low threshold in the system, as it guarantees the lowest value of $p$ for a given combination $(\beta_1, \beta_2, A)$. Interestingly, the highest value of $p$ occurs for $(\beta_1, \beta_2, L) = (D + 0.99, D + 0.99, 5)$. In other words, $p$ is maximized in the interior of $A - L$ space, for any given combination of $\beta_1$ and $\beta_2$. Similarly, in Fig. 2.7 with moderate dispersal ($D = 0.5$), the low threshold $L = 1$ yields the smallest value for $p$. On the other hand, $p$ is now maximized for $(\beta_1, \beta_2) = (D + 0.99, D + 0.99)$, when $L \leq 5$. Finally, in Fig. 2.8, we analyze the case of high dispersal. All scenarios favor system recovery more strongly than in the cases of low or moderate dispersal, with weaker Allee effects being more favorable for the system. For instance, $(\beta_1, \beta_2) = (D + 0.99, D + 0.99)$ results in $p > 0.806$ for all values of $A$ and $L$, but $(\beta_1, \beta_2) = (D + 0.01, D + 0.01)$ yields $p < 0.77$ across the $A - L$ space.

In general, a high degree of dispersal between both patches is needed to yield a desirable outcome for the system. In other words, in order to tip positive change with confidence, $D$ should

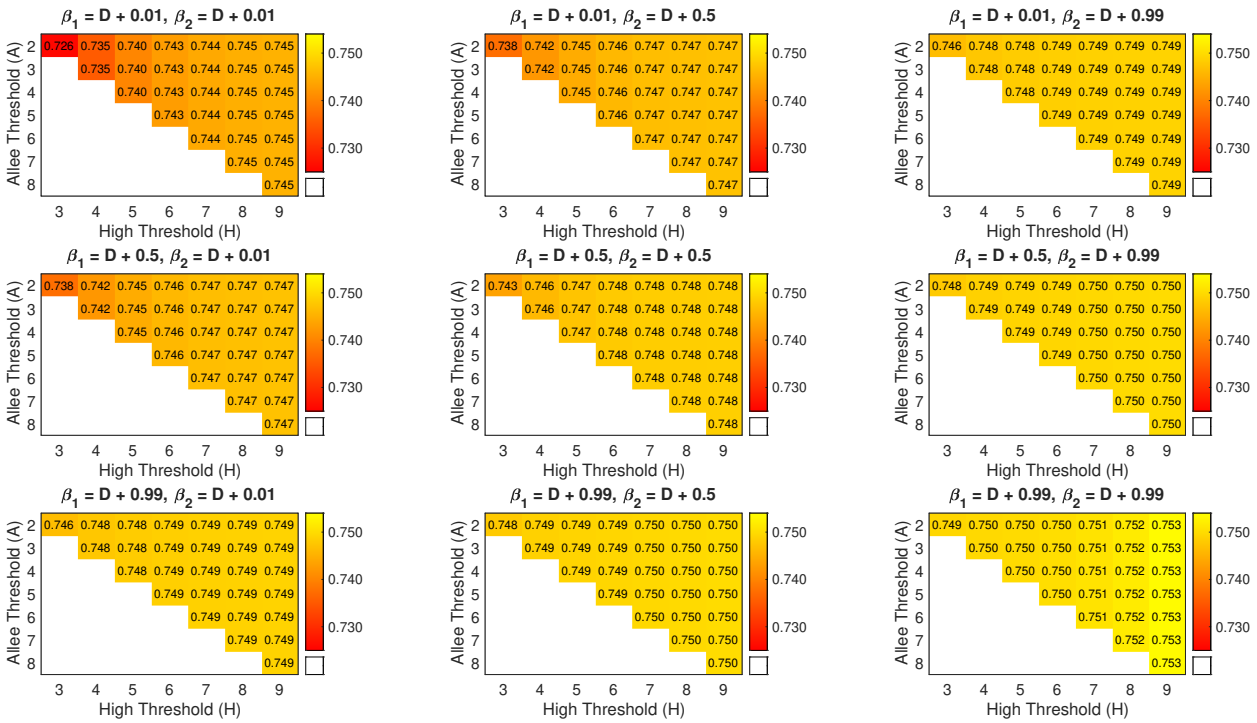


FIGURE 2.3. **Likelihood of positive tipping in the presence of low dispersal ($D = 0.01$), with $L = 1$.** A visualization of the case of low dispersal with a low threshold ($L$) corresponding to quasi-extinction. The combinations of $A$ and $H$ are shown explicitly. Each heatmap shows the value of $p$, the probability of system recovery, corresponding to a combination $(\beta_1, \beta_2, A, H)$ for $D = 0.01$ and $L = 1$.

be sufficiently large. A key issue which relates to the idea of a rescue effect is the relative likelihood of the transition from $HH$ to $LH$ (or $HL$), as compared with the transitions $LH$ (or $HL$) to $LL$ and $LH$ (or $HL$) to $HH$. The likelihood of system resiliency in the form of a rescue effect is given by $p$, whereas the probability of a total failure or catastrophic collapse is given by $1 - p$. Note that this means a partial failure of the system is inevitable (i.e., with probability $1 = p + (1 - p)$). This result follows from the nature of the one-step transition probabilities in the emulator framework. Thus, we can reason that the odds of system recovery is equal to $\frac{p}{1-p}$.

Given this series of observations, there is an interesting and intuitive explanation that generalizes our setting. Noting that $0 \leq p \leq 1$ since $p$ is a probability, we have that

$$\frac{p}{1-p} = p + p^2 + p^3 + \dots$$

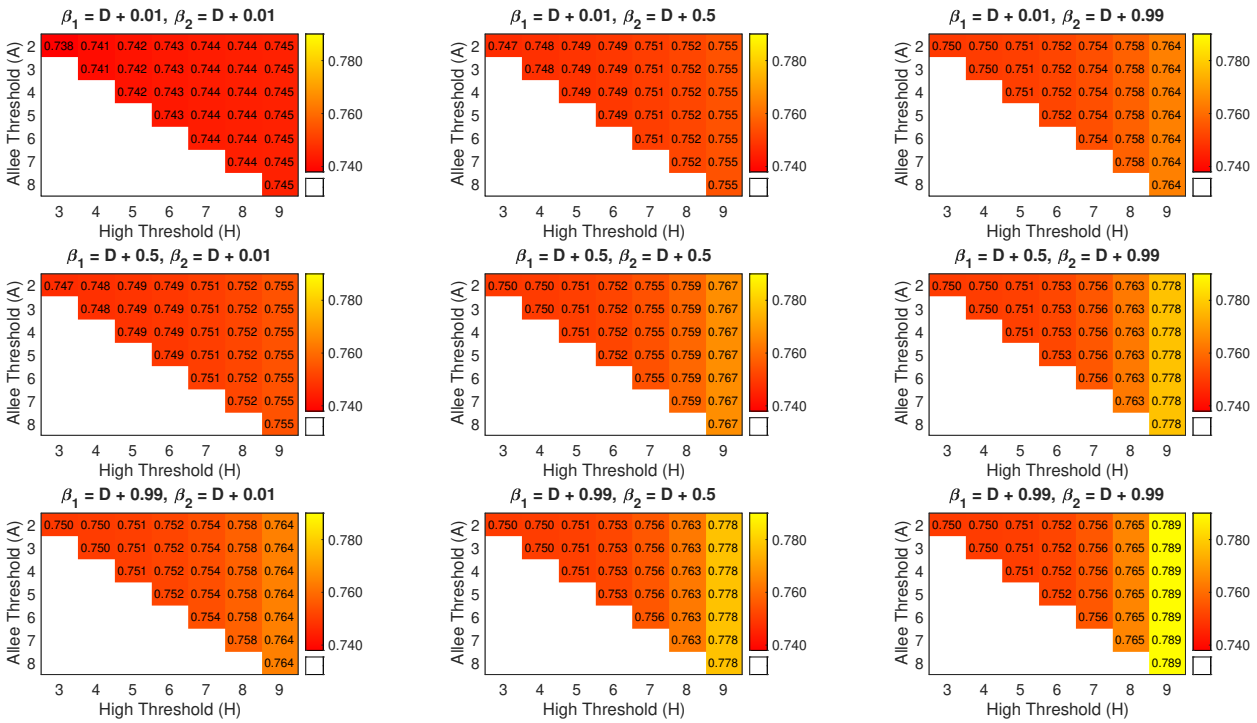


FIGURE 2.4. **Likelihood of positive tipping in the presence of moderate dispersal ($D = 0.5$), with $L = 1$.** A visualization of the case of moderate dispersal with a low threshold ($L$) corresponding to quasi-extinction. The combinations of $A$ and $H$ are shown explicitly. Each heatmap shows the value of $p$, the probability of system recovery, corresponding to a combination $(\beta_1, \beta_2, A, H)$ for $D = 0.5$ and $L = 1$.

is a convergent geometric series. Thus, we can write the left-hand side of the equation above as the odds of one network tipping favorably, where the network consists of a system with two patches. The right-hand side of the equation, however, can be interpreted as the cumulative probability of all such networks tipping favorably, i.e.,

$$\frac{p}{1-p} = \lim_{N\to\infty} \sum_{n=1}^{N} p^n,$$

where $n$ is the number of two-patch systems in a network. With this analysis, we thus see an instance of a tipping cascade of networks in the form of a domino effect. Note that the propagation of domino dynamics through a collection of networks requires strong connectivity, or high dispersal, in our model (Lenton, 2020).

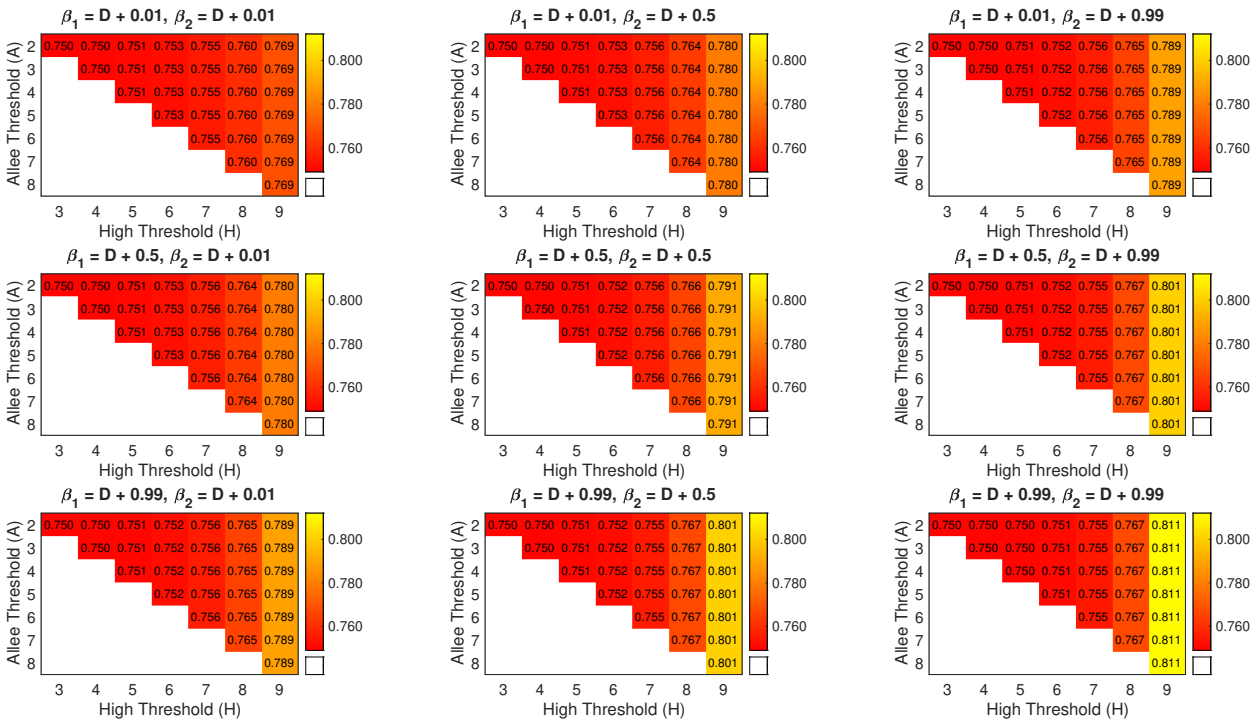


FIGURE 2.5. **Likelihood of positive tipping in the presence of high dispersal ($D = 0.99$), with $L = 1$.** A visualization of the case of high dispersal with a low threshold ($L$) corresponding to quasi-extinction. The combinations of $A$ and $H$ are shown explicitly. Each heatmap shows the value of $p$, the probability of system recovery, corresponding to a combination $(\beta_1, \beta_2, A, H)$ for $D = 0.99$ and $L = 1$.

## 2.6. Discussion

Our analysis of a minimal, stochastic system that could have cascading tipping points yields some interesting insights. A novel result of this work is that noise-induced tipping can distinguish a catastrophic collapse and a successful recovery from the brink of extinction. This idea is expressed succinctly as the distinction between the tipping of positive change and the failure to adequately address an impending critical transition (Lenton, 2020). In our two-population model, we showed that if the system is in the low/high state, a stochastic perturbation due to demographic noise results in either a collapse of both populations (low/low state) or a full recovery to the high/high stable state. This may be a key feature of spatially connected populations with strong Allee effects, and analyzing these dynamics should inform management strategies for similar ecological systems. We found that a population with higher resilience, in the form of a larger population abundance, has the capacity to save its counterpart through a rescue effect. In particular, this occurs due to

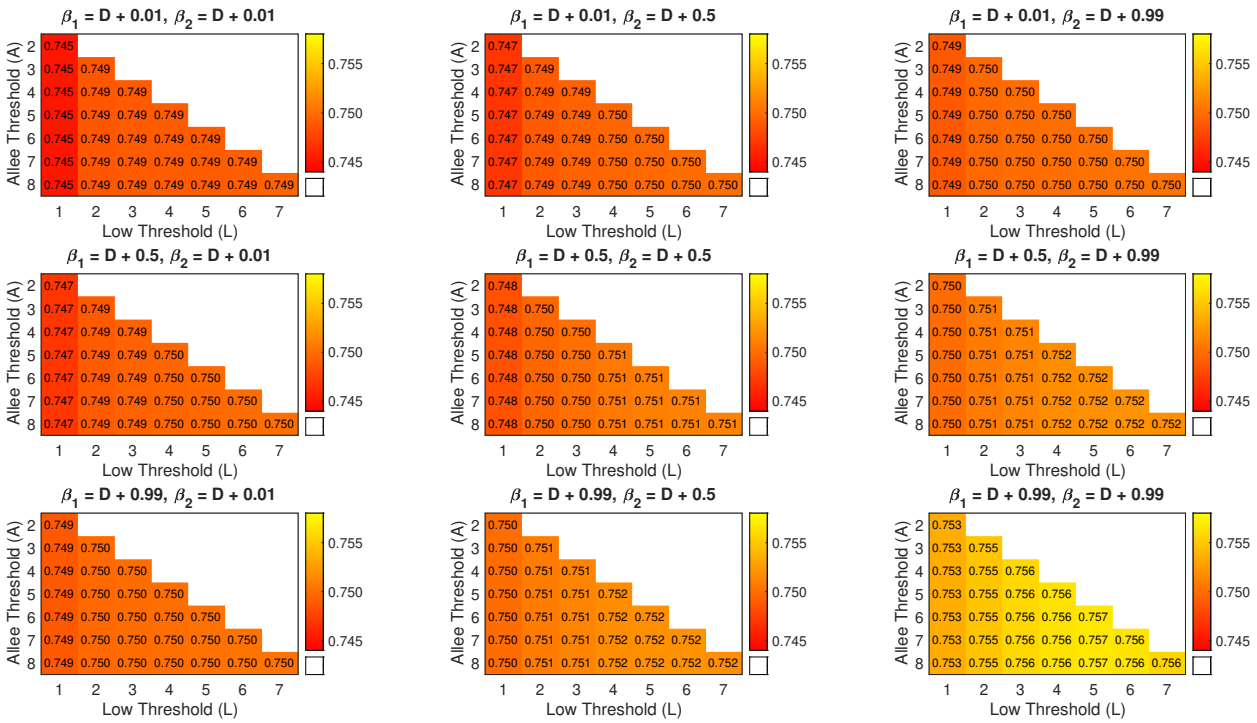


FIGURE 2.6. **Likelihood of positive tipping in the presence of low dispersal ($D = 0.01$), with $H = N$.** A visualization of the case of low dispersal with a high threshold ($H$) corresponding to the carrying capacity. The combinations of $A$ and $L$ are shown explicitly. Each heatmap shows the value of $p$, the probability of system recovery, corresponding to a combination $(\beta_1, \beta_2, A, L)$ for $D = 0.01$ and $H = N$.

the presence of dispersal between the populations. In the presence of noise, patch homogeneity, and strong network connectivity, the system is more likely to exhibit a tipping point cascade (Lenton, 2020).

Some discussion of systems with noise-induced tipping and their features is needed at this point. In situations where tipping one system increases the probability of another system tipping – for example, melting of the Greenland ice sheet increases the likelihood of failure of the Atlantic Meridional Overturning Circulation (AMOC) – the first system should act as a proxy for the entire network, in terms of a call to action. This is an important point, because by definition, our system can tip without warning, thus precluding detection through generic early-warning signals. However, we have been able to characterize the likelihood of its propensity to tip, either favorably or catastrophically (Lenton, 2020). The results from our analysis support the hypothesis that both stochastic dynamics might play a key role in regime shifts and their associated tipping (Rocha

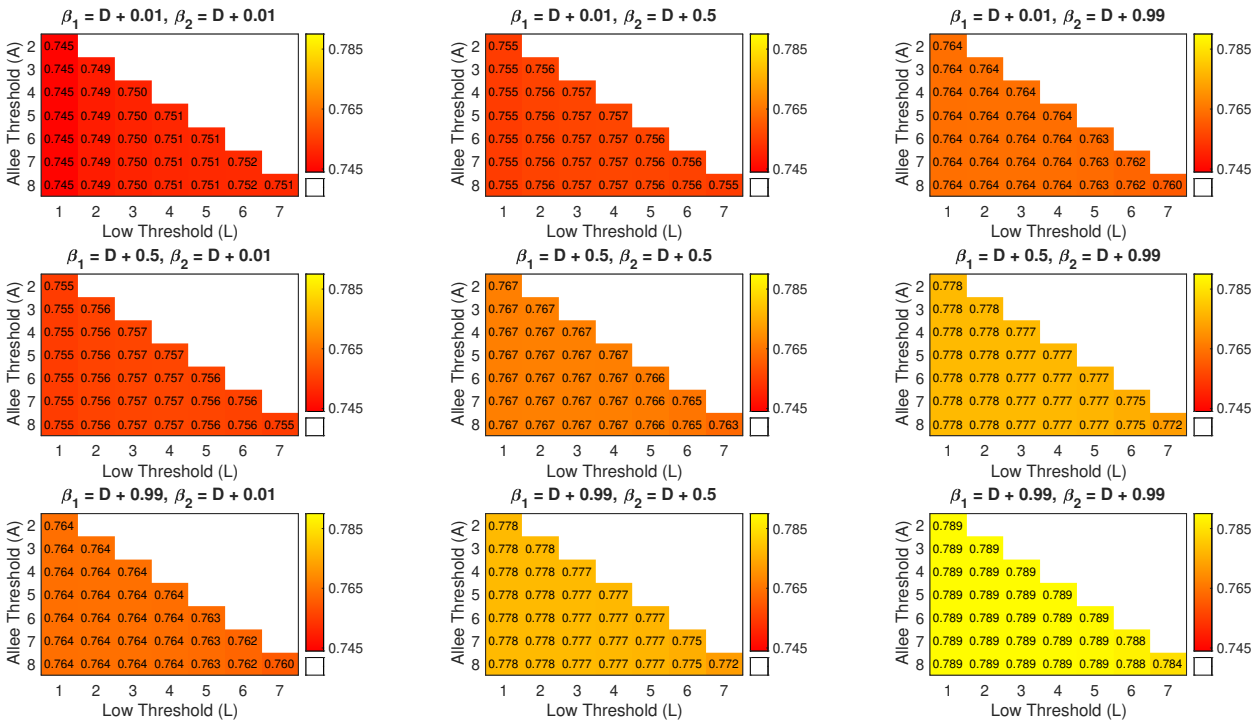


FIGURE 2.7. **Likelihood of positive tipping in the presence of moderate dispersal ($D = 0.5$), with $H = N$.** A visualization of the case of moderate dispersal with a high threshold ($H$) corresponding to the carrying capacity. The combinations of $A$ and $L$ are shown explicitly. Each heatmap shows the value of $p$, the probability of system recovery, corresponding to a combination $(\beta_1, \beta_2, A, L)$ for $D = 0.5$ and $H = N$.

et al., 2018). In particular, domino effects have relatively slow temporal dynamics and larger spatial scales; in our case, the spatial scale of the dispersal parameter dominates the time scale in magnitude. In addition, the one-step transition probabilities in our model support the notion that structural dependencies manifest as one-way interactions for the domino effect. This is a salient feature of regime shift couplings. In our system, we note that a partial collapse is inevitable. Most examples of regime shifts exhibiting domino effects concern the Earth system, including monsoon weakening and thermohaline circulation collapse, as well as nutrient transport mechanisms (Rocha et al., 2018; Scheffer, 2009).

Our analysis is based on an individual-based model that describes the dynamics of the system under consideration and this approach should have general applicability. The mean-field description of this model necessarily includes a quadratic term. In other work (Abraham, 1991; Klose et al.,

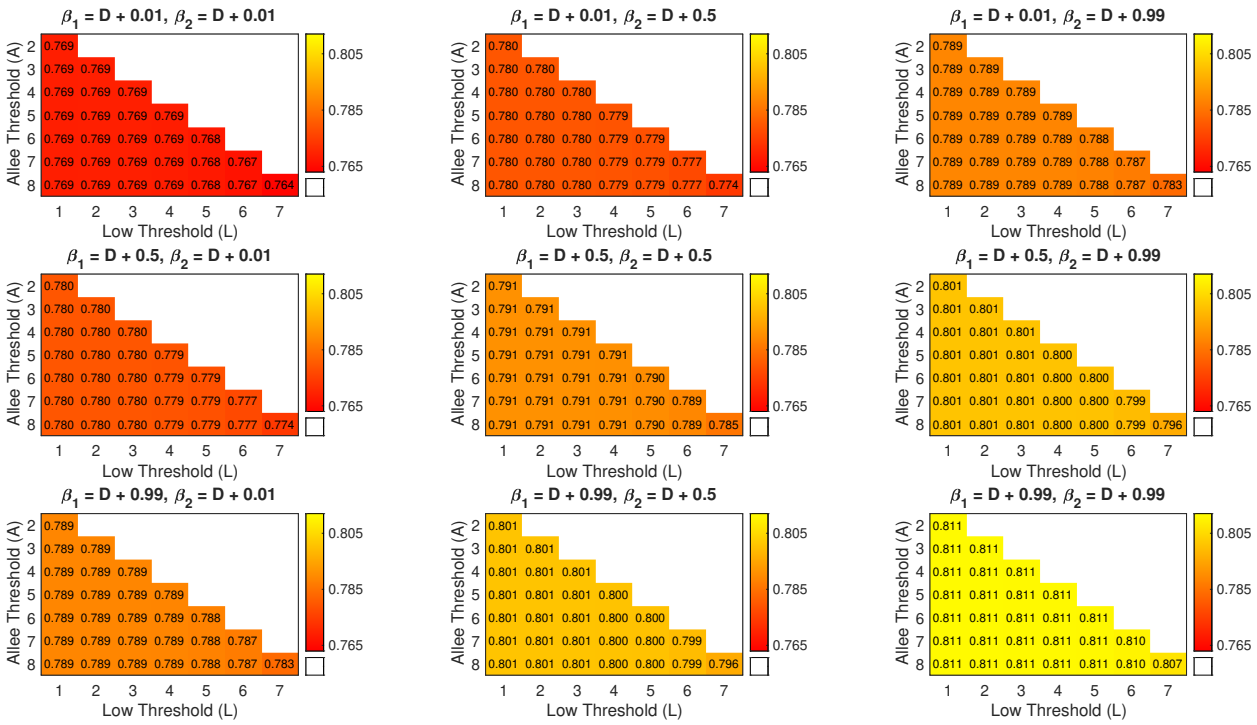


FIGURE 2.8. **Likelihood of positive tipping in the presence of high dispersal ($D = 0.99$), with $H = N$.** A visualization of the case of high dispersal with a high threshold ($H$) corresponding to the carrying capacity. The combinations of $A$ and $L$ are shown explicitly. Each heatmap shows the value of $p$, the probability of system recovery, corresponding to a combination $(\beta_1, \beta_2, A, L)$ for $D = 0.99$ and $H = N$.

2020), the proposed tipping element omits the quadratic term, in an attempt to describe a dangerous bifurcation in the form of a cusp catastrophe. This would correspond to zero mortality due to natural causes in our model (i.e., $\gamma = 0$). Similarly, the absence of the quadratic term would indicate that both the carrying capacity and Allee threshold for either population are identically zero (Johnson and Hastings, 2018). Thus, we see that important details of the underlying mechanisms of a tipping element can be lost in a phenomenological description.

Ways to generalize our work include looking at more than two populations which would allow the study of how specific forms of connectivity could play a role in tipping cascades, or introducing the possibility of more complex dynamics (Strogatz, 2015). The novelty of the emulator framework introduced here would be unaffected by the inclusion of additional dimensions, or patches, since the required (but modified) mapping procedure to store matrix elements in memory would remain valid. Allowing for patch heterogeneity in the two populations by distinguishing their stochastic

reaction rates could also produce interesting dynamics. We leave the exploration of these aspects to future work. Given the ubiquity of Allee effects (Courchamp et al., 2008) and the generality of our model, we believe that we have uncovered important ecological conclusions that are robust and should apply in a variety of settings. Within the field of landscape ecology, rescue effects are important in both metapopulations and species augmentation efforts. Another potential area of application is network theory.

## 2.7. Acknowledgements

The authors would like to thank the anonymous referee for extensive and valuable feedback that improved the manuscript.

CHAPTER 3

# Tipping cascades in a multi-patch system with noise and spatial coupling

## 3.1. Abstract

Forecasting tipping points in spatially extended systems is a key area of interest to ecologists. A slowly declining spatially distributed population is an important example of an ecological system that could exhibit a cascade of tipping points. Here, we developed a spatial two-patch model with environmental stochasticity that is slowly forced through population collapse, in the presence of changing environmental conditions. We began with a basic spatial model, then introduced a fast-slow version of the model using geometric singular perturbation theory, followed by the inclusion of stochasticity. Using the spectral density of the fluctuating subpopulation in each patch, we derived analytic expressions for candidate indicators of population extinction and evaluated their performance through a simulation study. We found that coupling and spatial heterogeneity decrease the magnitude of the proposed indicators in coupled populations relative to isolated populations. Moreover, the degree of coupling dictates the trends in summary statistics. We conclude that this theory may be applied to other contexts, including the control of invasive species.

## 3.2. Introduction

Complex systems can have thresholds, referred to as tipping points or catastrophic bifurcations, that mark an abrupt shift to an alternate dynamic regime. Such systems have been actively studied across a wide range of fields (Scheffer, 2009), including ecology (Boerlijst et al., 2013; Carpenter et al., 2011; Hastings and Wysham, 2010; Pace et al., 2015; Scheffer et al., 2015), financial systems (Battiston et al., 2016; May et al., 2008; Tu et al., 2020), climate science (Boulton and Lenton, 2015; Dakos et al., 2008; Lenton, 2020) and medicine (Maturana et al., 2020; Meisel et al., 2015; van de Leemput et al., 2014). Detecting tipping points and predicting their associated dynamics presents

significant challenges, because system observables may show negligible changes until the point of no return is reached. Since a series of tipping points can manifest through domino dynamics, as a unidirectional type of tipping cascade, there is an urgent need to adequately address these challenges. Fortunately, a new research frontier has emerged, harnessing noise as an informer of the sophisticated and often counterintuitive dynamics of interconnected systems.

A major advancement in this area is the development of early-warning signals (EWS), a suite of statistical tools that are independent of model assumptions or parameterization (Dakos et al., 2012). Instead, they capture generic changes in statistical metrics that occur prior to a bifurcation. The ability to characterize bifurcations is crucial in order to glean insight into upcoming qualitative changes in a system's behavior. For example, in ecology, populations subject to Allee effects may be described in terms of saddle-node (or fold) bifurcations. Most EWS are rooted in the phenomenon of "critical slowing down", which is a generic property of local bifurcations (Strogatz, 2015; Wissel, 1984). Akin to a second-order phase transition, critical slowing down (CSD hereafter) results in a longer return time to equilibrium following a perturbation. In ecology, CSD is used as a measure of resilience, the ability of a system to tolerate disturbances and restructure itself while responding to change (Scheffer, 2009). In the presence of stochasticity, this manifests as an increase in variance, larger temporal correlations, and marked changes in several other statistical measures. Rising variance and lag-1 autocorrelation are commonly used EWS that have been demonstrated in empirical settings (Dai et al., 2012; Dakos et al., 2008; Wouters et al., 2015). These statistics can be derived in linearized models by using stochastic differential equations (Gardiner, 2004), but theory for multi-dimensional systems on the verge of tipping has not been clearly elucidated. Moreover, the observability of EWS in real, multi-dimensional networks can be remarkably limited (Boerlijst et al., 2013), underscoring the need for a coherent theory of such systems.

To understand how CSD manifests in a multi-patch system, patch-specific temporal predictors are required. These predictors can also be used to assess whether a single patch can have a clear signal of an impending tipping cascade, or whether every patch needs to be individually monitored. To our knowledge, a predictive theory for temporal statistics of tipping elements that accounts for both stochasticity and coupling is currently lacking. It must be noted, however, that O'Regan made significant headway towards building this theory, although for a metapopulation with logistic

growth rates (O'Regan, 2018). Thus, the system investigated in that study corresponded to a non-catastrophic, transcritical bifurcation, implying a lack of hysteresis in the dynamics.

Ecological networks are inherently spatial and multi-dimensional, but the influence of space and coupling on tipping points is as yet unclear. Several summary statistics have been proposed as multivariate spatial indicators, such as spatial variance, spatial skewness, and spatial kurtosis (Guttal and Jayaprakash, 2009; Kéfi et al., 2014). However, spatial statistics are obtained using temporal snapshots of the system under consideration (Carpenter and Brock, 2010). For example, the technique of remote sensing may provide higher sensitivity at a lower computational cost than the processing of time series with high frequency. Also, spatial statistics yield information by averaging within patches, which might be less accurate in the presence of patch heterogeneity. In addition, from a theoretical standpoint, spatial statistics are usually difficult to obtain analytically. Thus, temporal indicators that are specific to each patch are necessary to anticipate tipping in connected ecological systems.

To address the aforementioned gap in the literature, we model a metapopulation with Allee effects as a multi-dimensional system in continuous time, where each subpopulation gradually approaches extinction as a result of patch quality evolving over ecological timescales. Gradually degraded metapopulations on the brink of population collapse are an important example of a spatial system that can exhibit a tipping point. Mathematically, a metapopulation that grows locally via Allee effects is characterized by a (codimension-one) saddle-node bifurcation at the tipping point. We address the question of how temporal statistics for subpopulation fluctuations can yield insight into whether or not a metapopulation is losing stability. We extend the framework to explore the effects of spatial heterogeneities on predicting extinction. We also check whether both patches exhibit EWS of tipping, or whether partial information (i.e., one patch) is sufficient to inform system management. Finally, we suggest that this theory of Allee effects and stochasticity can be applied to the control of invasive species, including insect pests (Liebhold et al., 2016).

### 3.3. Model Description

Models of Allee effects with passive dispersal have been discussed in the literature (Amarasekare, 1998; Kang and Lanchier, 2011). For an overview, consult Chapter 3 of a classic reference on Allee effects (Courchamp et al., 2008).

**3.3.1. Base model.** We begin our model formulation with the deterministic skeleton for the nondimensionalized model described by Johnson and Hastings, reproduced here for convenience (Johnson and Hastings, 2018).

$$\begin{aligned} \frac{\mathrm{d}x_1}{\mathrm{d}t} &= x_1(\beta_1 - (x_1 - 1)^2) + d(x_2 - x_1) \\ \frac{\mathrm{d}x_2}{\mathrm{d}t} &= x_2(\beta_2 - (x_2 - 1)^2) + d(x_1 - x_2) \end{aligned} \tag{3.1}$$

In the model above, the parameter $\beta_i$ represents a measure for the quality of the environment by the population denoted by $x_i$. The parameter $d$ denotes passive, symmetric diffusion in the system and is a measure of network connectivity. See Johnson's work for a detailed exposition of the nondimensionalization.

Here, $x_i \geq 0$ for $i = 1, 2$ denotes the density of subpopulation $i$ that inhabits patch $i$. In the absence of dispersal, subpopulation dynamics are determined by Allee effects at the rate $x_i(\beta_i - (x_i - 1)^2)$ in each patch. The model allows for both homogeneity in intrinsic dynamics ($\beta_1 = \beta_2 = \beta$) and spatial heterogeneity in the environment ($\beta_1 \neq \beta_2$). The positive steady-state of the spatially heterogeneous model $(x_1^*, x_2^*)$ can be obtained numerically.

In the absence of coupling, each population is isolated. If $\beta_i < 0$, population extinction is certain due to the presence of a *fatal* Allee effect. At $\beta_i = 0$, a saddle-node bifurcation occurs. For $0 < \beta_i < 1$, each population is bistable with a positive steady-state at $x_i = 1 + \sqrt{\beta_i}$ and a stable population extinction state at $x_i = 0$, owing to a *strong* Allee effect. At $\beta_i = 1$, a transcritical bifurcation occurs. Finally, for $\beta_i > 1$, the extinction state becomes unstable in the regime of the *weak* Allee effect.

In the bistable regime, if environmental conditions are homogeneous (i.e., $0 < \beta_1 = \beta_2 = \beta < 1$) and the subpopulations disperse at a rate $d > 0$, the system has two spatially homogeneous steady-states: a positive steady-state $(x_1^*, x_2^*) = (1+\sqrt{\beta}, 1+\sqrt{\beta})$ and an extinction state at $(x_1^*, x_2^*) = (0, 0)$.

The eigenvalues of the spatially homogeneous system (3.1) are $-2(\sqrt{\beta}+\beta)$ and $-2(\sqrt{\beta}+\beta+d)$. If the quality of the environment in each patch is degraded, we assume that $\beta$ declines. Therefore, both eigenvalues will decrease in magnitude, and extinction will occur in both patches when the dominant eigenvalue $-2(\sqrt{\beta}+\beta)$ is equal to zero. Hence, critical slowing down prior to population extinction is predicted in the bistable regime of the spatially homogeneous system.

Henceforth, we focus our analyses on the case of the *strong* Allee effect that gives rise to bistability.

**3.3.2. Fast-slow model.** To study the system's approach toward a catastrophic collapse, we use a fast-slow model to model the approach to the tipping point. In the spatially homogeneous system, this necessitates that $\beta$ declines slowly relative to the dynamics within each patch. Thus, we modify model (3.1) to account for a slowly varying quality of environment,

$$\begin{aligned} \frac{\mathrm{d}x_1}{\mathrm{d}t} &= x_1(\beta-(x_1-1)^2)+d(x_2-x_1) \\ \frac{\mathrm{d}x_2}{\mathrm{d}t} &= x_2(\beta-(x_2-1)^2)+d(x_1-x_2) \\ \frac{\mathrm{d}\beta}{\mathrm{d}t} &= -\beta_0 \end{aligned} \tag{3.2}$$

where $\beta_0 > 0$ quantifies the rate of change of the parameter $\beta$ in each patch. By Fenichel's Theorem (Berglund and Gentz, 2006; Fenichel, 1979; Kuehn, 2015), as $\beta_0 \to 0$, the trajectories of system (3.2) approach those of the model where $\beta$ remains constant. Since $\beta$ evolves much more slowly than the population dynamics, we assume that $0 < \beta_0 \ll 1$, and that deteriorating conditions yield a linear decline in $\beta$,

$$\beta(t) = \beta - \beta_0 t, \tag{3.3}$$

with $t^* = \beta/\beta_0$ denoting the time at which $\beta(t)$ becomes zero.

In the presence of spatial heterogeneity, the quality of one patch may differ from that of its counterpart. Thus, the underlying growth rates for both patches may be distinct. So, we assume that environmental conditions stay constant in the first patch but that the second patch is slowly degraded, effectively decreasing its population growth rate. This set of assumptions yields the

following model,

$$\begin{aligned} \frac{\mathrm{d}x_1}{\mathrm{d}t} &= x_1(\beta_1 - (x_1 - 1)^2) + d(x_2 - x_1) \\ \frac{\mathrm{d}x_2}{\mathrm{d}t} &= x_2(\beta_2 - (x_2 - 1)^2) + d(x_1 - x_2) \\ \frac{\mathrm{d}\beta_2}{\mathrm{d}t} &= -\beta_0 \end{aligned} \tag{3.4}$$

with

$$\beta_2(t) = \beta_2 - \beta_0 t, \tag{3.5}$$

where $t^* = \beta_2/\beta_0$ indicates the time that $\beta_2(t)$ becomes zero. By Fenichel's theorem (Berglund and Gentz, 2006; Fenichel, 1979; Kuehn, 2015), for sufficiently small $\beta_0$, the dynamics of the fast-slow system approach those of the system where $\beta_2$ is fixed at a constant value. Models (3.2) and (3.4) can be combined as

$$\begin{aligned} \frac{\mathrm{d}x_1}{\mathrm{d}t} &= x_1(\beta_1(t) - (x_1 - 1)^2) + d(x_2 - x_1) \\ \frac{\mathrm{d}x_2}{\mathrm{d}t} &= x_2(\beta_2(t) - (x_2 - 1)^2) + d(x_1 - x_2) \end{aligned} \tag{3.6}$$

where $\beta_1(t) = \beta_2(t) = \beta(t)$ in the case of spatial homogeneity (see (3.2) and (3.3)). In the spatially heterogeneous scenario, we assume that $\beta_1(t) = \beta_1$ and that $\beta_2(t)$ is defined by (3.5).

**3.3.3. Stochastic model.** We now derive a system of Itô stochastic differential equations (SDEs) that describes spatially homogeneous metapopulations by assuming that exogenous noise can influence patch dynamics.

3.3.3.1. *Multiplicative noise.* Following the derivation in previous work (O'Regan, 2018), and assuming that $\sigma_\mu$ is identical for both patches, we obtain the following system of SDEs,

$$\begin{aligned} \mathrm{d}x_1 &= (x_1(\beta_1(t) - (x_1 - 1)^2) - dx_1 + dx_2)\mathrm{d}t + \sigma_\mu x_1 \mathrm{d}W_1 \\ \mathrm{d}x_2 &= (x_2(\beta_2(t) - (x_2 - 1)^2) - dx_2 + dx_1)\mathrm{d}t + \sigma_\mu x_2 \mathrm{d}W_2 \end{aligned} \tag{3.7}$$

Since random disturbances scale with the population density $x_i$ in each patch, system (3.7) describes a model with multiplicative noise. Note that system (3.7) is a stochastic analogue of the fast-slow system (3.6).

3.3.3.2. *Simulations of the homogeneous stochastic models.* To study the behavior of the stochastic fast-slow model as the tipping point is approached, we simulated the model using the parameters in Table 3.1. Fig. 3.1 shows realizations of the $x_1$ subpopulation in isolated patches ($d = 0$), as compared to simulations of systems where the $x_1$ population is coupled to another patch, through low and high dispersal, and under homogeneous environmental conditions. Coupling patches through dispersal dampens the environmental fluctuations in each patch, as compared to the case of no dispersal. When coupling is low, and intrinsic dynamics are equal in each patch, coupled populations fluctuate on a similar level as that of isolated populations. When coupling is high, fluctuations are dampened due to the presence of coupling.

| Parameter | Symbol | Value (per unit time) |
|---|---|---|
| Coupling strength (high level of dispersal) | $d_h$ | 1 |
| Coupling strength (moderate level of dispersal) | $d_m$ | 0.1 |
| Coupling strength (low level of dispersal) | $d_l$ | 0.01 |
| Multiplicative noise level | $\sigma_\mu$ | 0.05 |
| Initial value of measure of patch quality (homogeneous model) | $\beta$ | 0.99 |
| Measure of patch quality (strong source patch 1) | $\beta_1$ | 0.99 |
| Measure of patch quality (weak source patch 1) | $\beta_1$ | 0.2 |
| Initial value of measure of patch quality (in deteriorating patch 2) | $\beta_2$ | 0.99 |
| Rate of change of measure of patch quality (deteriorating patch) | $\beta_0$ | 0.001 |
| Initial value of population $x_i$ (homogeneous system) | $x_i(0)$ | $1+\sqrt{0.99}$ |
| Initial value of population $x_1$ (strong source patch) | $x_1(0)$ | $1+\sqrt{0.99}$ |
| Initial value of population $x_1$ (weak source patch) | $x_1(0)$ | $1+\sqrt{0.2}$ |
| Initial value of population $x_2$ value (deteriorating patch) | $x_2(0)$ | $1+\sqrt{0.99}$ |

TABLE 3.1. **Parameter values used for numerical simulations.**

## 3.4. Analytic derivations

In order to predict subpopulation extinction using time series data, we aim to understand the nature of subpopulation fluctuations with temporal leading indicator statistics. In this section, we will show that three indicator statistics change systematically as tipping becomes increasing likely, as a direct consequence of critical slowing down. The steady-state here is chosen as the mean of the quasi-stationary population distribution. Consequently, we set $\beta_i(t) = \beta_i$ in model (3.7) and quantify the behavior of fluctuations in the vicinity of the positive steady-state $(x_1^*, x_2^*)$ of model (3.1). Although the fast-slow model assumes that the mean evolves slowly through time,

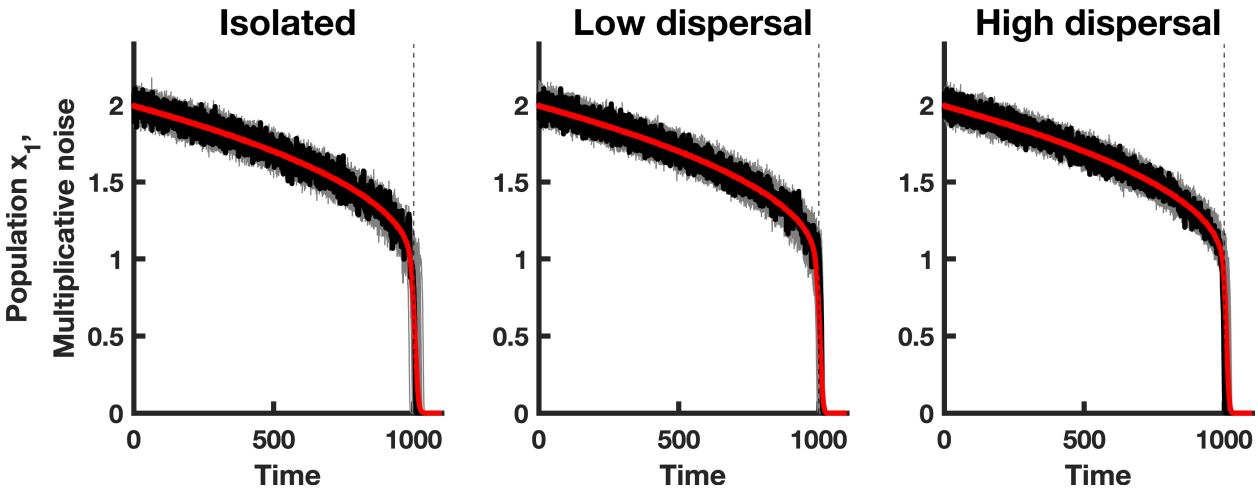


FIGURE 3.1. **Simulations of population $x_1$ in a homogeneous coupled patch system.** The red line shows the mean of 500 realizations of the homogeneous model, a single realization is shown in black and 50 simulations of the $x_1$ population are shown in gray. The dashed vertical line indicates the time $t^*$ at which the saddle-node bifurcation occurs. The first column shows simulations of isolated populations ($d = 0$), the second column corresponds to simulations of populations coupled through low dispersal levels ($d = 0.01$), and the last column shows simulations of populations coupled through high dispersal ($d = 1$). Numerical values for the parameters used in the simulations are provided in Table 3.1.

the steady-state is a faithful approximation of the mean of the fast-slow models, provided that the intrinsic growth rate for each patch changes sufficiently slowly.

To derive summary statistics for fluctuations about the positive steady-state, we note that we can express system (3.7) as follows,

$$\mathrm{d}x(t) = f(x(t),t)\mathrm{d}t + \sqrt{D(x(t),t)}\mathrm{d}W(t), \tag{3.8}$$

where $x(t) = (x_1, x_2)$, the terms of the mean vector $f(x(t),t)$ are $f_i(x(t),t) = x_i(\beta_i(t) - (x_i - 1)^2) - dx_i + dx_j$ and the entries of the variance-covariance matrix $D(x(t),t)$ are $D_{ii}(x(t),t) = \sigma_\mu^2 x_i^2$. The probability distribution $P(x(t),t)$ of the solutions of system (3.8) satisfies the forward Kolmogorov

equation (Allen, 2010; O'Regan, 2018),

$$\begin{aligned}\frac{\partial P(x(t),t)}{\partial t} &= -\sum_{i=1}^{2}\frac{\partial}{\partial x_i}[f_i(x(t),t)P(x(t),t)] \\ &\quad + \frac{1}{2}\sum_{i=1}^{2}\sum_{j=1}^{2}\frac{\partial^2}{\partial x_i \partial x_j}[D_{ij}(x(t),t)P(x(t),t)]\end{aligned} \tag{3.9}$$

**3.4.1. Model linearization.** To characterize the behavior of fluctuations near the positive steady-state, we perform a Taylor expansion of the terms in the mean vector and covariance matrix about $(x_1^*, x_2^*)$, and truncate at leading-order,

$$\begin{aligned}f_i(x_1,x_2,t) &\approx f_i(x_1^*,x_2^*,t) + \frac{\partial f(x_1^*,x_2^*,t)}{\partial x_1}z_1 + \frac{\partial f(x_1^*,x_2^*,t)}{\partial x_2}z_2 + \dots \\ &\approx 0 + \sum_{j=1}^{2} a_{ij}z_j \dots,\end{aligned} \tag{3.10}$$

where $a_{ij}$ refers to the partial derivatives of $f_i$ and $z_i = x_i - x_i^*$ denotes perturbations from the steady-state. Similarly,

$$D_{ij}(x_1,x_2,t) \approx D_{ij}(x_1^*,x_2^*,t) + \dots \tag{3.11}$$

The entries $a_{ij}$ of the Jacobian matrix are given by $a_{ii} = \beta_i - d - 1 + 4x_i^* - 3(x_i^*)^2$ and $a_{ij} = d$, for $i \neq j$, and the terms of the variance-covariance matrix are $D_{ii} = \sigma_\mu^2 (x_i^*)^2$. The joint probability distribution of fluctuations $z(t) = (z_1, z_2)$ from the steady-state satisfies

$$\begin{aligned}\frac{\partial \Pi(z(t),t)}{\partial t} &= -\sum_{i=1}^{2}\frac{\partial}{\partial z_i}\Pi(z(t),t))\left(\sum_{j=1}^{2}a_{ij}z_i\right) \\ &\quad + \frac{1}{2}\sum_{i=1}^{2}\sum_{j=1}^{2}\frac{\partial^2}{\partial z_i \partial z_j}[D_{ij}\Pi(z(t),t)]\end{aligned} \tag{3.12}$$

Solutions of the following system of stochastic differential equations,

$$\begin{aligned}\mathrm{d}z_1 &= (a_{11}z_1 + a_{12}z_2)\mathrm{d}t + \sqrt{D_{11}}\mathrm{d}W_1 \\ \mathrm{d}z_2 &= (a_{21}z_1 + a_{22}z_2)\mathrm{d}t + \sqrt{D_{22}}\mathrm{d}W_2\end{aligned} \tag{3.13}$$

share the same probability distribution $\Pi(z(t),t)$ (Allen et al., 2008; O'Regan, 2018).

**3.4.2. Spectral density.** To derive leading indicators of extinction, we begin with the spectral density of the fluctuating subpopulation within each patch. The technique of Fourier transformation can be used to obtain this function. For the full derivation, we refer the interested reader to prior work (Nisbet and Gurney, 1982; O'Regan, 2018).

Briefly, we note that any continuous function $z(t)$ defined for a time-period $-\infty \leq t \leq \infty$ may be expressed in terms of its Fourier transform $\widetilde{z}(\omega)$,

$$z(t) = \frac{1}{2\pi} \int_{-\infty}^{\infty} \widetilde{z}(\omega) \exp(i\omega t)\ \mathrm{d}\omega, \tag{3.14}$$

with $\omega$ denoting angular frequency. The Fourier transform of $z(t)$ is then given by

$$\widetilde{z}(\omega) = \int_{-\infty}^{\infty} z(t) \exp(-i\omega t)\ \mathrm{d}t. \tag{3.15}$$

We rewrite system (3.13) in a form that lends itself to the method of Fourier transformation,

$$\begin{aligned} \frac{\mathrm{d}z_1}{\mathrm{d}t} &= a_{11}z_1(t) + a_{12}z_2(t) + \sqrt{D_{11}}\Gamma_1(t), \\ \frac{\mathrm{d}z_2}{\mathrm{d}t} &= a_{21}z_1(t) + a_{22}z_2(t) + \sqrt{D_{22}}\Gamma_2(t), \end{aligned} \tag{3.16}$$

where $\Gamma_1(t)$ and $\Gamma_2(t)$ denote white noise processes associated with the covariance matrix $\{D_{ij}\}$. Fourier transformation of system (3.16) yields,

$$\begin{aligned} i\omega\widetilde{z}_1(\omega) &= a_{11}\widetilde{z}_1(\omega) + a_{12}\widetilde{z}_2(\omega) + \sqrt{D_{11}}\widetilde{\Gamma}_1(\omega), \\ i\omega\widetilde{z}_2(\omega) &= a_{21}\widetilde{z}_1(\omega) + a_{22}\widetilde{z}_2(\omega) + \sqrt{D_{22}}\widetilde{\Gamma}_2(\omega), \end{aligned} \tag{3.17}$$

where $\widetilde{z}_1(\omega), \widetilde{z}_2(\omega), \widetilde{\Gamma}_1(\omega)$ and $\widetilde{\Gamma}_2(\omega)$ are the Fourier transforms of the functions $z_1(t), z_2(t), \Gamma_1(t)$ and $\Gamma_2(t)$, respectively. We can then obtain $\widetilde{z}_1(\omega)$ as

$$\widetilde{z}_1(\omega) = \frac{(a_{22} - i\omega)\sqrt{D_{11}}\Gamma_1(\omega)}{\delta - \omega^2 - iT\omega} - \frac{a_{12}\sqrt{D_{22}}\Gamma_2(\omega)}{\delta - \omega^2 - iT\omega}, \tag{3.18}$$

where $T$ and $\delta$ are the trace and determinant of the Jacobian matrix $\{a_{ij}\}$, respectively. Using (3.18) we can establish the spectral density of the fluctuations, which we denote by

$$S_1(\omega) = \frac{D_{11}a_{22}^2 + D_{22}a_{12}^2 + D_{11}\omega^2}{(\omega^2 - \delta)^2 + T^2\omega^2}. \tag{3.19}$$

(See the Appendix in the work by O'Regan for the complete derivation.) Similarly, the spectral density of fluctuations of the subpopulation in the second patch can be obtained as,

$$S_2(\omega) = \frac{D_{22}a_{11}^2 + D_{11}a_{21}^2 + D_{22}\omega^2}{(\omega^2 - \delta)^2 + T^2\omega^2}. \tag{3.20}$$

**3.4.3. Leading indicators in the spatially homogeneous setting.** Here, we derive analytic expressions for the variance, coefficient of variation, lag-1 autocovariance function and lag-1 autocorrelation function for the spatially homogeneous model with $0 < \beta < 1$ and $d > 0$. For the spatially homogeneous model, $a_{11} = a_{22} = -2\sqrt{\beta}(\sqrt{\beta}+1) - d$ and $a_{12} = a_{21} = d$. The spectral density of the fluctuations of the subpopulations in each patch $i$ is given by

$$S_i(\omega) = \frac{\sigma_\mu^2(1+\sqrt{\beta})^2[2\sqrt{\beta}(\sqrt{\beta}+1)+d]^2 + \sigma_a^2 d^2 + \sigma_a^2\omega^2}{(\omega^2 - [(2\sqrt{\beta}(\sqrt{\beta}+1)+d)^2 - d^2])^2 + 4(2\sqrt{\beta}(\sqrt{\beta}+1)+d)^2\omega^2} \tag{3.21}$$

To obtain the variance of the fluctuations, we integrate the spectral density over all frequencies,

$$\frac{1}{2\pi}\int_{-\infty}^{\infty} S_i(\omega)d\omega = \frac{1}{\pi}\int_0^{\infty} S_i(\omega)d\omega. \tag{3.22}$$

Evaluating this integral expression yields

$$v_\mu(\beta, d) = \frac{(\sqrt{\beta}+1)[2\sqrt{\beta}(\sqrt{\beta}+1)+d]\sigma_\mu^2}{8\sqrt{\beta}[d+\sqrt{\beta}(\sqrt{\beta}+1)]} \tag{3.23}$$

To obtain the autocovariance function, we compute

$$\frac{1}{2\pi}\int_{-\infty}^{\infty} S_i(\omega)\cos(\omega\tau)d\omega = \frac{1}{\pi}\int_0^{\infty} S_i(\omega)\cos(\omega\tau)d\omega, \tag{3.24}$$

using the evenness of $S_i(\omega)$. Integrating expression (3.24) with $\tau = 1$ gives

$$\begin{aligned} a_\mu(\beta, d) = {} & \frac{\sigma_\mu^2(\sqrt{\beta}+1)[d\exp(2d) + \sqrt{\beta} + \exp(2d)\sqrt{\beta} + \beta + \exp(2d)\beta]}{8\sqrt{\beta}[d+\sqrt{\beta}(\sqrt{\beta}+1)]} \\ & \times \exp(-2[d+\sqrt{\beta}(\sqrt{\beta}+1)]) \end{aligned} \tag{3.25}$$

Dividing this expression by the variance gives the lag-1 autocorrelation function,

$$\begin{aligned} \mathrm{acf}_1(\beta) = {} & \frac{d\exp(2d) + \sqrt{\beta} + \exp(2d)\sqrt{\beta} + \beta + \exp(2d)\beta}{d + 2\sqrt{\beta}(\sqrt{\beta}+1)} \\ & \times \exp(-2[d+\sqrt{\beta}(\sqrt{\beta}+1)]) \end{aligned} \tag{3.26}$$

It can be shown that the variance and lag-1 autocorrelation functions can be written in terms of the eigenvalues $\lambda_1$ and $\lambda_2$ of the spatially homogeneous system,

$$v_\mu(\beta, d) = \frac{\sigma_\mu^2}{16}(|\lambda_1| + |\lambda_2|)\frac{|\lambda_1|^2}{|\lambda_2|}\left(\frac{1}{1+\sqrt{2|\lambda_1|+1}}\right). \tag{3.27}$$

$$\text{acf}_1(\beta) = \frac{1}{|\lambda_1| + |\lambda_2|}[|\lambda_1|\exp(-|\lambda_2|) + |\lambda_2|\exp(-|\lambda_1|)]. \tag{3.28}$$

To find the coefficient of variation statistic for each patch, we divide the standard deviation of the fluctuations by the subpopulation mean $1 + \sqrt{\beta}$ in each patch,

$$CV_\mu(\beta, d) = \frac{\sigma_\mu\sqrt{2}}{4(1+\sqrt{\beta})}\sqrt{\frac{(1+\sqrt{\beta})(d+2\sqrt{\beta}+2\beta)}{\sqrt{\beta}(d+\beta+\sqrt{\beta})}} \tag{3.29}$$

In summary, measures of variability depend on the strength of noise. It can be seen that the leading indicators are continuous functions of $\beta$ and the dispersal parameter $d$. All leading indicator functions exist for $0 < \beta < 1$ and are defined for $d > 0$.

**3.4.4. Theoretical predictions.** Next, we are interested in the qualitative behavior of the leading indicators as patch quality is degraded, that is, as the intrinsic patch quality $\beta$ of each subpopulation approaches zero from the right, for $\beta \in (0, 1)$. Taking the limit of each expression as $\beta \to 0^+$ yields,

$$\lim_{\beta\to 0^+} v_\mu(\beta, d) = +\infty, \tag{3.30}$$

$$\lim_{\beta\to 0^+} CV_\mu(\beta, d) = +\infty, \tag{3.31}$$

$$\lim_{\beta\to 0^+} acf_1(\beta, d) = 1. \tag{3.32}$$

To better intuit the behavior of the statistics as the tipping point of the system is approached due to changes in intrinsic dynamics, we compute the first derivative of each statistic with respect to $\beta$ (Table 3.2). By calculating the first derivative of each function with respect to $\beta$, provided $d > 0$ and $0 < \beta < 1$, we find that $v_\mu(\beta, d), CV_\mu(\beta, d)$, and $acf_1(\beta, d)$ are strictly decreasing functions of $\beta$;

therefore, all of these functions increase monotonically as $\beta$ approaches zero from the right (Table 3.2). Thus, we predict strictly increasing trends in lag-1 autocorrelation, variance and coefficient of variation, as extinction is approached in each patch.

| Statistic $h(\beta,d)$ | $\frac{\partial}{\partial\beta}h(\beta,d)$ | $\frac{\partial}{\partial d}h(\beta,d)$ |
|---|---|---|
| $v_\mu(\beta,d)$ | $-\frac{\left(2\left(\sqrt{\beta}+1\right)^2\beta+d^2-2(\beta-1)\sqrt{\beta}d\right)\sigma_\mu^2}{16\beta^{3/2}\left(\beta+\sqrt{\beta}+d\right)^2}$ | $-\frac{\left(\sqrt{\beta}+1\right)^2\sigma_\mu^2}{8\left(\beta+\sqrt{\beta}+d\right)^2}$ |
| $CV_\mu(\beta,d)$ | $-\frac{(2\sqrt{\beta}+1)\left(2\left(\beta+\sqrt{\beta}\right)+d\right)\left(2\left(\sqrt{\beta}+1\right)^2\beta+d^2+2\left(\beta+\sqrt{\beta}\right)d\right)\sigma_\mu}{8\sqrt{2}\beta^2\left(\beta+\sqrt{\beta}+d\right)^3\left(\frac{(\sqrt{\beta}+1)(2(\beta+\sqrt{\beta})+d)}{\sqrt{\beta}(\beta+\sqrt{\beta}+d)}\right)^{3/2}}$ | $-\frac{(\sqrt{\beta}+1)\sigma_\mu}{4\sqrt{2}\left(\beta+\sqrt{\beta}+d\right)^2\sqrt{\left(\sqrt{\beta}+1\right)^2\left(\frac{1}{\beta+\sqrt{\beta}}+\frac{1}{\beta+\sqrt{\beta}+d}\right)}}$ |
| $acf_1(\beta,d)$ | $-\frac{\left(2e^{2d}d^2+d\left(2\left(\beta+\sqrt{\beta}\right)+\left(6\left(\beta+\sqrt{\beta}\right)+1\right)e^{2d}-1\right)+4\left(\beta+\sqrt{\beta}\right)^2\left(e^{2d}+1\right)\right)}{2\sqrt{\beta}\left(2\left(\beta+\sqrt{\beta}\right)+d\right)^2}$ $\times\left(2\sqrt{\beta}+1\right)e^{-2\left(\beta+\sqrt{\beta}+d\right)}$ | $-\frac{\left(\beta+\sqrt{\beta}\right)e^{-2(\beta+\sqrt{\beta}+d)}\left(\left(2\sqrt{\beta}+1\right)^2-e^{2d}+2d\right)}{\left(2\left(\beta+\sqrt{\beta}\right)+d\right)^2}$ |

TABLE 3.2. **First derivatives of each statistic, assuming $\beta \in (0,1)$ and $d, \sigma_\mu \in (0,\infty)$.**

To understand the effect of coupling on the behavior of the temporal leading indicators, we examine these functions as $d$ approaches zero from above, and as $d$ approaches positive infinity.

As $d$ decreases to zero from above, the limit of each statistic approaches the expression for the statistic in the case without dispersal,

$$\lim_{d\to 0^+} v_\mu(\beta,d) = \frac{\sigma_\mu^2(\sqrt{\beta}+1)}{4\sqrt{\beta}}, \tag{3.33}$$

$$\lim_{d\to 0^+} CV_\mu(\beta,d) = \frac{\sigma_\mu}{2\sqrt{\sqrt{\beta}+\beta}}, \tag{3.34}$$

$$\lim_{d\to 0^+} acf_1(\beta,d) = \exp\left[-2\sqrt{\sqrt{\beta}+\beta}\right]. \tag{3.35}$$

Consequently, the summary statistics capture the behavior of the whole system as being similar to that of isolated subsystems. If coupling increases to infinity, the limits are

$$\lim_{d\to \infty} v_\mu(\beta,d) = \frac{\sigma_\mu^2(\sqrt{\beta}+1)}{8\sqrt{\beta}}, \tag{3.36}$$

$$\lim_{d\to \infty} CV_\mu(\beta,d) = \frac{\sigma_\mu\sqrt{2}}{4\sqrt{\sqrt{\beta}+\beta}}, \tag{3.37}$$

$$\lim_{d\to\infty} acf_1(\beta, d) = \exp\left[-2\sqrt{\sqrt{\beta}+\beta}\right]. \tag{3.38}$$

Increasing the degree of patch connectivity muffles the temporal signals that quantify variability. As $d \to \infty$, the variance approaches 1/2 of the variance in the absence of dispersal. So, in a very well-mixed metapopulation, the temporal variance in each patch will be muted relative to isolated patches. Similarly, as $d$ approaches infinity, the coefficient of variation approaches $1/\sqrt{2}$ of its analogue in the absence of coupling. Table 3.2 shows that the derivative of each function decreases monotonically with $d$, provided $d > 0, \sigma_\mu > 0$, and $0 < \beta < 1$.

Notice that the lag-1 autocorrelation function approaches $\exp[-2\sqrt{\sqrt{\beta}+\beta}]$ as $\beta$ approaches either 0 or $\infty$. The first derivative of $acf_1(\beta, d)$ with respect to $d$ is

$$\frac{\partial}{\partial d} acf_1(\beta, d) = -\frac{\exp[-2(d+\sqrt{\beta}+\beta)](\sqrt{\beta}+\beta)[2d - \exp(2d) + (1+2\sqrt{\beta})^2]}{(d+2(\sqrt{\beta}+\beta))^2}$$

Provided that $d$ is strictly positive and $\beta \in (0, 1)$, there is a critical point of $acf_1(\beta, d)$ at

$$d_c = -\frac{1}{2}(1+2\sqrt{\beta})^2 - \frac{1}{2}\text{ProductLog}[-\exp[-(1+2\sqrt{\beta})^2]. \tag{3.39}$$

Applying the second derivative test shows that a local minimum of $acf_1(\beta, d)$ occurs at $d_c$,

$$\frac{\partial^2 acf_1(\beta, d_c)}{\partial^2 d} = \frac{8(\sqrt{\beta}+\beta)\exp[-2(\sqrt{\beta}+\beta)]}{\text{ProductLog}[-\exp[-(1+2\sqrt{\beta})^2]]} \times \frac{1}{(1+\text{ProductLog}[-\exp[-(1+2\sqrt{\beta})^2]])}$$

The second derivative is always positive at $d_c$, because the denominator of the expression above is strictly positive, owing to the dominance of the square term.

As a result, with low dispersal in the spatially homogeneous system, the neighboring points $x_i(t)$ and $x_i(t+1)$ in a stationary time series are highly correlated. As dispersal increases, the temporal correlation between $x_i(t)$ and $x_i(t+1)$ decreases, due to mixing between both patches. For $d > d_c$, however, autocorrelation increases because dispersal is sufficiently high to result in a single population. In summary, $x_i(t)$ and $x_i(t+1)$ are least correlated at intermediate levels of patch connectivity. For intermediate levels of dispersal, we can expect the lag-1 autocorrelation to be

lower relative to that of isolated patches, but if coupling is sufficiently high, the lag-1 autocorrelation approaches that of a single patch.

**3.4.5. Numerical predictions for the summary statistics.** Numerically evaluating the summary statistics at the mean $(x_1^*, x_2^*) = (1+\sqrt{\beta}, 1+\sqrt{\beta})$ confirms our theoretical predictions. As $\beta$ approaches zero from the right in each patch, the leading indicators change as predicted by the theory (Fig. 3.2). The presence of coupling dampens patterns in indicator statistics that measure variability. Furthermore, a high dispersal rate leads to larger changes in the lag-1 autocorrelation statistic for populations in synchrony, in contrast with isolated patches, as predicted with a decrease in $\beta$.

## 3.5. Simulation methodology

The theoretical predictions for the summary statistics in Section 3.4 are calculated about the steady-state (i.e., the subpopulation mean $(x_1^*, x_2^*) = (1 + \sqrt{\beta}, 1 + \sqrt{\beta})$). In order to test the robustness of the theoretical predictions for the leading indicator statistics under worsening patch quality, we conducted a simulation study using the fast-slow model derived in Section 3.3. Using the parameters in Table 3.1, we simulated the stochastic fast-slow model approaching a tipping point under low and high dispersal regimes, and under both spatially homogeneous (system (3.2) and (3.3)) and heterogeneous (system (3.4) and (3.5)) environmental conditions.

Here, we adopt the simulation procedure implemented in previous work (O'Regan, 2018). All computations were performed in MATLAB (MATLAB, 2021).

## 3.6. Results

Increases in lag-1 autocorrelation, variance and coefficient of variation are seen in the simulation study of the coupled two-patch model (Fig. 3.3). As the theory shows, higher dispersal levels result in decreases in the magnitude and rate of change of the trends in the indicator statistics. Median Kendall correlation coefficient values are all positive, demonstrating that on average, positive trends in indicator statistics occur as tipping is approached. Also, the median correlation coefficient values for the coefficient of variation are very close to 1, indicating that under multiplicative noise, one can expect a strong positive relationship between a worsening environment and the coefficient of

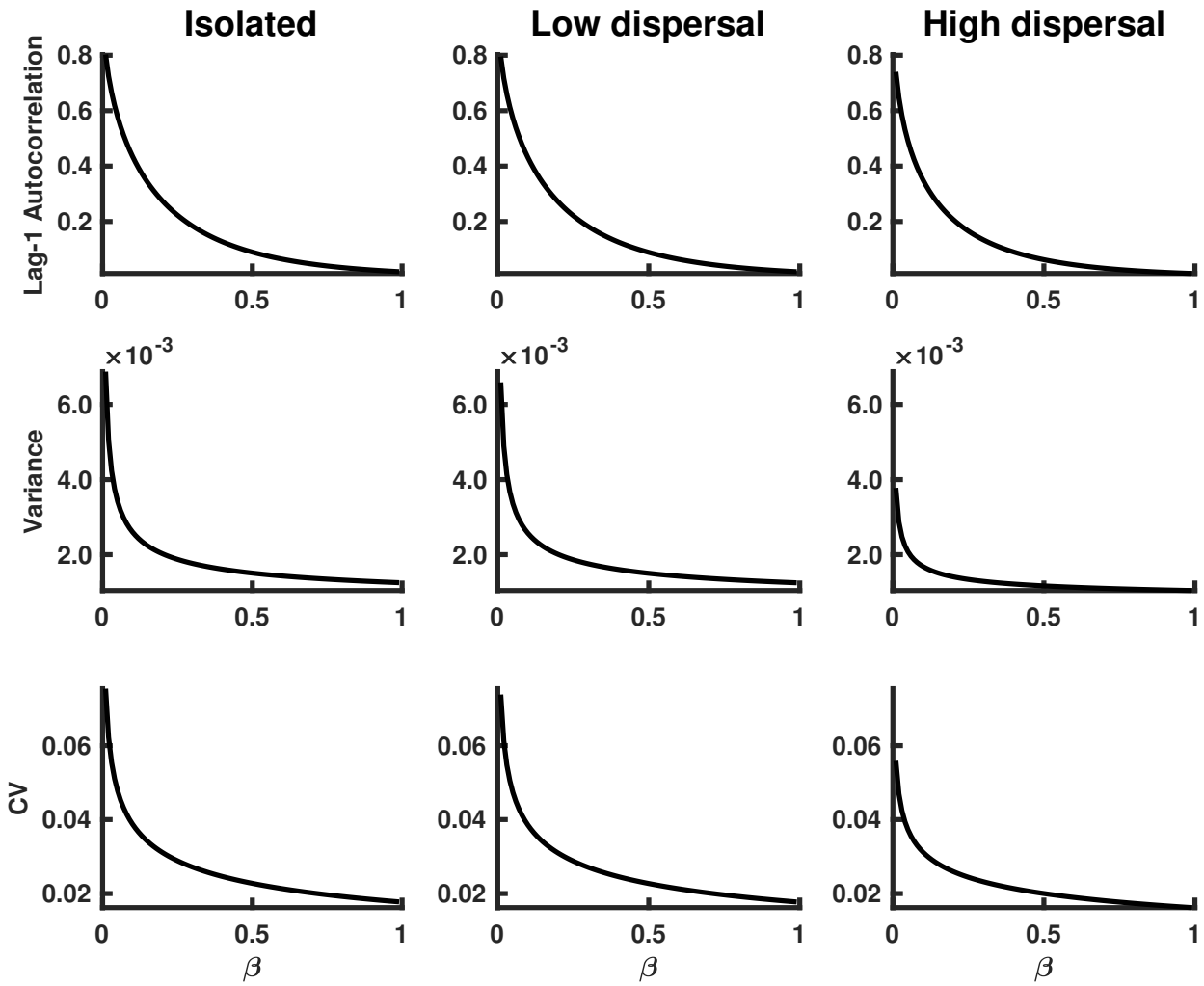


FIGURE 3.2. **Theoretical predictions for summary statistics of $x_1$ in a homogeneous coupled system.** The first column of panels shows summary statistic predictions for isolated patches, the second column of panels displays predictions for $x_1$ populations coupled through low dispersal levels, and the third column of panels corresponds to populations coupled through high dispersal. Parameter values used for the numerical predictions are given in Table 1. Predictions were calculated for fluctuations about the steady-state $(1+\sqrt{\beta}, 1+\sqrt{\beta})$ of system (3.1) (representing the mean of the stochastic fast-slow system) for $\beta$ values ranging from 0.99 down to 0.01, with a spacing of 0.01.

variation. This finding is common across dispersal levels. In summary, indicator statistics behave as predicted by the theory, with the coefficient of variation performing consistently well as an indicator of CSD across all cases explored here.

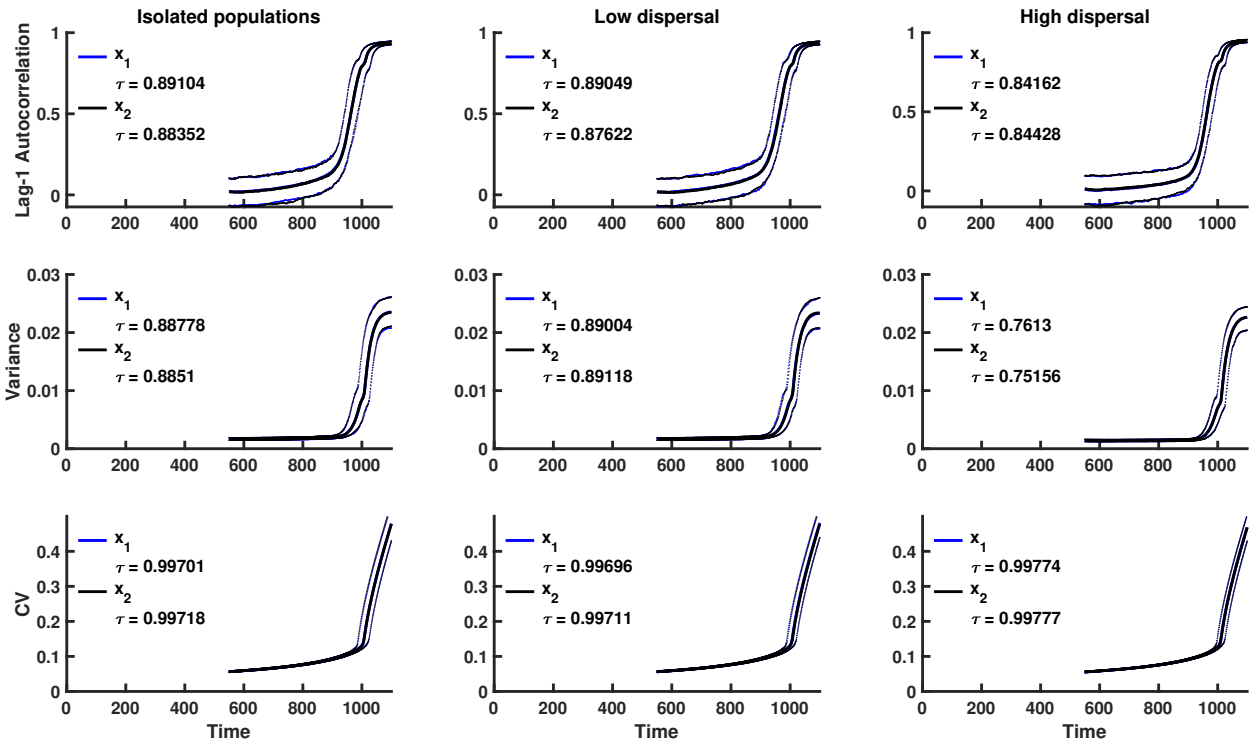


FIGURE 3.3. **Simulation study predictions for the summary statistics of the $x_1$ population in a homogeneous coupled system with multiplicative noise.** Thick blue lines indicate the median value of each statistic for population $x_1$ over 500 simulations; thick black lines correspond to the median value of each statistic for the $x_2$ population over 500 realizations. Dotted lines show the 95% prediction interval for each statistic. The median value of Kendall's correlation coefficient $\tau$ is reported for each indicator statistic over 500 simulations. The first column of panels are summary statistic predictions for isolated patches, the second column are predictions for populations coupled through low dispersal levels, and the last column shows predictions for populations coupled through high dispersal. Parameter values used for the numerical predictions are given in Table 3.1.

**3.6.1. The impact of spatial heterogeneity on CSD.** Spatial systems are generally heterogeneous in nature (Levin, 1976; O'Regan, 2018). To investigate how spatial heterogeneities affect CSD in a spatially extended dynamical system, and whether the predictions for the leading indicator statistics for the spatially homogeneous model are robust to heterogeneities, we formulated a fast-slow spatially heterogeneous model with multiplicative noise. We assumed that environmental conditions remain constant in the first patch, while conditions steadily decline in the second patch. We investigated the dynamics when patch 1 is a "strong source", meaning that the patch quality is high and population growth occurs under favorable conditions. We also explored the onset of

CSD when the first patch is a "weak source", that is, when conditions for population growth are poor, and the population is close to extinction. Fig. 3.4 shows simulations of the fast-slow model with a strong source patch and a deteriorating patch under low and high dispersal. Due to mixing between the subpopulations, both patches decline in habitat quality. Although the second patch deteriorates at the same rate as the declining patches in the spatially homogeneous system, the strong source patch exhibits a rescue effect in the regime of high dispersal. Both patches decline at similar rates due to the high level of connectivity between the subpopulations.

Similar patterns of subpopulation decline due to high levels of coupling are also observed when the first patch is depleted of resources (Fig. 3.5). When a poor quality patch is coupled with a degrading subpopulation, both subpopulations decline towards extinction and exhibit larger fluctuations compared to subpopulations where one patch has a good environment (compare Figures 3.4 and 3.5). The spatially heterogeneous metapopulation with a weak source patch appears to be more responsive to the intrinsic dynamics within each patch, because each patch has an initial transient before the system relaxes to the moving steady-state of the fast-slow system (Fig. 3.5). Initially, the subpopulation in patch 1 is buffered from extinction due to dispersal of individuals from patch 2, which has a better initial environmental quality than the second patch.

Figures 3.4 and 3.5 suggest the following hypothesis: due to a rescue effect, temporal indicators of CSD should be weaker in a spatially heterogeneous system with a strong source patch than a spatially heterogeneous system with a weak source patch. The latter system is closer to the extinction threshold, whereas the metapopulation with a strong source patch is buffered from extinction.

3.6.1.1. *Theoretical predictions.* In order to examine the behavior of leading indicators of extinction in a spatially heterogeneous system, we numerically integrated equations (3.19) and (3.20) for each steady-state value $(x_1^*, x_2^*)$ of system (3.1) (which we used to represent the mean of the stochastic fast-slow system) for $\beta_2$ values ranging between 1 and $10^{-2}$, while $\beta_1$ remained constant (Table 3.1), and we used the integrals to calculate summary statistics. Figs. 3.6 and 3.7 show the behaviors of the summary statistics as $\beta_2$ decreases towards zero from the right. In a similar manner as the spatially homogeneous system, the lag-1 autocorrelation function, variance and coefficient of variation all increase, in both patches, as environmental conditions in patch 2 decline. Moreover,

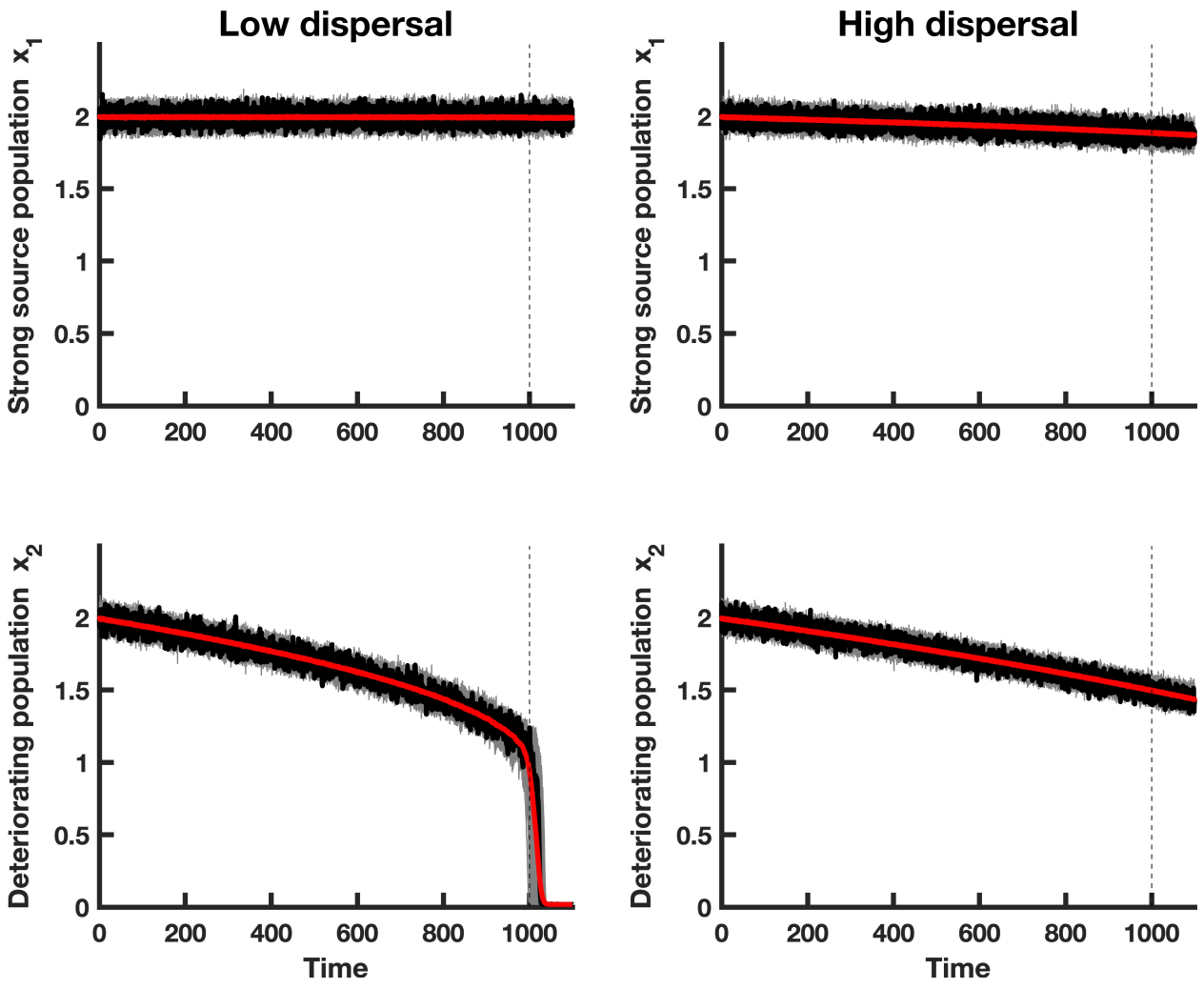


FIGURE 3.4. **Simulations of both populations, in a heterogeneous coupled patch system with multiplicative noise and a static patch with a good environment (i.e., a "strong source" patch).** The red line shows the mean of the 500 $x_i$ realizations of the heterogeneous model, a single realization is shown in black and 50 simulations of each subpopulation $x_i$ are shown in gray. The dashed vertical line indicates the time at which the saddle-node bifurcation occurs. The first column of panels displays simulations of populations coupled through low dispersal levels, and the second column corresponds to simulations of populations coupled through high dispersal. Numerical values for the parameters used in the simulations are provided in Table 3.1.

trends in leading indicators are dampened with increasing dispersal, just as predicted in the case of the spatially homogeneous system.

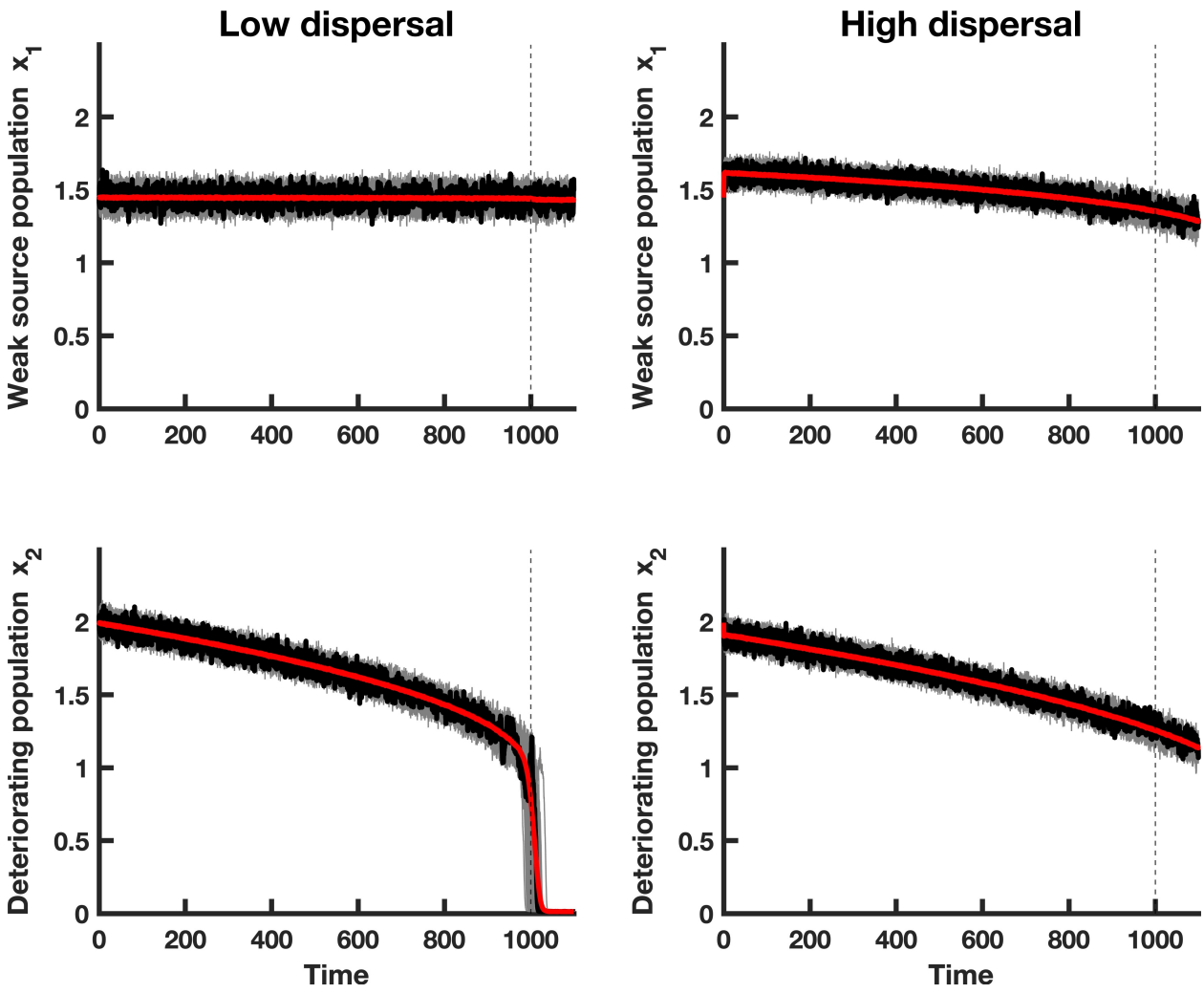


FIGURE 3.5. **Simulations of the $x_1$ and $x_2$ populations, in a heterogeneous coupled patch system with multiplicative noise and a bad environment (i.e., a "weak source" patch).** The red line shows the mean of the 500 $x_i$ realizations of the heterogeneous model, a single realization is shown in black and 50 simulations of each subpopulation $x_i$ are shown in gray. A transient is observed before the system relaxes to the moving fast-slow steady-state. The dashed vertical line indicates the time at which the saddle-node bifurcation occurs. The first column of panels shows simulations of populations coupled through low dispersal levels, and the second column corresponds to simulations of populations coupled through high dispersal. Numerical values for the parameters used in the simulations are provided in Table 3.1.

Since conditions in the second patch are deteriorating, it is reasonable to expect that subpopulation $x_2$ would exhibit a stronger sign of CSD than the $x_1$ subpopulation subject to a constant growth rate in the first patch. We find that this is indeed the case. Under low dispersal and good

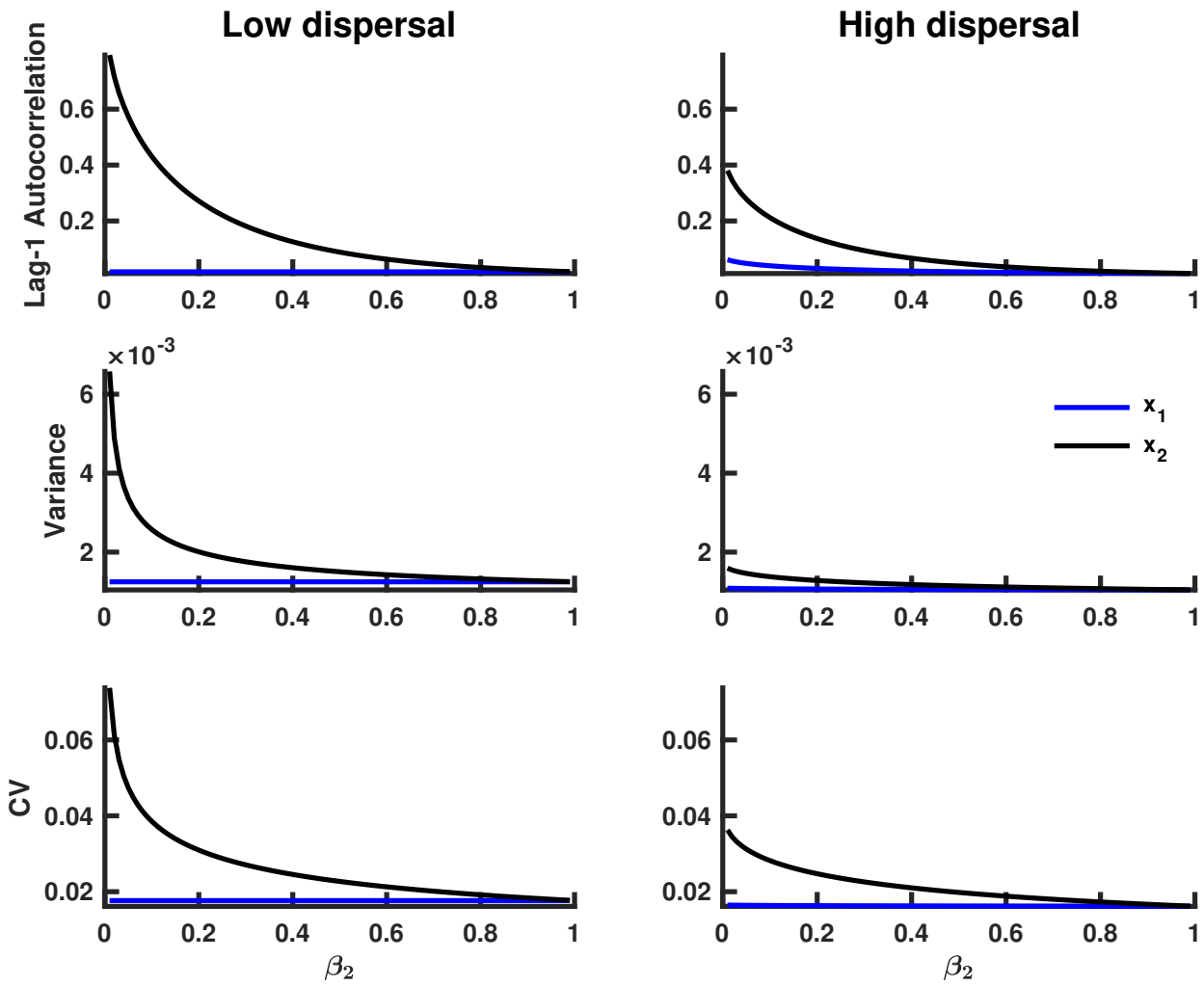


FIGURE 3.6. **Theoretical predictions for the summary statistics of a heterogeneous coupled system with multiplicative noise and a static patch with a good environment (i.e., a "strong source" patch).** The first column shows summary statistic predictions for the $x_1$ and $x_2$ subpopulations coupled through low dispersal levels, and the second column displays predictions for subpopulations coupled through high dispersal. Parameter values used for the numerical predictions are given in Table 3.1. Predictions were calculated for fluctuations about the steady-state $x_1^*, x_2^*$ of system (3.1) (representing the mean of the stochastic fast-slow system) for $\beta_2$ values ranging from 0.99 down to 0.01, with a spacing of 0.01, while $\beta_1$ remained constant at 0.99.

conditions in patch 1, $x_2$ exhibits a stronger signal of CSD than $x_1$, as indicated by the magnitude and slope of the summary statistics; this is true under high dispersal as well (Fig. 3.7).

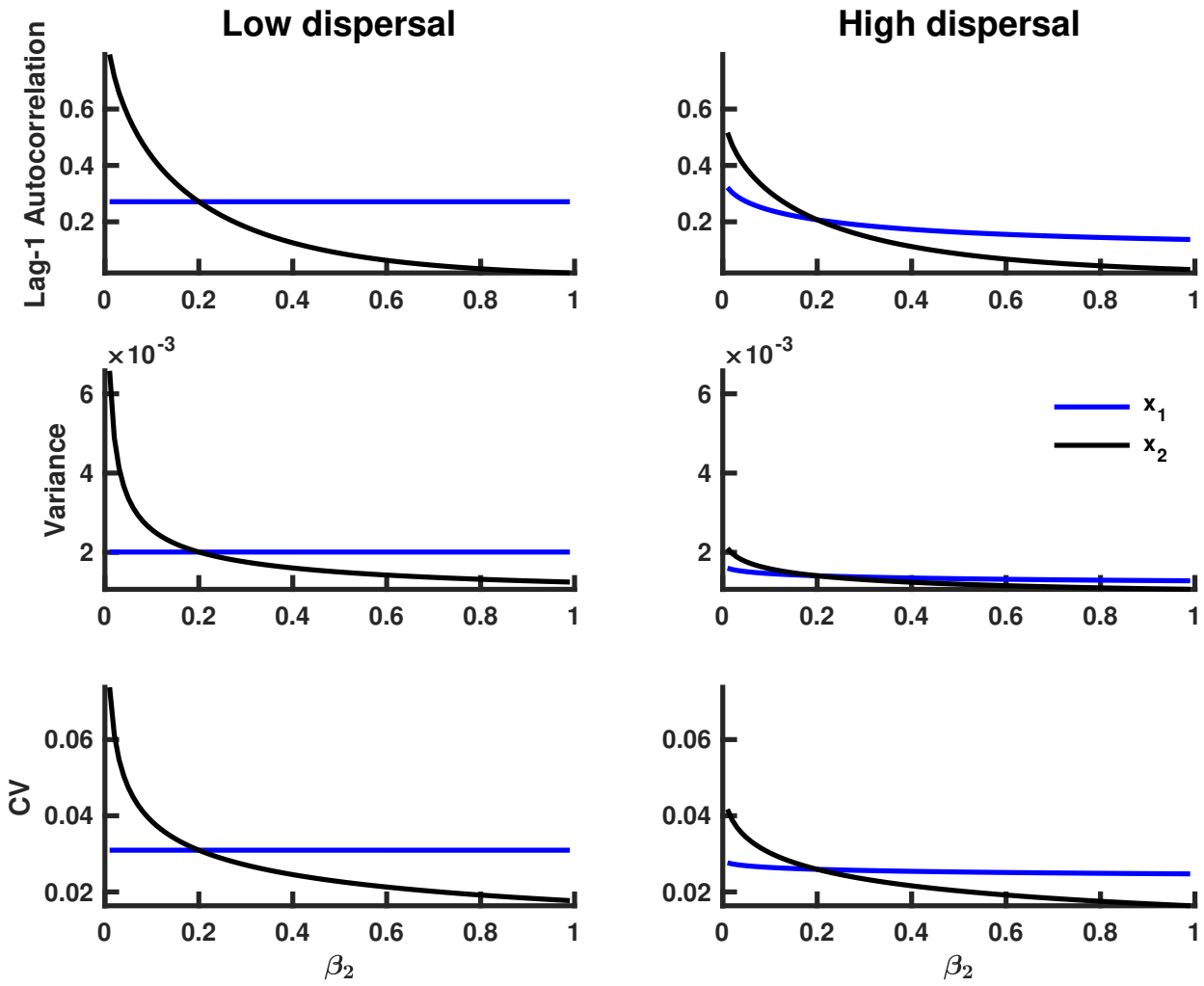


FIGURE 3.7. **Theoretical predictions for the summary statistics of a heterogeneous coupled system with multiplicative noise and a static patch with a bad environment (i.e. a "weak source" patch).** The first column shows summary statistic predictions for the $x_1$ and $x_2$ subpopulations coupled through low dispersal levels, and the second column displays predictions for subpopulations coupled through high dispersal. Parameter values used for the numerical predictions are given in Table 3.1. Predictions were calculated for fluctuations about the steady-state $x_1^*, x_2^*$ of system (3.1) (representing the mean of the stochastic fast-slow system) for $\beta_2$ values ranging from 0.99 down to 0.01, with a spacing of 0.01, while $\beta_1$ remained constant at 0.2.

Under high dispersal and poor environmental quality for the second patch, patterns in leading indicators are similar in both patches (Fig. 3.7). When dispersal is low, leading indicators obtained from population fluctuations in patch 2 change more rapidly than those obtained from patch 1 as

$\beta_2$ approaches zero from the right. Further away from the extinction point at $\beta_2 = 0$, patch 1 has larger variance, lag-1 autocorrelation and coefficient of variation due to poor conditions that make the $x_1$ subpopulation more susceptible to extinction. All of the summary statistics increase, in both patches, as $\beta_2$ approaches zero.

Comparing the magnitudes of the signals in Figures 3.6 and 3.7, we observe stronger signals of CSD in the summary statistics obtained from the spatially heterogeneous model with a weak source patch than the model with a good quality patch. These predictions suggest that the spatially heterogeneous system with a weak source patch, which is near extinction, should exhibit stronger signals of CSD than the model with a good source patch that favors system longevity.

3.6.1.2. *Simulation study predictions.* Predictions for the summary statistics calculated from the spatially heterogeneous fast-slow model over a moving window (Figures 3.8 and 3.9) confirm the predicted trends obtained by numerical integration (Figures 3.6 and 3.7). From the median $\tau$ values, there is considerably more variability in leading indicator trends than those obtained from simulations of the spatially homogeneous system (compare the median Kendall's $\tau$ values in Fig. 3.4 with those from Figures 3.8 and 3.9). Furthermore, the prediction that stronger signals of CSD are observed in the spatially heterogeneous system with a weak source patch than the corresponding system with a strong source patch is robust in the simulated models (compare $\tau$ values in Fig. 3.8 with those in Fig. 3.9). Just as in the spatially homogeneous system, the coefficient of variation appears to be the most reliable indicator of extinction.

**3.6.2. Partial observability in tipping cascades.** As discussed in Section 3.2, a given multi-patch system is likely to be observable in only one patch. We can thus explore the likelihood of a tipping cascade as follows. By defining the extinction threshold with $L := L_1 = L_2 = 0$, the Allee threshold as $A_i := 1 - \sqrt{\beta_i}$ (Johnson and Hastings, 2018), and the high threshold as $H_i := 1 + \sqrt{\beta_i}$ for $i = 1, 2$, we notice that $L_i < A_i < H_i$ in the bistable regime of the strong Allee effect. Hence, we can consider the question of whether there exists a signal for CSD in the system, given that only one patch is observable and deteriorates in quality. This amounts to checking whether or not a transition from $H_1$ to $L_1$ in the first patch is captured by the full system, with the second patch maintained at either $H_2$ or $L_2$. In other words, the cases here correspond to $(H_1, H_2) \to (L_1, H_2)$ and $(H_1, L_2) \to (L_1, L_2)$ respectively. Together, these two cases capture the

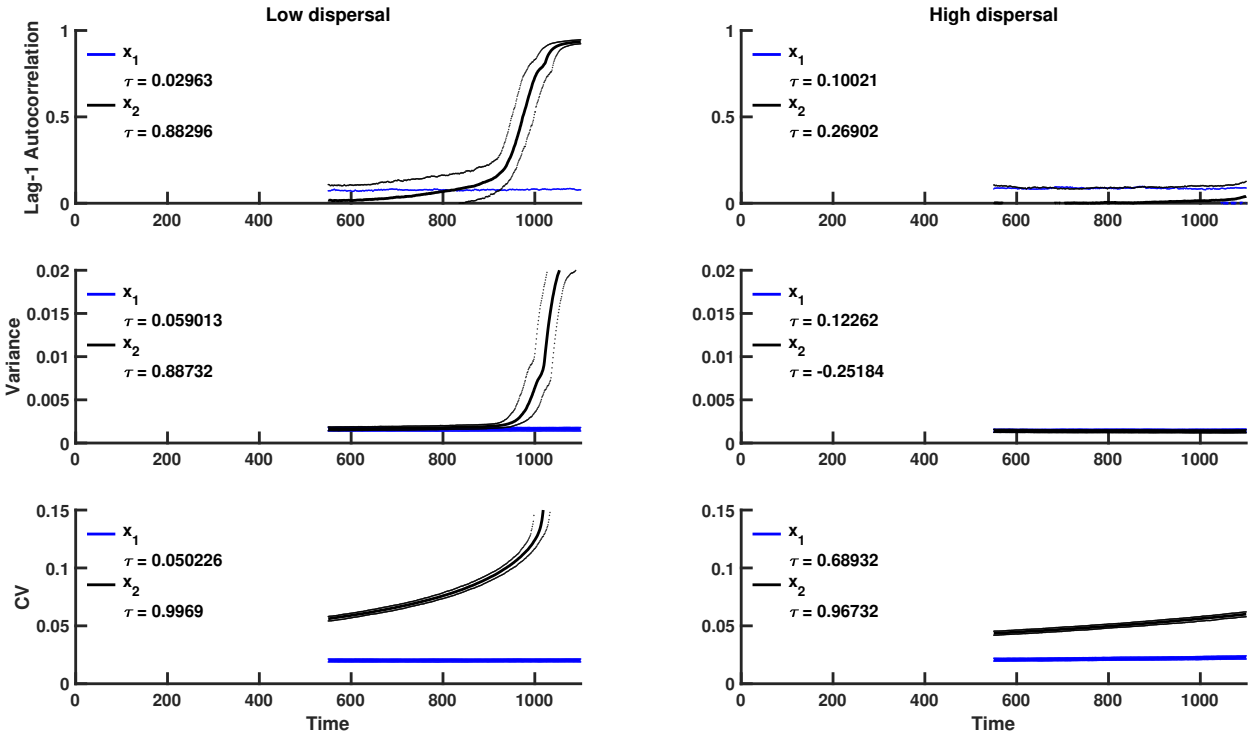


FIGURE 3.8. **Simulation study predictions for the summary statistics of the $x_1$ and $x_2$ population in a heterogeneous coupled system with multiplicative environmental noise and a static patch with a good environment (i.e., a "strong source" patch).** Thick blue lines indicate the median value of each statistic for the $x_1$ population over 500 realizations, and thick black lines indicate the median value of each statistic for the $x_2$ population over 500 simulations. Dotted lines correspond to the 95% prediction interval for each statistic. The median value of Kendall's correlation coefficient $\tau$ is reported for each indicator statistic over 500 simulations. The first column shows predictions for populations coupled through low dispersal levels, and the second column shows predictions for populations coupled through high dispersal. Parameter values used for the numerical predictions are given in Table 3.1.

scenario of a tipping cascade, whereby the system can begin at a high-high state and end in a catastrophic collapse at the low-low state (Mallela and Hastings, 2021a).

In the spatially homogeneous scenario (i.e., $\beta_1 = \beta_2 = \beta$), we note that the thresholds discussed above are the same for both patches. The expressions for the respective leading indicators are also identical across patches. Thus we can refer to expressions (3.30) to (3.32) in Section 3.4, to understand that all of the leading indicators describing CSD in the second patch have strictly

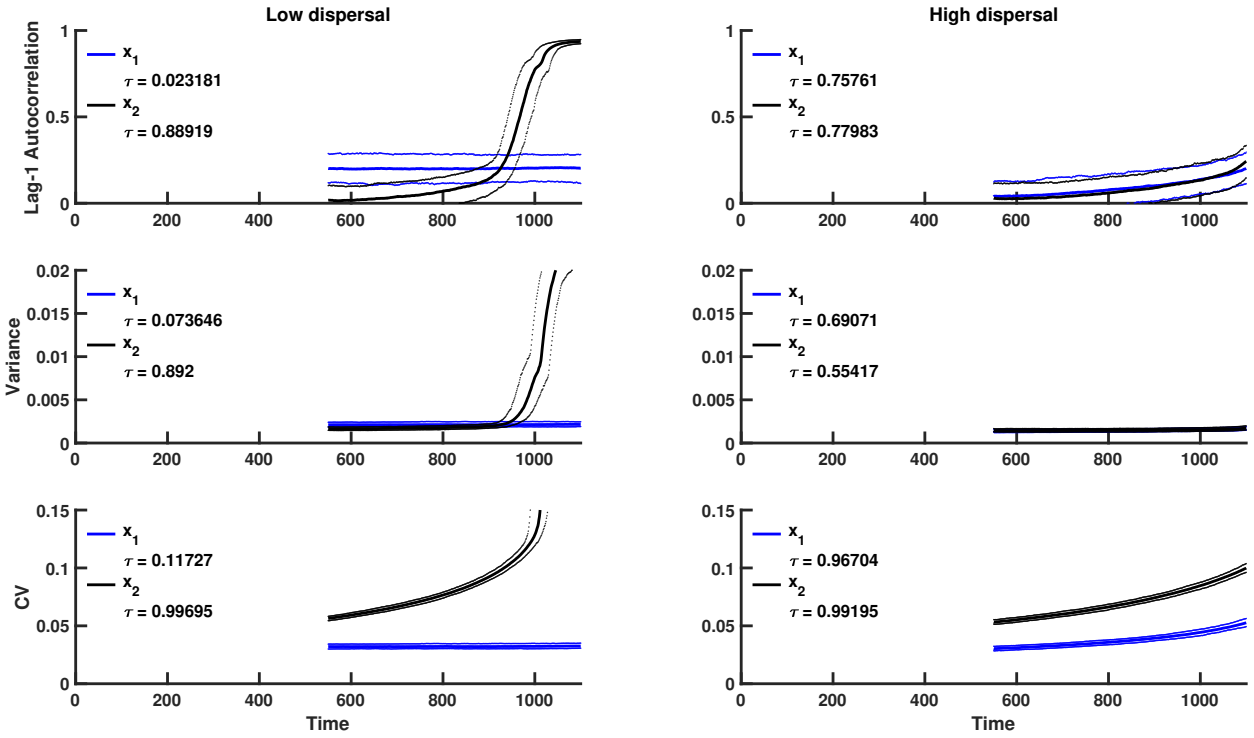


FIGURE 3.9. **Simulation study predictions for the summary statistics of the $x_1$ and $x_2$ population in a heterogeneous coupled system with multiplicative environmental noise and a static patch with a bad environment (i.e., a "weak source" patch).** Thick blue lines indicate the median value of each statistic for the $x_1$ population over 500 realization, and thick black lines indicate the median value of each statistic for the $x_2$ population over 500 simulations. Dotted lines indicate the 95% prediction interval for each statistic. The median value of Kendall's correlation coefficient $\tau$ is reported for each indicator statistic over 500 simulations. The first column shows predictions for populations coupled through low dispersal levels, and the second column displays predictions for populations coupled through high dispersal. Parameter values used for the numerical predictions are given in Table 3.1. Initial transient behavior of $x_1$ and $x_2$ (Fig. 3.5) is captured by the sharp change in statistics over the moving window.

increasing trends as extinction is approached in the first patch. Hence, observing the second patch adequately informs our assessment of the first patch.

For purposes of display, we analyze the case of multiplicative noise in the spatially heterogeneous case with $\beta_1 \neq \beta_2$ (Fig. 3.10). Increases in lag-1 autocorrelation, variance and coefficient of variation for the second patch are seen in a study of the coupled two-patch model with multiplicative noise. Lower values of $\beta_2$, reflecting a poorer quality of the second patch, result in stronger signals of CSD for the first patch. This is true across all dispersal levels. For a fixed combination of $\beta_1$ and $\beta_2$, the

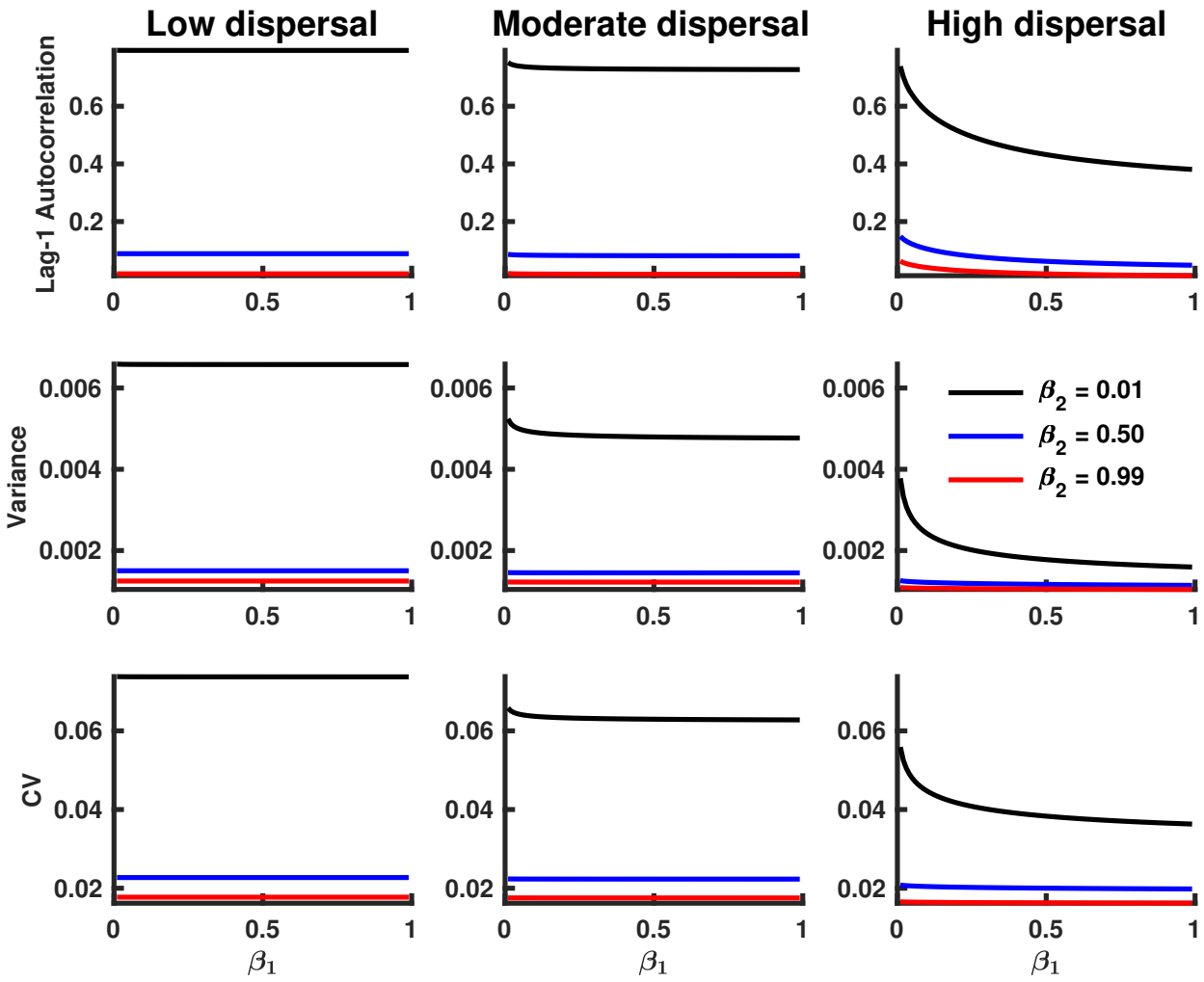


FIGURE 3.10. **Theoretical predictions for summary statistics of $x_2$ in a tipping cascade with multiplicative noise.** The first column of panels shows summary statistic predictions for populations coupled through low dispersal, the second column displays predictions for $x_1$ populations coupled through moderate dispersal, and the third column of panels corresponds to populations coupled through high dispersal. Parameter values used for the numerical predictions are given in Table 3.1. Predictions were calculated for fluctuations about the steady-state $(1+\sqrt{\beta_1}, 1+\sqrt{\beta_2})$ of the spatially heterogeneous system for $\beta_1$ values ranging from 0.99 down to 0.01, with a spacing of 0.01.

strength (magnitude) of the signal decreases with higher dispersal, for all three leading indicators. We note that our analyses here capture both directions of a tipping cascade.

## 3.7. Discussion

Predicting tipping cascades is a complex task. Temporal, patch-specific indicators are potentially useful for anticipating catastrophic events in networks with poor connectivity and environmental noise. We formulated a stochastic fast-slow two-patch model that is valid for different environmental conditions. By simulating the stochastic fast-slow model, we showed that predicted trends in the leading indicators are robust, implying that CSD manifests prior to tipping.

Noise, network connectivity and return rates to the steady-state collectively characterize the behavior of temporal summary statistics for the two-patch model studied here. Assuming spatial homogeneity, we showed that increasing the level of coupling between patches reduces signal strengths by decreasing their magnitude relative to those obtained for isolated populations. The lag-1 autocorrelation function exhibits non-monotonic behavior with increasing coupling strength. The simulation study shows that the coefficient of variation is the most robust temporal indicator across different coupling regimes, as well as for various environmental conditions. These predictions for the behavior of the leading indicators are robust even if the constraint of spatial homogeneity is relaxed. The analytic expressions derived in the homogeneous case are useful for prediction in spatially heterogeneous systems, where having patch-specific indicators that account for coupling between subsystems becomes more important.

Increasing the degree of coupling induces synchronous dynamics in both patches in the heterogeneous model. When a good quality patch is available, rescue effects due to dispersal buffer the system from a catastrophic collapse by introducing synchrony in the network dynamics. Alternatively, in the heterogeneous system with a weak source patch, the dynamics of the poor quality patch follow those of the declining subpopulation over a short transient, and both subpopulations simultaneously decrease toward extinction. These results suggest that both patches in the system should be monitored. However, we have a stronger result in the scenario of observing a tipping cascade. In particular, a signal in one patch is sufficient to inform our understanding of its counterpart (Fig. 3.10). This finding can have important implications in several settings. For example, nearly all species are buffeted by stochasticity and many of them could have Allee dynamics (Liebhold and Bascompte, 2003).

A key shortcoming of our findings relates to the limits of applicability of CSD, which forms the basis of research on early warning signals (Clements and Ozgul, 2018). As is typical of the transition from theory to practice, we must be careful when applying our methods that are rooted in bifurcation theory, to real ecological data (Burthe et al., 2016). Moreover, while CSD and its associated components of instability are present in some biological models, it is absent from several others, including systems displaying catastrophic failures (Boerlijst et al., 2013). We must also be cognizant of the fact that predictability does not necessarily allow for prevention, as the fate of the system may be unavoidable (Boettiger et al., 2013).

In addition, we used a simple model for a saddle-node bifurcation to describe the intrinsic patch dynamics, but the framework can be generalized for bistable ecosystems present in nature. For instance, accounting for spatial structure and movement pathways through networks (Suweis and D'Odorico, 2014) is a natural way to extend the two-patch model presented here. Because we are interested in the scenario of noise-induced tipping via a saddle-node bifurcation, with a smooth and gradual approach to the tipping point, extinction is highly likely. A factor that may influence the time to extinction is the dispersal rate between patches, which could lead to a rescue effect. In other words,we emphasize the importance of transient dynamics in our analyses over a finite time horizon, and do not explore persistence in the long-term dynamics of the system. We do note, however, that prior work explored the role of patch dispersion in the persistence of stochastic populations, through a linear model without Allee effects (Evans et al., 2013) and a density-dependent logistic model without Allee effects (Hening et al., 2018). In summary, we have studied a general model for early warning systems of tipping cascades. Although the analytic expressions for leading indicators need to be numerically evaluated for the spatially heterogeneous model, they still play a key role in the identification of critical slowing down in coupled ecological networks.

### 3.8. Acknowledgements

This research was supported by NSF Grant DMS - 1817124 Metacommunity Dynamics: Integrating Local Dynamics, Stochasticity and Connectivity.

CHAPTER 4

# Optimal management of stochastic invasion in a metapopulation with Allee effects

## 4.1. Abstract

Invasive species account for incalculable damages worldwide, in both ecological and bioeconomic terms. The question of how a network of invasive populations can be optimally managed is one that deserves further exploration. A study accounting for partial observability and imperfect detection, in particular, could yield useful insights into species eradication efforts. Here, we generalized a simple model system that we developed in previous work. This model consists of three interacting populations with underlying strong Allee effects and stochastic dynamics, inhabiting distinct locations connected by dispersal, which can generate bistability. To explore the stochastic dynamics, we formulated an individual-based modeling approach. Next, using the theory of continuous-time Markov chains, we approximated the original high-dimensional model by a Markov chain with eight states, with each state corresponding to a combination of population thresholds. We then used the reduced model as the core for a powerful decision-making tool, referred to as a Partially Observable Markov Decision Process (POMDP). Analysis of this POMDP indicates when the system results in optimal management outcomes.

## 4.2. Introduction

Biological invasions of pests pose a serious and growing threat to ecosystems around the world (Liebhold et al., 2016; Tobin, 2018; Venette and Hutchison, 2021). They disrupt the structure of ecosystems, (Bauer, 2012; Dukes and Mooney, 2004), outcompete native species (Huxel, 1999), or pose dangers to human health by transmitting disease, leading to infections or deaths (Hulme, 2014; Larson et al., 2005). Damages from invasive species worldwide have recently been estimated at more than 1.4 trillion USD over a time period of four decades, comprising a large fraction of the

global economy (Diagne et al., 2021). For example, the invasive gypsy moth (*Lymantria dispar*) alone caused nearly 500 million USD in economic losses from the years of 1980 to 1996 (Wallner, 1998).

The synergy between mathematical models and experimental data can accelerate the development of cost-efficient approaches in exploring and recommending management protocols for invasive species. The interplay between several important elements – namely, local invasion dynamics, connectivity, control, and observability – should inform these approaches. In particular, it is crucial to make appropriate management decisions (e.g., by using early-warning signals) when knowledge about the system is limited, as is typically the case early in the outbreak of an invasive species or emerging infectious disease (Mallela and Hastings, 2021b).

The inclusion of stochasticity in modeling frameworks is key in exploring the control of an invasive population, which often initiates through a successful invasion event, after which it establishes and spreads (Lodge et al., 2016). Because the existence of a strong Allee effect implies the existence of a survival threshold (Johnson and Hastings, 2018; Méndez et al., 2019), the presence of a sufficiently strong Allee effect typically enables the extinction of an invasive species (Liebhold et al., 2016). In particular, eradication can be achieved by bringing a population below its Allee threshold, rather than by seeking to eliminate every member. Given that populations in nature rarely exist in isolation, a metapopulation structure would be a reasonable choice for a modeling study of invasive species management.

Another important feature of a modeling study is the issue of optimality in a problem of dynamic optimization. When faced with limited resources, which is nearly always the case, principles of bioeconomics can be helpful in guiding management (Clark, 2010). For instance, the accrual of economic costs related to control, damages, and observation are all relevant factors that can be addressed in an application of bioeconomics (Epanchin-Niell and Hastings, 2010).

In order to explore how a connected network of invasive populations can be effectively managed or eradicated by Allee effects, we conducted a simple analysis involving a metapopulation with a connectivity structure given by a passive, symmetric diffusion process. We extended the model described in our previous work (Mallela and Hastings, 2021a) by including an additional location (or patch) in the model formulation. Then, by using a powerful decision-making framework known

as a Partially Observable Markov Decision Process (POMDP) (Chadès et al., 2017, 2021), we explored the realistic scenario of partial observability with respect to location, for each of the possible network topologies.

The remainder of the paper is organized as follows. In Section 4.3, following a methodology we previously developed (Mallela and Hastings, 2021a), we provide the background needed to formulate a stochastic, individual-based model that accounts for Allee effects. The model dynamics are described by a Markovian birth-death process. This representation works nicely with the theory of stochastic processes, including Markov chains and mean first passage times. In Section 4.4, we employ dimensionality reduction and useful approximations to specify a continuous-time Markov chain with a finite (but small) number of states. This reduced model then serves as a foundation for the POMDP used in this study (described in Section 4.4). In Section 4.5, we describe the results obtained from numeric simulations. Finally, we conclude with discussion in Section 4.6.

## 4.3. Model Formulation

In this work, we formulate our network model by following the approach of our previous work (Mallela and Hastings, 2021a). For the sake of completeness, we include the full derivation here. We consider the case of a network with three identical patches, or locations. There are two distinct topologies for such a network; namely, the patches are connected either in a straight line or in a triangular configuration (Fig. 4.1). Our work uses an individual-based model (IBM) that displays both the weak and strong Allee effects and also accounts for dispersal, consisting of linear and binary birth processes, a ternary competition process, a linear death process, and an exchange process. In what follows, we describe the reaction schemes associated with the line and triangle configurations, respectively.

### 4.3.1. Line configuration.

$$X_1 \xrightarrow{\mu_1} (1+b)X_1 \tag{4.1a}$$

$$2X_1 \xrightarrow{\lambda_1} (2+a)X_1 \tag{4.1b}$$

$$X_1 \xrightarrow{\gamma_1} \emptyset \tag{4.1c}$$

$$3X_1 \xrightarrow{\tau_1} (3-c)X_1 \tag{4.1d}$$

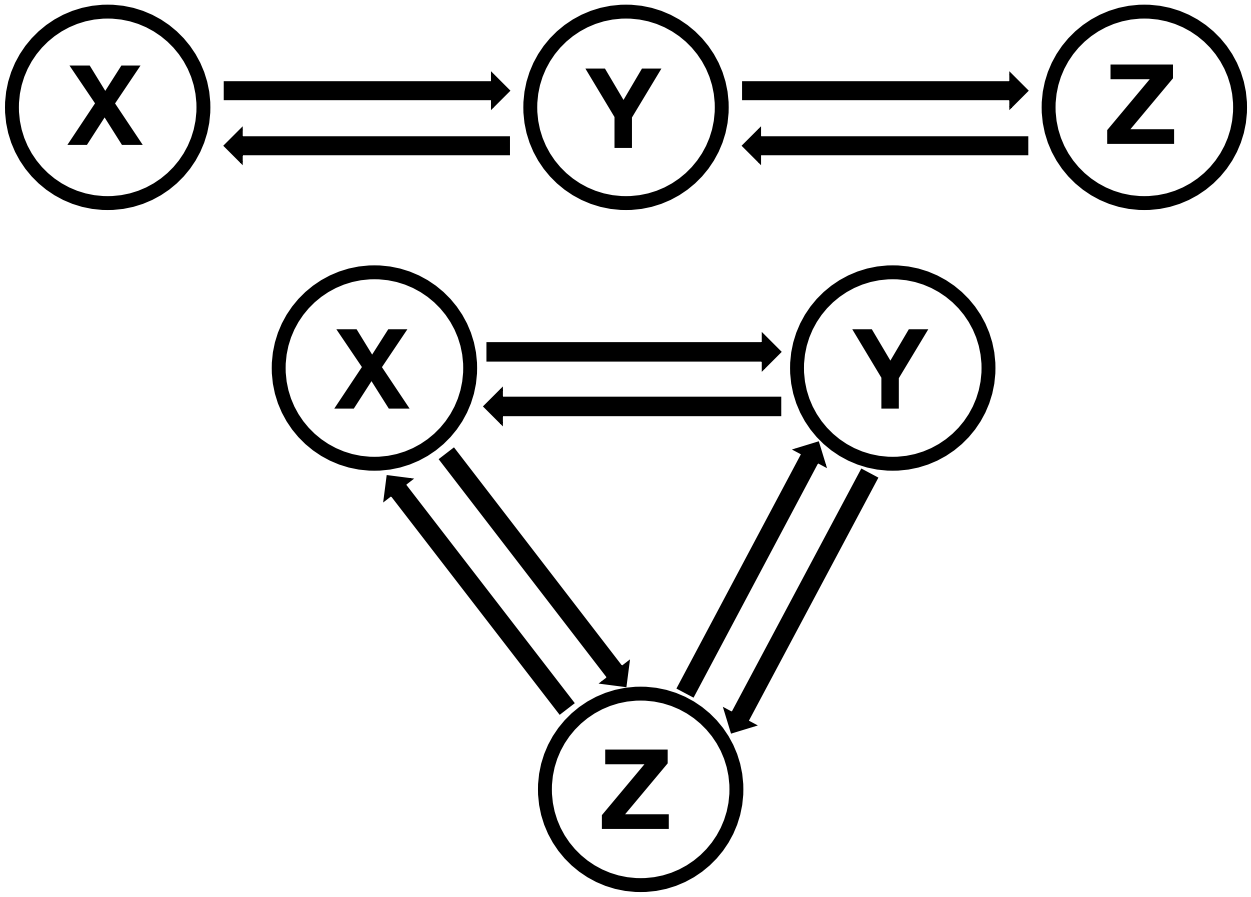


FIGURE 4.1. Line (top) and triangle (bottom) network topologies for a metapopulation consisting of three locations. The symbols $X$, $Y$, and $Z$ denote the identities of the locations. Arrows indicate dispersal between locations via passive, symmetric diffusion.

$$X_2 \xrightarrow{\mu_2} (1+b)X_2 \tag{4.1e}$$

$$2X_2 \xrightarrow{\lambda_2} (2+a)X_2 \tag{4.1f}$$

$$X_2 \xrightarrow{\gamma_2} \emptyset \tag{4.1g}$$

$$3X_2 \xrightarrow{\tau_2} (3-c)X_2 \tag{4.1h}$$

$$X_3 \xrightarrow{\mu_3} (1+b)X_3 \tag{4.1i}$$

$$2X_3 \xrightarrow{\lambda_3} (2+a)X_3 \tag{4.1j}$$

(4.1k) $$X_3 \xrightarrow{\gamma_3} \emptyset$$

(4.1l) $$3X_3 \xrightarrow{\tau_3} (3-c)X_3$$

(4.1m) $$X_1 \xrightarrow{d} X_2$$

(4.1n) $$X_2 \xrightarrow{d} X_1$$

(4.1o) $$X_2 \xrightarrow{d} X_3$$

(4.1p) $$X_3 \xrightarrow{d} X_2$$

Reaction (4.1a) defines a linear birth process, which occurs at a constant rate of $\mu_1$, and describes the baseline reproductive success of the first population in the absence of cooperative effects. It accounts for the fact that the typical individual produces $b$ offspring that reach reproductive age. Reaction (4.1b) is a binary birth process that occurs at a constant rate of $\lambda_1$, and describes cooperative interactions, such as breeding, anti-predator behavior, or foraging, that result in producing $a$ additional offspring which reach reproductive age. Reaction (4.1c) is a linear death process, occurring at a constant rate of $\gamma_1$, which accounts for mortality due to natural causes. The reaction (4.1d) is a ternary competition process, accounting for the results of overcrowding and resource depletion, where $c$ individuals die at rate $\tau_1$. Note that $1, 2$, or $3$ are the only meaningful values for $c$. Reactions (4.1e)-(4.1l) are defined analogously for the second and third populations. Finally, reactions (4.1m)-(4.1p) define the exchange processes of symmetric dispersal between the populations in the distinct patches. Dispersal occurs at a constant rate of $d$.

The reaction scheme (4.1) defines a Markovian process, and the temporal evolution of $P(n_1, n_2, n_3, t)$, the probability of having $n_i$ individuals from the $i^{th}$ population at time $t$ for $i = 1, 2, 3$, is described by the following master equation (Gardiner, 2004):

(4.2) $$\frac{\mathrm{d}P(\boldsymbol{n}, t)}{\mathrm{d}t} = \sum_{\boldsymbol{r}} [W(\boldsymbol{n} - \boldsymbol{r}, \boldsymbol{r})P(\boldsymbol{n} - \boldsymbol{r}, t) - W(\boldsymbol{n}, \boldsymbol{r})P(\boldsymbol{n}, t)],$$

where $P(\boldsymbol{n} < \mathbf{0}, t) = P(n_1 < 0, n_2 < 0, n_3 < 0, t) = 0$. Here $W(\boldsymbol{n}, \boldsymbol{r})$ denotes the set of transition rates between the states with $\boldsymbol{n}$ and $\boldsymbol{n} + \boldsymbol{r}$ individuals, where

$$\begin{aligned}\boldsymbol{r} &= \{\boldsymbol{r_1}, \boldsymbol{r_2}, \ldots, \boldsymbol{r_{16}}\} \\ &= \{(b,0,0), (a,0,0), (-1,0,0), (-c,0,0), (0,b,0), (0,a,0), (0,-1,0), (0,-c,0), \\ &(0,0,b), (0,0,a), (0,0,-1), (0,0,-c), (-1,0,0), (0,-1,0), (0,-1,0), (0,0,-1)\}\end{aligned}$$

is the vector of transition increments corresponding to the system given by (4.1). The transition rates corresponding to each reaction, $W(\boldsymbol{n}, \boldsymbol{r})$, are obtained from the reaction kinetics (Gardiner, 2004; Van Kampen, 1992):

(4.3a) $$W(\boldsymbol{n}, \boldsymbol{r_1}) = \mu_1 n_1$$

(4.3b) $$W(\boldsymbol{n}, \boldsymbol{r_2}) = \frac{\lambda_1}{2} n_1(n_1 - 1)$$

(4.3c) $$W(\boldsymbol{n}, \boldsymbol{r_3}) = \gamma_1 n_1$$

(4.3d) $$W(\boldsymbol{n}, \boldsymbol{r_4}) = \frac{\tau_1}{6} n_1(n_1 - 1)(n_1 - 2)$$

(4.3e) $$W(\boldsymbol{n}, \boldsymbol{r_5}) = \mu_2 n_2$$

(4.3f) $$W(\boldsymbol{n}, \boldsymbol{r_6}) = \frac{\lambda_2}{2} n_2(n_2 - 1)$$

(4.3g) $$W(\boldsymbol{n}, \boldsymbol{r_7}) = \gamma_2 n_2$$

(4.3h) $$W(\boldsymbol{n}, \boldsymbol{r_8}) = \frac{\tau_2}{6} n_2(n_2 - 1)(n_2 - 2)$$

(4.3i) $$W(\boldsymbol{n}, \boldsymbol{r_9}) = \mu_3 n_3$$

(4.3j) $$W(\boldsymbol{n}, \boldsymbol{r_{10}}) = \frac{\lambda_3}{2} n_3(n_3 - 1)$$

(4.3k) $$W(\boldsymbol{n}, \boldsymbol{r_{11}}) = \gamma_3 n_3$$

(4.3l) $$W(\boldsymbol{n}, \boldsymbol{r_{12}}) = \frac{\tau_3}{6} n_3(n_3 - 1)(n_3 - 2)$$

(4.3m) $$W(\boldsymbol{n}, \boldsymbol{r_{13}}) = d n_2$$

(4.3n) $$W(\boldsymbol{n}, \boldsymbol{r_{14}}) = d n_1$$

$$W(\boldsymbol{n}, \boldsymbol{r_{15}}) = dn_3 \tag{4.3o}$$

$$W(\boldsymbol{n}, \boldsymbol{r_{16}}) = dn_2 \tag{4.3p}$$

Deterministic ODEs for the average population sizes can be derived using (4.2). Multiplying (4.2) by $n_1 n_2 n_3$, using transition rates (4.3), and summing over all values of $n_1$, $n_2$, and $n_3$, we obtain

$$\frac{\mathrm{d}\rho_1}{\mathrm{d}t} = (b\mu_1 - \gamma_1 - d)\rho_1 + \frac{a\lambda_1}{2}\rho_1^2 - \frac{c\tau_1}{6}\rho_1^3 + d\rho_2 \tag{4.4a}$$

$$\frac{\mathrm{d}\rho_2}{\mathrm{d}t} = (b\mu_2 - \gamma_2 - 2d)\rho_2 + \frac{a\lambda_2}{2}\rho_2^2 - \frac{c\tau_2}{6}\rho_2^3 + d(\rho_1 + \rho_3) \tag{4.4b}$$

$$\frac{\mathrm{d}\rho_3}{\mathrm{d}t} = (b\mu_3 - \gamma_3 - d)\rho_3 + \frac{a\lambda_3}{2}\rho_3^2 - \frac{c\tau_3}{6}\rho_3^3 + d\rho_2 \tag{4.4c}$$

where $\rho_i = \langle n_i \rangle$ is the mean number of individuals in population $i$ for $i = 1, 2, 3$. We note that (4.4) holds strictly when the demographic fluctuations vanish. This occurs in the macroscopic limit as the population size and spatial extent of each population increase to infinity such that their ratio, the population density, stays constant or approaches a finite limit.

For the sake of simplicity, in what follows, we focus on the simplest version of this IBM. Namely, we treat the Markovian process as a single-step process with $a = b = c = 1$. The set of reactions (4.1) then becomes

$$X_1 \xrightarrow{\mu_1} 2X_1 \tag{4.5a}$$

$$2X_1 \xrightarrow{\lambda_1} 3X_1 \tag{4.5b}$$

$$X_1 \xrightarrow{\gamma_1} \emptyset \tag{4.5c}$$

$$3X_1 \xrightarrow{\tau_1} 2X_1 \tag{4.5d}$$

$$X_2 \xrightarrow{\mu_2} 2X_2 \tag{4.5e}$$

$$2X_2 \xrightarrow{\lambda_2} 3X_2 \tag{4.5f}$$

$$X_2 \xrightarrow{\gamma_2} \emptyset \tag{4.5g}$$

$$3X_2 \xrightarrow{\tau_2} 2X_2 \tag{4.5h}$$

(4.5i) $$X_3 \xrightarrow{\mu_3} 2X_3$$

(4.5j) $$2X_3 \xrightarrow{\lambda_3} 3X_3$$

(4.5k) $$X_3 \xrightarrow{\gamma_3} \emptyset$$

(4.5l) $$3X_3 \xrightarrow{\tau_3} 2X_3$$

(4.5m) $$X_1 \xrightarrow{d} X_2$$

(4.5n) $$X_2 \xrightarrow{d} X_1$$

(4.5o) $$X_2 \xrightarrow{d} X_3$$

(4.5p) $$X_3 \xrightarrow{d} X_2$$

The mean-field rate equations corresponding to (4.5) are

(4.6a) $$\frac{\mathrm{d}\rho_1}{\mathrm{d}t} = (\mu_1 - \gamma_1 - d)\rho_1 + \frac{\lambda_1}{2}\rho_1^2 - \frac{\tau_1}{6}\rho_1^3 + d\rho_2$$

(4.6b) $$\frac{\mathrm{d}\rho_2}{\mathrm{d}t} = (\mu_2 - \gamma_2 - 2d)\rho_2 + \frac{\lambda_2}{2}\rho_2^2 - \frac{\tau_2}{6}\rho_2^3 + d(\rho_1 + \rho_3)$$

(4.6c) $$\frac{\mathrm{d}\rho_3}{\mathrm{d}t} = (\mu_3 - \gamma_3 - d)\rho_3 + \frac{\lambda_3}{2}\rho_3^2 - \frac{\tau_3}{6}\rho_3^3 + d\rho_2$$

Next, we can define dimensionless quantities in terms of the reaction rates as follows:

(4.7) $$\widetilde{N}_1 = \frac{3\lambda_1}{2\tau_1}, \quad \delta_1^2 = 1 + \frac{8\tau_1(\mu_1 - \gamma_1 - d)}{3\lambda_1^2}, \quad R_0^{(1)} = \frac{\mu_1}{\gamma_1 + d}$$

(4.8) $$\widetilde{N}_2 = \frac{3\lambda_2}{2\tau_2}, \quad \delta_2^2 = 1 + \frac{8\tau_2(\mu_2 - \gamma_2 - 2d)}{3\lambda_2^2}, \quad R_0^{(2)} = \frac{\mu_2}{\gamma_2 + 2d}$$

(4.9) $$\widetilde{N}_3 = \frac{3\lambda_3}{2\tau_3}, \quad \delta_3^2 = 1 + \frac{8\tau_3(\mu_3 - \gamma_3 - d)}{3\lambda_3^2}, \quad R_0^{(3)} = \frac{\mu_3}{\gamma_3 + d}$$

Note that for $i = 1$ to 3, $\widetilde{N}_i$ defines the scale of the typical size of population $i$ prior to extinction. The identities (4.7)-(4.9) establish a relation between the microscopic $(\lambda_i, \mu_i, \gamma_i, \tau_i)$ and macroscopic $(\widetilde{N}_i, \delta_i, R_0^{(i)})$ parameters, which are obtainable through field observations.

Observe that the individual-based model displays the strong Allee effect, if $R_0^{(i)} < 1$. Furthermore, for $R_0^{(i)} < 1$ we have $\delta_i < 1$. For the strong Allee effect, we must also demand that $\delta_i > 0$.

As in our previous work (Mallela and Hastings, 2021a), we treat the stochastic rate parameters in (4.5) as identical for all populations. This assumption appears to be reasonable in many cases because of the presence of dispersal between populations in close proximity. Given that the three patches are identical, the matching scheme can be written as follows (for $i = 1, 2, 3$):

$$\mu := \mu_i = \beta \tag{4.10a}$$

$$\lambda := \lambda_i \equiv 4 \tag{4.10b}$$

$$\gamma := \gamma_i \equiv 1 \tag{4.10c}$$

$$\tau := \tau_i \equiv 6 \tag{4.10d}$$

$$\widetilde{N} := \widetilde{N}_i \tag{4.10e}$$

Thus for $i = 1$ and 3,

$$\widetilde{N} = 1, \quad \delta_i^2 = \beta - d, \quad R_0^{(i)} = \frac{\beta}{d+1} \tag{4.11}$$

and for $i = 2$,

$$\widetilde{N} = 1, \quad \delta_i^2 = \beta - 2d, \quad R_0^{(i)} = \frac{\beta}{2d+1} \tag{4.12}$$

In what follows, we are interested in the case of bistability in each patch, which is manifest in the case of the strong Allee effect. This means that $0 < \delta_i < 1$.

**4.3.2. Triangle configuration.** The model corresponding to the triangle configuration is formulated in a similar manner as in Section 4.3.1. However, there is one key modification to the reaction scheme, namely, the addition of the following reactions to (4.5):

$$X_1 \xrightarrow{d} X_3 \tag{4.13a}$$

$$X_3 \xrightarrow{d} X_1 \tag{4.13b}$$

The mean-field rate equations are then:

$$\frac{\mathrm{d}\rho_1}{\mathrm{d}t} = (\mu_1 - \gamma_1 - 2d)\rho_1 + \frac{\lambda_1}{2}\rho_1^2 - \frac{\tau_1}{6}\rho_1^3 + d(\rho_2 + \rho_3) \tag{4.14a}$$

$$\frac{\mathrm{d}\rho_2}{\mathrm{d}t} = (\mu_2 - \gamma_2 - 2d)\rho_2 + \frac{\lambda_2}{2}\rho_2^2 - \frac{\tau_2}{6}\rho_2^3 + d(\rho_1 + \rho_3) \tag{4.14b}$$

$$\frac{\mathrm{d}\rho_3}{\mathrm{d}t} = (\mu_3 - \gamma_3 - 2d)\rho_3 + \frac{\lambda_3}{2}\rho_3^2 - \frac{\tau_3}{6}\rho_3^3 + d(\rho_1 + \rho_2) \tag{4.14c}$$

We then obtain (for $i = 1, 2, 3$):

$$\widetilde{N} = 1, \quad \delta_i^2 = \beta - 2d, \quad R_0^{(i)} = \frac{\beta}{2d+1} \tag{4.15}$$

As in the case of the line configuration, $0 < \delta_i < 1$.

### 4.4. Methods

Our stochastic model operates over a three-dimensional state space. As in our previous work (Mallela and Hastings, 2021a), we adopted a master equation treatment of our model. Instead of specifying a model with carrying capacities, we used an individual-based modeling approach using a reaction network. This allows for a fine-grained representation of the underlying discrete, stochastic process. Using this approach, we then wrote down the three-dimensional master equation for the process. Given that this stochastic process is a continuous-time Markov chain (CTMC), it can be explicitly described by a generator $\mathcal{Q}$-matrix with a countable state space. A nice feature of most ecological models is that they are built around processes that will approach a compact region exponentially quickly. Any reasonable ecological model should not have unbounded population growth. Density dependence in ecological models typically ensures this. Thus, our model effectively operates over a finite state space as the probability of arbitrarily large populations is negligibly small. Using this insight, we were able to obtain a finite CTMC in three dimensions.

Since the multidimensional master equation was relatively unwieldy to work with, we reduced the three-dimensional state space to one dimension (Allen, 2010; Allen and Allen, 2003). Denoting $N := N_1 = N_2 = N_3$ as the maximum number of individuals in a given population, the specific mapping function used was $f(x, y, z) = (N + 1)^2 x + (N + 1)y + z + 1$, for $x, y, z \in [0, N]$. We also used the sparsity of the banded $\mathcal{Q}$-matrix to reduce computational cost.

For the ensuing analyses, we specified population thresholds by treating them as identical across patches. Denoting $L := L_1 = L_2 = L_3$ and $H := H_1 = H_2 = H_3$ as the low and high thresholds, we

specified $A := A_1 = A_2 = A_3$ as the Allee threshold, noting that $0 < L < A < H \leq N$. Here $N$ can be understood as a system size parameter. The linear ordering of the thresholds guarantees that $L$ is always less than $H$. Note that the smallest $L$ threshold, $L = 1$, behaves as a state corresponding to quasi-extinction. Moreover, with $2 \leq A \leq N - 1$, we have $A + 1 \leq H \leq N$ and $1 \leq L \leq A - 1$. It can be shown that this results in $\binom{N}{3}$ combinations of the thresholds.

In order to probe the system under consideration, we numerically computed the mean first-passage times (MFPTs) for models (4.5) and (4.13) with the state space parameterized by $N$ for all combinations of the parameters $\beta_i, d, L, A$, and $H$. First, we formed the $\mathcal{Q}$-matrix for each point in parameter space. We then formed a vector of initial state probabilities $p_0$ governing the subsequent evolution of the CTMC. Then, the rows and columns of $\mathcal{Q}$ corresponding to the trap states (e.g., extinction) were removed. Similarly, the corresponding entry in $p_0$ was removed. Next, using the truncated $\mathcal{Q}$-matrix, $\widetilde{\mathcal{Q}}$, we computed the matrix of mean residence times, or $-\widetilde{\mathcal{Q}}^{-1}$. Finally, we computed the sum of the entries in $-\widetilde{\mathcal{Q}}^{-1}p_0$ to yield the MFPT from the desired initial state to the desired end state.

We could then construct a compartmental system with a reduced state space consisting of eight states: $HHH, HHL, HLL, LLL, LLH, LHH, LHL$, and $HLH$. Each of these states corresponds to a combination of population thresholds. For instance, $HLL$ means that the first population is at a high abundance, while the second and third populations are at low levels. The MFPTs from the original model were used as input rates in the matrix of transition rates for the reduced model. Thus we used an emulator as a proxy to analyze the original system.

We can use the emulator (described above) to construct the schematic diagram shown in Fig. 4.2. In the diagram, each $r_i$ for $i = 1, 2, \ldots, 24$ represents the transition rate between the relevant compartments. Each rate can be obtained as the inverse of the corresponding MFPT. Given that the process is represented as a CTMC, we can write down the transition probability matrix $\mathcal{T}$ for the emulator. The transition probability matrix of the embedded discrete-time Markov chain gives the one-step transition probabilities of the system.

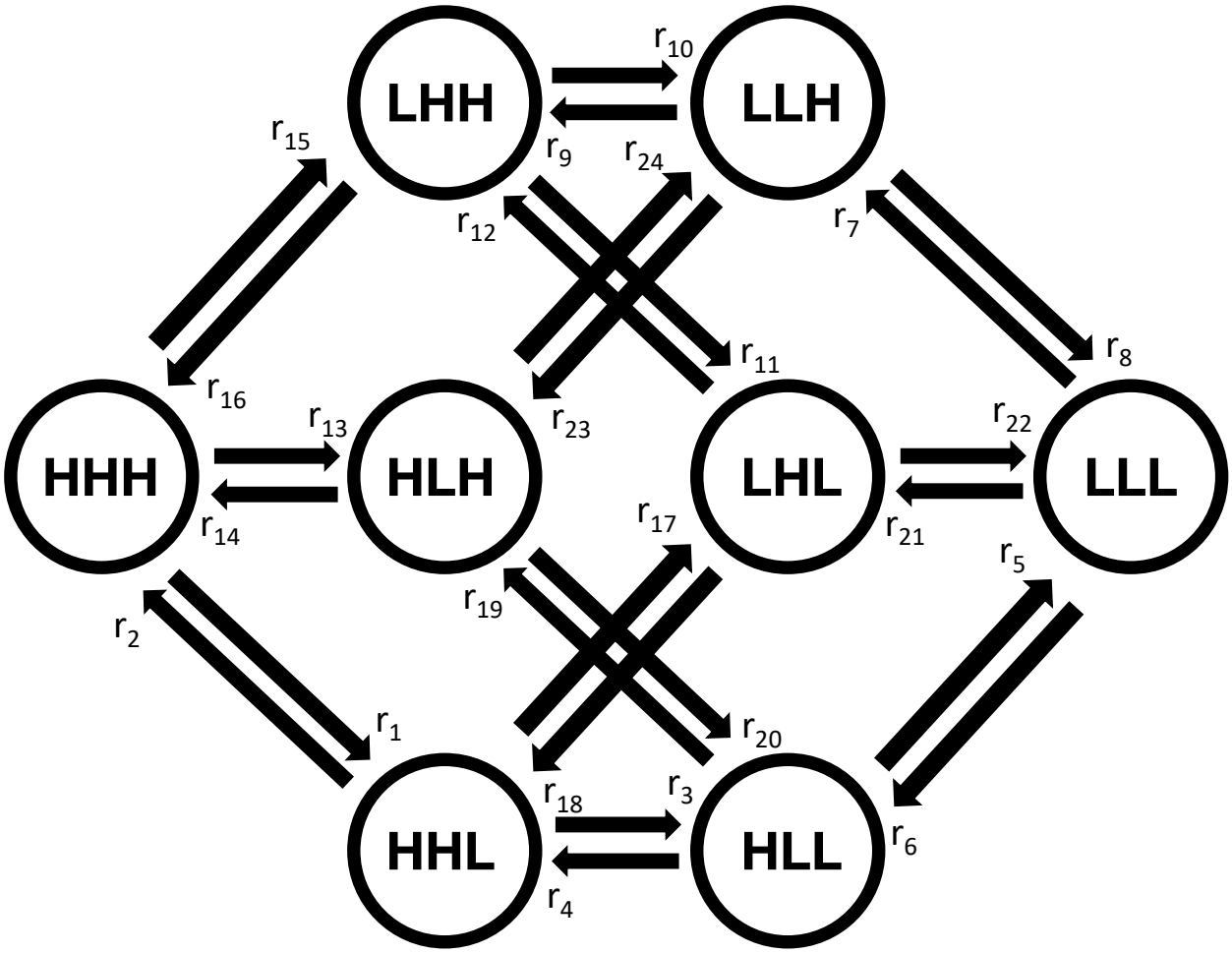


FIGURE 4.2. Schematic diagram of state-dependent transitions for a given metapopulation. In the diagram, each $r_i$ for $i = 1, 2, \ldots, 24$ denotes the transition rate between the relevant compartments, which are indicated in solid circles.For instance, $HLH$ means that the first and third locations are in a state of high abundance of the invasive species, and the second location is in a state of low abundance. The diagram has $2^n$ states, where $n$ indicates the number of locations, and 24 transitions between states.

The matrix $\mathcal{T}$ is given as:

$$\begin{pmatrix}
0 & \frac{r_1}{r_1+r_{13}+r_{15}} & 0 & 0 & 0 & \frac{r_{15}}{r_1+r_{13}+r_{15}} & 0 & \frac{r_{13}}{r_1+r_{13}+r_{15}} \\
\frac{r_2}{r_2+r_3+r_{17}} & 0 & \frac{r_3}{r_2+r_3+r_{17}} & 0 & 0 & 0 & \frac{r_{17}}{r_2+r_3+r_{17}} & 0 \\
0 & \frac{r_4}{r_4+r_5+r_{19}} & 0 & \frac{r_5}{r_4+r_5+r_{19}} & 0 & 0 & 0 & \frac{r_{19}}{r_4+r_5+r_{19}} \\
0 & 0 & \frac{r_6}{r_6+r_7+r_{21}} & 0 & \frac{r_7}{r_6+r_7+r_{21}} & 0 & \frac{r_{21}}{r_6+r_7+r_{21}} & 0 \\
0 & 0 & 0 & \frac{r_8}{r_8+r_9+r_{23}} & 0 & \frac{r_9}{r_8+r_9+r_{23}} & 0 & \frac{r_{23}}{r_8+r_9+r_{23}} \\
\frac{r_{16}}{r_{10}+r_{11}+r_{16}} & 0 & 0 & 0 & \frac{r_{10}}{r_{10}+r_{11}+r_{16}} & 0 & \frac{r_{11}}{r_{10}+r_{11}+r_{16}} & 0 \\
0 & \frac{r_{18}}{r_{12}+r_{18}+r_{22}} & 0 & \frac{r_{22}}{r_{12}+r_{18}+r_{22}} & 0 & \frac{r_{12}}{r_{12}+r_{18}+r_{22}} & 0 & 0 \\
\frac{r_{14}}{r_{14}+r_{20}+r_{24}} & 0 & \frac{r_{20}}{r_{14}+r_{20}+r_{24}} & 0 & \frac{r_{24}}{r_{14}+r_{20}+r_{24}} & 0 & 0 & 0
\end{pmatrix}$$

where the ordering of the states is

$$(HHH, HHL, HLL, LLL, LLH, LHH, LHL, HLH).$$

Note that $\mathcal{T}$ is row-stochastic.

**4.4.1. Partial observability.** The problem we focus on is one of species eradication: at each time step, managers allocate their budget to minimize the population size of an invasive species. Managers need informed guidance in order to allocate resources and decide when to manage or stop managing. We present a formulation of this problem as a POMDP. A Markov decision process (MDP) is a stochastic control process in discrete-time that satisfies the Markov property. (Bellman, 1957). Partially observable MDPs (POMDPs) generalize MDPs, where a manager is only partly aware of the current state of the system (Åström, 1965). POMDPs are described by a tuple $\langle S, A, Z, P, O, r, H, b_0, \gamma \rangle$, where:

- $S = \{HHH, HHL, HLL, LLL, LLH, LHH, LHL, HLH\}$ is the set of states. Each state represents the status of the metapopulation at a given time step. Managers do not perfectly detect the state of the system. The current state is denoted as $s_t$.
- $A = \{$manage the first location, manage the second location, manage the third location, do nothing$\}$ is the set of actions. An action corresponds to the decision that managers may implement at any given time step. We assume that a fixed budget allows for the management of only one location at each time step. The realized action is denoted as $a_t$.
- $Z = \{$Absent (L), Present (H)$\}$ is the set of observations for an individual location. An observation ($z_t$) indicates the information received by managers at each time step.
- $P(s_{t+1}|s_t, a_t)$ are the transition probabilities between states, conditional on an action, that represent the dynamics of the system; for instance, the probability of eradication of the metapopulation of invasive species at a given time step, assuming that managers do nothing, is given by the transition probability matrix $\mathcal{T}$ for the emulator described above.
- $O(z_{t+1}|s_{t+1}, a_t)$ denote the detection probabilities given an action $a_t \in A$ undertaken at time step $t$, and the system state $s_{t+1} \in S$ at time $t + 1$.

- $r(s_t, a_t)$ is a reward function that accounts for the economic benefits and costs of being in a state $s_t \in S$ and performing an action $a_t \in A$. In our case, we assume that rewards are obtained only for the actual state of the system (i.e., not for the observed state). We specify no reward when nothing is done, no reward when an individual location is in a high (H) state, a reward of 25 units when an individual location is in a low (L) state, and a cost of $25k$ units when a location is managed. Here, $k = 2$.
- $H$ is the time horizon (i.e., finite or infinite) over which actions are implemented. Here, we use an infinite time horizon. From an ecological standpoint, we are assuming that the decision-making process of a program should be independent of its time horizon, and should depend only on its state. In this case, an optimal policy is independent of time.
- $b_0$ denotes the initial belief, a probability distribution over states. A belief state represents our belief of the system state at a given time step. In our case, $b_0 = (1, 0, 0, 0, 0, 0, 0, 0)$, corresponding to an initial belief that the metapopulation is invaded at all locations.
- $\gamma \in [0, 1]$ is a discount factor, relating future rewards and costs to their total present value. A discount factor less than 1 indicates that immediate rewards are more valuable than later ones (Koopmans, 1960). It also ensures the convergence of the optimization procedure and helps solvers converge more rapidly towards a solution (Kaelbling et al., 1998; Kurniawati et al., 2008; Spaan and Vlassis, 2005). We define the optimization criterion as the expected sum of discounted rewards over an infinite time horizon, $\mathbb{E}(\sum_{t=0}^{\infty} \gamma^t r_t)$. In this study, we take $\gamma = 0.95$.

Solving a POMDP corresponds to finding an optimal policy $\pi : B \to A$ that maps the current belief state $b \in B$ to an allocation of resources. Belief states are used as sufficient statistics as a proxy for the true state of the system (Åström, 1965). The optimal policy maximizes an optimization criterion (as described above). The criterion is also referred to as the value function $V_\pi(b_t)$ for a given belief state $b_t$ and a given policy $\pi$. In this study, we used the MATLAB toolbox MDPSolve (Fackler, 2011) for solving POMDPs with the value iteration algorithm. POMDPs are solved by discretizing the belief state space and interpolating over rectangular or simplex grids (Zhou and Hansen, 2001). Then, the discretized problem is solved as an MDP. Our model outcome was chosen

as the value function evaluated at a belief state corresponding to guaranteed eradication across the locations, or $V_\pi(b_t)$, with $b_t = (0, 0, 0, 1, 0, 0, 0, 0)$.

As in our previous work (Mallela and Hastings, 2021a), we specified an upper bound of 1 for the dispersal parameter $d$. Then, we chose a size of $N = 6$ for each location. This was the largest value for $N$ such that the largest condition number among the space of all matrices $\widetilde{\mathcal{Q}}$, taken over the set of simulated parameter values, was less than $10^7$. All computations were performed in MATLAB (MATLAB, 2021).

### 4.5. Results

One case of interest, corresponding to partial observability of a given location, relates to the dependence of the model outcome on potentially imperfect detection. A second case of interest relates to how the model outcome depends on how many locations are observed, as well as on which locations are observed, in a given network topology. We first explore the case of imperfect detection. In particular, we focused on the case of $L = 1, A = 3$, and $H = N = 6$ for subsequent analyses. (In our initial explorations, we found qualitatively similar behavior for other sets of parameter values obeying the constraints discussed in Section 4.4.)

In Fig. 4.3, we show results corresponding to the case of total observability (i.e., all three patches are observable). Note that each curve in every figure panel is symmetric about $o = 0.5$. This is because of the symmetry of the system (i.e., the model is symmetric with respect to the high ($H$) and low ($L$) thresholds, meaning that $H$ and $L$ can be interchanged without ambiguity. We see that for $o > 0.5$, the reward value is monotonically increasing with respect to detection accuracy, meaning that rewards are maximized at perfect detection (i.e., when $o = 1$). Here, the metapopulation obeying a triangular configuration always results in the same reward value as one obeying a line structure.

Next, we explore the second case of interest, which relates to dependence of the model outcome on both the number and type of location observed in a given network. In Fig. 4.4, we show results corresponding to the case of perfect observability (i.e., detection of the invasive species is error-free). For each network configuration,adding a location (i.e., two patches as compared to one patch) yields a higher reward. This can be seen by comparing Fig. 4.4A with Fig. 4.4B, Fig. 4.4C

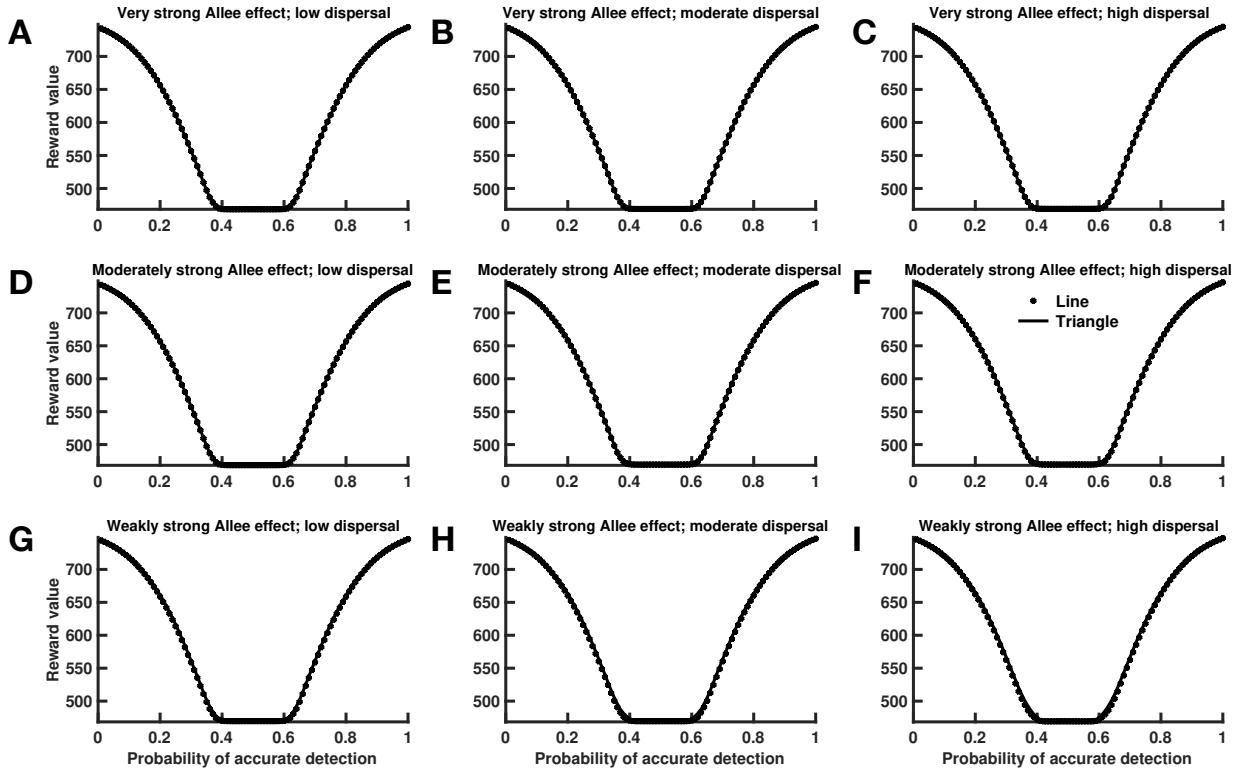


FIGURE 4.3. Dependence of POMDP reward on detection accuracy for the case of total observability. The dispersal parameter $d$ was chosen to take values of $0.01, 0.50$, and $0.99$ corresponding to low, moderate, and high dispersal, respectively. Panels A, B and C correspond to the case of a very strong Allee effect (i.e., $\beta_1 = \beta_3 = d + 0.01$ and $\beta_2 = 2d + 0.01$ in the line network; $\beta_1 = \beta_2 = \beta_3 = 2d + 0.01$ in the triangle network). Panels D, E and F correspond to the case of a moderately strong Allee effect (i.e., $\beta_1 = \beta_3 = d + 0.5$ and $\beta_2 = 2d + 0.5$ in the line network; $\beta_1 = \beta_2 = \beta_3 = 2d + 0.5$ in the triangle network). Finally, Panels G, H and I correspond to the case of a weakly strong Allee effect (i.e., $\beta_1 = \beta_3 = d + 0.99$ and $\beta_2 = 2d + 0.99$ in the line network; $\beta_1 = \beta_2 = \beta_3 = 2d + 0.99$ in the triangle network). See Section 4.3 for more information.

with Fig. 4.4D, and Fig. 4.4E with Fig. 4.4F. Moreover, the line network with only one patch at the end being observable, produces a higher reward value than both the line network with the middle patch being observable and the triangle network. Model outcomes are very similar in the cases of the line network with a patch in the middle and the triangle network. When two patches are observable, all 3 network configurations (i.e., 2 for the line network and 1 for the triangle) result in comparable model outcomes.

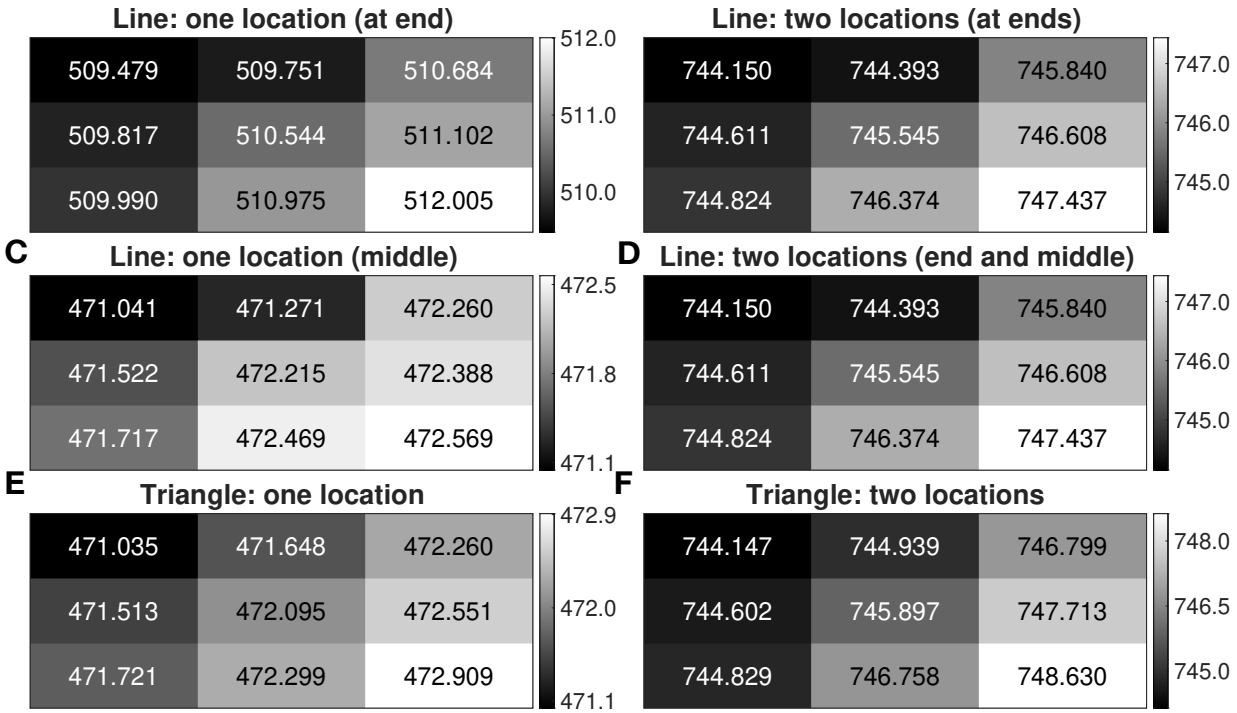


FIGURE 4.4. Dependence of POMDP reward on parameters for the case of perfect observability, with less than three observable locations. Within each panel, the matrix of values can be interpreted as follows. The horizontal axis indicates levels of the dispersal parameter $d$, which was chosen to take values of $0.01, 0.50$, and $0.99$ corresponding to low, moderate, and high dispersal, respectively. The vertical axis indicates levels of the parameter $\beta$, which were chosen as described in the caption for Fig. 4.3. Briefly, the value of $\beta$ increases from top to bottom, with lower values corresponding to a higher strength of the Allee effect; equivalently, to a lower quality of the environment in a given patch. Reward values from the POMDP are indicated in each panel. Panels A, C, and E correspond to the case of one observable patch; panels B, D, and F correspond to the case of two observable patches.

Across all cases, a higher degree of connectivity (given by the dispersal parameter $d$) yields a higher reward value. This feature can be seen by traversing each matrix of values, in a given panel, from left to right. Conversely, a lower strength of the Allee effect (equivalently, a higher quality of the environment in a patch, given by the parameter $\beta$) gives a higher value for the reward. One reaches this conclusion by traversing each matrix of values in a given panel from top to bottom.

Fig. 4.5 is an analogue of Fig. 4.4, but for the case of total observability, where all three patches are observable. Thus, Fig. 4.5 corresponds to the scenario of a Markov Decision Process (MDP). Interestingly, the results here are identical to those of the case where only two patches are

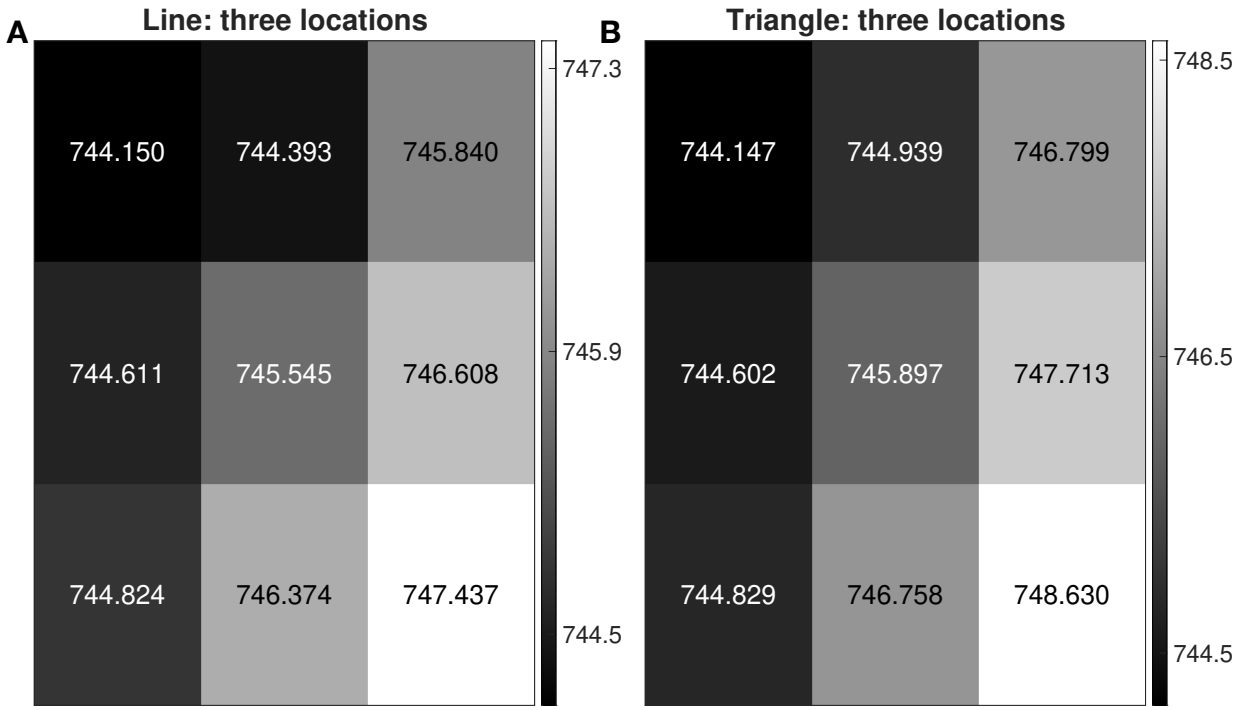


FIGURE 4.5. Dependence of POMDP reward on parameters for the case of perfect observability, when all three locations are observable. Within each panel, the matrix of values can be interpreted as follows. The horizontal axis indicates levels of the dispersal parameter $d$, which was chosen to take values of $0.01, 0.50$, and $0.99$ corresponding to low, moderate, and high dispersal, respectively. The vertical axis indicates levels of the parameter $\beta$, which were chosen as described in the caption for Fig. 4.3. Briefly, the value of $\beta$ increases from top to bottom, with lower values corresponding to a higher strength of the Allee effect; equivalently, to a lower quality of the environment in a given patch. Reward values from the POMDP are indicated in each panel. Panels A and B correspond to the line and triangle networks, respectively.

observable (i.e., compare Fig. 4.5A with Figs. 4.4B and 4D, and Fig. 4.5B with Fig. 4.4F). In other words, it is necessary to observe only two patches, as including a third patch (resulting in an MDP) does not add value to the management program. However, including only one patch results in suboptimal outcomes.

## 4.6. Summary and Discussion

Careful management of an ecological system is an inherently challenging task. An overriding issue is the problem that determining the full state of the system can be costly (Epanchin-Niell et al., 2012; Regan et al., 2011). This may necessitate using approaches that explicitly account

for this difficulty. Although decision-making tools including Markov Decision Processes (MDPs) have indeed been demonstrated to be useful in a variety of applications (Boucherie and Van Dijk, 2017; White, 1993), managers of ecological systems should consider the benefits of using a Partially Observable Markov Decision Process (POMDP) instead of a MDP.

By using a POMDP, one can address the role of possibly costly observation. In a simple system with three different locations, we can ask the question of which locations need to be observed. In this work, we have shown that it is necessary to observe only two locations, as opposed to all three, in order to obtain reasonable management outcomes. We have also demonstrated that a POMDP can be specified in multiple ways, e.g., by modulating the accuracy of detection, controlling for the number of observable locations, or doing both.

Connectivity is clearly a fundamental aspect of our analysis, which corresponds to the degree of isolation in different locations. The spatial organization of a metapopulation also plays a key role in determining system dynamics. Allowing for dispersal among all three patches (i.e., in the triangle configuration) results in a global connectivity structure between the patches. However, the line configuration results in more localized connectivity by placing the locations at the ends at a disadvantage, because the ends do not communicate directly; they are linked only through the central location. This could explain why the line network has differential outcomes, given that only one patch is observable.

For an individual patch, the interplay between dispersal and the quality of the environment determines the model dynamics. In other words, the outcome of the POMDP is highly dependent on the model parameters $d$ and $\beta$, or the strength of the Allee effect in the regime of bistability. When the strong Allee effect is especially pronounced, eradication of the invasive species is considerably easier, yielding a lower reward value from the POMDP. If the strong Allee effect is relatively mild, however, eradication becomes more difficult, hence producing a larger POMDP reward. Dispersal acts as a mediating agent for the Allee dynamics, whereby a higher degree of exchange between patches results in a higher reward value for the POMDP.

The reader must be cautioned that our modeling study has some simplifying assumptions. In order to manage the curse of dimensionality in parameter space, we assumed that all patches are identical. This implies that the individual rate parameters in the reaction schemes are also

identical across patches. Also, the transition rates used to parameterize the stochastic emulator were obtained in terms of mean first-passage times, but an equally valid choice could be the use of most likely first-passage times (i.e., the mode of the distribution of first-passage times). Nevertheless, our theoretical model is valuable as a simulation study, and can be generalized to a larger number of patches. This could introduce more interesting dynamics and would also imply a larger number of possible network topologies. We leave these explorations to future work.

# Bibliography


Ralph Abraham. Cuspoidal nets. In *Business Cycles*, pages 56–63. Springer, 1991.

Edward J Allen, Linda JS Allen, Armando Arciniega, and Priscilla E Greenwood. Construction of equivalent stochastic differential equation models. *Stochastic analysis and applications*, 26(2): 274–297, 2008.

Linda JS Allen. *An introduction to stochastic processes with applications to biology*. CRC press, 2010.

Linda JS Allen and Edward J Allen. A comparison of three different stochastic population models with regard to persistence time. *Theoretical Population Biology*, 64(4):439–449, 2003.

Priyanga Amarasekare. Interactions between local dynamics and dispersal: insights from single species models. *Theoretical Population Biology*, 53(1):44–59, 1998.

Karl Johan Åström. Optimal control of Markov processes with incomplete state information. *Journal of Mathematical Analysis and Applications*, 10:174–205, 1965.

Stefano Battiston, J Doyne Farmer, Andreas Flache, Diego Garlaschelli, Andrew G Haldane, Hans Heesterbeek, Cars Hommes, Carlo Jaeger, Robert May, and Marten Scheffer. Complexity theory and financial regulation. *Science*, 351(6275):818–819, 2016.

Jonathan T Bauer. Invasive species:"back-seat drivers" of ecosystem change? *Biological invasions*, 14(7):1295–1304, 2012.

Richard Bellman. A Markovian decision process. *Journal of mathematics and mechanics*, 6(5): 679–684, 1957.

Nils Berglund and Barbara Gentz. *Noise-induced phenomena in slow-fast dynamical systems: a sample-paths approach*. Springer Science & Business Media, 2006.

Reinette Biggs, Stephen R Carpenter, and William A Brock. Turning back from the brink: detecting an impending regime shift in time to avert it. *Proceedings of the National Academy of Sciences*, 106(3):826–831, 2009.

Maarten C Boerlijst, Thomas Oudman, and André M de Roos. Catastrophic collapse can occur without early warning: examples of silent catastrophes in structured ecological models. *PLoS ONE*, 8(4):e62033, 2013.

Carl Boettiger, Noam Ross, and Alan Hastings. Early warning signals: the charted and uncharted territories. *Theoretical ecology*, 6(3):255–264, 2013.

Richard J Boucherie and Nico M Van Dijk. *Markov decision processes in practice*. Springer, 2017.

David S Boukal and Luděk Berec. Single-species models of the Allee effect: extinction boundaries, sex ratios and mate encounters. *Journal of Theoretical Biology*, 218(3):375–394, 2002.

Chris A Boulton and Timothy M Lenton. Slowing down of North Pacific climate variability and its implications for abrupt ecosystem change. *Proceedings of the National Academy of Sciences*, 112(37):11496–11501, 2015.

Justin S Brashares, Jeffery R Werner, and ARE Sinclair. Social 'meltdown' in the demise of an island endemic: Allee effects and the vancouver island marmot. *Journal of Animal Ecology*, 79 (5):965–973, 2010.

Sarah J Burthe, Peter A Henrys, Eleanor B Mackay, Bryan M Spears, Ronald Campbell, Laurence Carvalho, Bernard Dudley, Iain DM Gunn, David G Johns, Stephen C Maberly, et al. Do early warning indicators consistently predict nonlinear change in long-term ecological data? *Journal of Applied Ecology*, 53(3):666–676, 2016.

SR Carpenter and WA Brock. Early warnings of regime shifts in spatial dynamics using the discrete Fourier transform. *Ecosphere*, 1(5):1–15, 2010.

Stephen R Carpenter, Jonathan J Cole, Michael L Pace, Ryan Batt, WA Brock, Timothy Cline, Jim Coloso, James R Hodgson, Jim F Kitchell, David A Seekell, et al. Early warnings of regime shifts: a whole-ecosystem experiment. *Science*, 332(6033):1079–1082, 2011.

Iadine Chadès, Sam Nicol, Tracy M Rout, Martin Péron, Yann Dujardin, Jean-Baptiste Pichancourt, Alan Hastings, and Cindy E Hauser. Optimization methods to solve adaptive management problems. *Theoretical Ecology*, 10(1):1–20, 2017.

Iadine Chadès, Luz V Pascal, Sam Nicol, Cameron S Fletcher, and Jonathan Ferrer-Mestres. A primer on partially observable Markov decision processes (POMDPs). *Methods in Ecology and Evolution*, 12(11):2058–2072, 2021.

Tom Chou and Maria R D'Orsogna. First passage problems in biology. In *First-passage phenomena and their applications*, pages 306–345. World Scientific, 2014.

AA Cimatoribus, SS Drijfhout, V Livina, and G Van Der Schrier. Dansgaard–oeschger events: bifurcation points in the climate system. *Climate of the Past*, 9(1):323–333, 2013.

Colin W Clark. *Mathematical bioeconomics: the mathematics of conservation*, volume 91. John Wiley & Sons, 2010.

Christopher F Clements and Arpat Ozgul. Indicators of transitions in biological systems. *Ecology letters*, 21(6):905–919, 2018.

Tim Coulson, Pejman Rohani, and Mercedes Pascual. Skeletons, noise and population growth: the end of an old debate? *Trends in Ecology & Evolution*, 19(7):359–364, 2004.

Franck Courchamp, Tim Clutton-Brock, and Bryan Grenfell. Inverse density dependence and the Allee effect. *Trends in ecology & evolution*, 14(10):405–410, 1999.

Franck Courchamp, Elena Angulo, Philippe Rivalan, Richard J Hall, Laetitia Signoret, Leigh Bull, and Yves Meinard. Rarity value and species extinction: the anthropogenic Allee effect. *PLoS biology*, 4(12):e415, 2006.

Franck Courchamp, Ludek Berec, and Joanna Gascoigne. *Allee effects in ecology and conservation*. Oxford University Press, 2008.

Lei Dai, Daan Vorselen, Kirill S Korolev, and Jeff Gore. Generic indicators for loss of resilience before a tipping point leading to population collapse. *Science*, 336(6085):1175–1177, 2012.

Vasilis Dakos, Marten Scheffer, Egbert H van Nes, Victor Brovkin, Vladimir Petoukhov, and Hermann Held. Slowing down as an early warning signal for abrupt climate change. *Proceedings of the National Academy of Sciences*, 105(38):14308–14312, 2008.

Vasilis Dakos, Stephen R Carpenter, William A Brock, Aaron M Ellison, Vishwesha Guttal, Anthony R Ives, Sonia Kéfi, Valerie Livina, David A Seekell, Egbert H van Nes, et al. Methods for detecting early warnings of critical transitions in time series illustrated using simulated ecological data. *PLoS ONE*, 7(7):e41010, 2012.

Christophe Diagne, Boris Leroy, Anne-Charlotte Vaissière, Rodolphe E Gozlan, David Roiz, Ivan Jarić, Jean-Michel Salles, Corey JA Bradshaw, and Franck Courchamp. High and rising economic costs of biological invasions worldwide. *Nature*, 592(7855):571–576, 2021.

John M Drake and Andrew M Kramer. Allee effects. *Nat. Educ. Knowl*, 3(10):2, 2011.

Jeffrey S Dukes and Harold A Mooney. Disruption of ecosystem processes in western north america by invasive species. *Revista chilena de historia natural*, 77(3):411–437, 2004.

Rebecca S Epanchin-Niell and Alan Hastings. Controlling established invaders: integrating economics and spread dynamics to determine optimal management. *Ecology letters*, 13(4):528–541, 2010.

Rebecca S Epanchin-Niell, Robert G Haight, Ludek Berec, John M Kean, and Andrew M Liebhold. Optimal surveillance and eradication of invasive species in heterogeneous landscapes. *Ecology letters*, 15(8):803–812, 2012.

Steven N Evans, Peter L Ralph, Sebastian J Schreiber, and Arnab Sen. Stochastic population growth in spatially heterogeneous environments. *Journal of mathematical biology*, 66(3):423–476, 2013.

Paul Fackler. MDPSolve: a MATLAB toolbox for solving markov decision problems with dynamic programming. `https://github.com/PaulFackler/MDPSolve`, 2011.

Neil Fenichel. Geometric singular perturbation theory for ordinary differential equations. *Journal of differential equations*, 31(1):53–98, 1979.

Crispin W Gardiner. *Handbook of stochastic methods: for physics, chemistry and the natural sciences*. Springer, 2004.

Fabio Gennaretti, Dominique Arseneault, Antoine Nicault, Luc Perreault, and Yves Bégin. Volcano-induced regime shifts in millennial tree-ring chronologies from northeastern North America. *Proceedings of the National Academy of Sciences*, 111(28):10077–10082, 2014.

Daniel T Gillespie. A general method for numerically simulating the stochastic time evolution of coupled chemical reactions. *Journal of computational physics*, 22(4):403–434, 1976.

Daniel T Gillespie. Exact stochastic simulation of coupled chemical reactions. *The journal of physical chemistry*, 81(25):2340–2361, 1977.

Albeter Goldbeter and Daniel E Koshland Jr. Ultrasensitivity in biochemical systems controlled by covalent modification: Interplay between zero-order and multistep effects. *Journal of Biological Chemistry*, 259(23):14441–14447, 1984.

Vishwesha Guttal and Ciriyam Jayaprakash. Spatial variance and spatial skewness: leading indicators of regime shifts in spatial ecological systems. *Theoretical Ecology*, 2(1):3–12, 2009.

Alan Hastings. *Population biology: concepts and models*. Springer Science & Business Media, 2013.

Alan Hastings and Louis Gross. *Encyclopedia of theoretical ecology*. Univ of California Press, 2012.

Alan Hastings and Derin B Wysham. Regime shifts in ecological systems can occur with no warning. *Ecology letters*, 13(4):464–472, 2010.

Alexandru Hening, Dang H Nguyen, and George Yin. Stochastic population growth in spatially heterogeneous environments: the density-dependent case. *Journal of mathematical biology*, 76 (3):697–754, 2018.

Crawford S Holling. Resilience and stability of ecological systems. *Annual review of ecology and systematics*, 4(1):1–23, 1973.

Werner Horsthemke and René Lefever. *Noise-induced transitions in physics, chemistry, and biology*. Springer, 1984.

Philip E Hulme. Invasive species challenge the global response to emerging diseases. *Trends in parasitology*, 30(6):267–270, 2014.

Gary R Huxel. Rapid displacement of native species by invasive species: effects of hybridization. *Biological conservation*, 89(2):143–152, 1999.

Carter L Johnson and Alan Hastings. Resilience in a two-population system: interactions between Allee effects and connectivity. *Theoretical Ecology*, 11(3):281–289, 2018.

Kaitlyn E Johnson, Grant Howard, William Mo, Michael K Strasser, Ernesto ABF Lima, Sui Huang, and Amy Brock. Cancer cell population growth kinetics at low densities deviate from the exponential growth model and suggest an Allee effect. *PLoS biology*, 17(8):e3000399, 2019.

Leslie Pack Kaelbling, Michael L Littman, and Anthony R Cassandra. Planning and acting in partially observable stochastic domains. *Artificial intelligence*, 101(1-2):99–134, 1998.

Yun Kang and Nicolas Lanchier. Expansion or extinction: deterministic and stochastic two-patch models with Allee effects. *Journal of Mathematical Biology*, 62(6):925–973, 2011.

Sonia Kéfi, Vishwesha Guttal, William A Brock, Stephen R Carpenter, Aaron M Ellison, Valerie N Livina, David A Seekell, Marten Scheffer, Egbert H van Nes, and Vasilis Dakos. Early warning signals of ecological transitions: methods for spatial patterns. *PLoS ONE*, 9(3):e92097, 2014.

Ann Kristin Klose, Volker Karle, Ricarda Winkelmann, and Jonathan F Donges. Emergence of cascading dynamics in interacting tipping elements of ecology and climate. *Royal Society open science*, 7(6):200599, 2020.

Tjalling C Koopmans. Stationary ordinal utility and impatience. *Econometrica: Journal of the Econometric Society*, pages 287–309, 1960.

Andrew M Kramer, Brian Dennis, Andrew M Liebhold, and John M Drake. The evidence for Allee effects. *Population Ecology*, 51(3):341–354, 2009.

Christian Kuehn. *Multiple time scale dynamics*, volume 191. Springer, 2015.

Hanna Kurniawati, David Hsu, and Wee Sun Lee. Sarsop: Efficient point-based POMDP planning by approximating optimally reachable belief spaces. In *Robotics: Science and systems*, volume 2008. Citeseer, 2008.

Steven J Lade, Susa Niiranen, Jonas Hentati-Sundberg, Thorsten Blenckner, Wiebren J Boonstra, Kirill Orach, Martin F Quaas, Henrik Österblom, and Maja Schlüter. An empirical model of the Baltic Sea reveals the importance of social dynamics for ecological regime shifts. *Proceedings of the National Academy of Sciences*, 112(35):11120–11125, 2015.

Brendon MH Larson, Brigitte Nerlich, and Patrick Wallis. Metaphors and biorisks: the war on infectious diseases and invasive species. *Science communication*, 26(3):243–268, 2005.

Timothy M Lenton. Tipping positive change. *Philosophical Transactions of the Royal Society B*, 375(1794):20190123, 2020.

Simon A Levin. Population dynamic models in heterogeneous environments. *Annual review of ecology and systematics*, pages 287–310, 1976.

Andrew Liebhold and Jordi Bascompte. The Allee effect, stochastic dynamics and the eradication of alien species. *Ecology Letters*, 6(2):133–140, 2003.

Andrew M Liebhold, Ludek Berec, Eckehard G Brockerhoff, Rebecca S Epanchin-Niell, Alan Hastings, Daniel A Herms, John M Kean, Deborah G McCullough, David M Suckling, Patrick C Tobin, et al. Eradication of invading insect populations: from concepts to applications. *Annual review of entomology*, 61:335–352, 2016.

David M Lodge, Paul W Simonin, Stanley W Burgiel, Reuben P Keller, Jonathan M Bossenbroek, Christopher L Jerde, Andrew M Kramer, Edward S Rutherford, Matthew A Barnes, Marion E

Wittmann, et al. Risk analysis and bioeconomics of invasive species to inform policy and management. *Annual Review of Environment and Resources*, 41:453–488, 2016.

Thomas E Lovejoy and Carlos Nobre. Amazon tipping point. *Science Advances*, 4(2):eaat2340, 2018.

Abhishek Mallela and Alan Hastings. The role of stochasticity in noise-induced tipping point cascades: a master equation approach. *Bulletin of Mathematical Biology*, 83(5):1–20, 2021a.

Abhishek Mallela and Alan Hastings. Tipping cascades in a multi-patch system with noise and spatial coupling. *Bulletin of Mathematical Biology*, 83(11):1–27, 2021b.

Abhishek Mallela, Maulik K Nariya, and Eric J Deeds. Crosstalk and ultrasensitivity in protein degradation pathways. *PLoS Computational Biology*, 16(12):e1008492, 2020.

MATLAB. *R2021a*. The MathWorks Inc., 2021.

Matias I Maturana, Christian Meisel, Katrina Dell, Philippa J Karoly, Wendyl D'Souza, David B Grayden, Anthony N Burkitt, Premysl Jiruska, Jan Kudlacek, Jaroslav Hlinka, et al. Critical slowing down as a biomarker for seizure susceptibility. *Nature Communications*, 11(1):1–12, 2020.

Robert M May, Simon A Levin, and George Sugihara. Ecology for bankers. *Nature*, 451(7181): 893–894, 2008.

Christian Meisel, Andreas Klaus, Christian Kuehn, and Dietmar Plenz. Critical slowing down governs the transition to neuron spiking. *PLoS Comput Biol*, 11(2):e1004097, 2015.

Vicenç Méndez, Michael Assaf, Axel Masó-Puigdellosas, Daniel Campos, and Werner Horsthemke. Demographic stochasticity and extinction in populations with Allee effect. *Physical Review E*, 99(2):022101, 2019.

James Murray and David King. Oil's tipping point has passed. *Nature*, 481(7382):433–435, 2012.

Roger M Nisbet and William Gurney. *Modelling fluctuating populations*. Wiley, 1982.

Howard T Odum and WC Allee. A note on the stable point of populations showing both intraspecific cooperation and disoperation. *Ecology*, 35(1):95–97, 1954.

Suzanne M O'Regan. How noise and coupling influence leading indicators of population extinction in a spatially extended ecological system. *Journal of biological dynamics*, 12(1):211–241, 2018.

Michael L Pace, Stephen R Carpenter, and Jonathan J Cole. With and without warning: managing ecosystems in a changing world. *Frontiers in Ecology and the Environment*, 13(9):460–467, 2015.

Nicholas F Polizzi, Michael J Therien, and David N Beratan. Mean first-passage times in biology. *Israel journal of chemistry*, 56(9-10):816–824, 2016.

Tracey J Regan, Iadine Chadès, and Hugh P Possingham. Optimally managing under imperfect detection: a method for plant invasions. *Journal of Applied Ecology*, 48(1):76–85, 2011.

Juan C Rocha, Garry Peterson, Örjan Bodin, and Simon Levin. Cascading regime shifts within and across scales. *Science*, 362(6421):1379–1383, 2018.

Marten Scheffer. *Critical transitions in nature and society*, volume 16. Princeton University Press, 2009.

Marten Scheffer. Foreseeing tipping points. *Nature*, 467(7314):411–412, 2010.

Marten Scheffer, Stephen R Carpenter, Timothy M Lenton, Jordi Bascompte, William Brock, Vasilis Dakos, Johan Van de Koppel, Ingrid A Van de Leemput, Simon A Levin, Egbert H Van Nes, et al. Anticipating critical transitions. *Science*, 338(6105):344–348, 2012.

Marten Scheffer, Stephen R Carpenter, Vasilis Dakos, and Egbert H van Nes. Generic indicators of ecological resilience: inferring the chance of a critical transition. *Annual Review of Ecology, Evolution, and Systematics*, 46:145–167, 2015.

Matthijs TJ Spaan and Nikos Vlassis. Perseus: Randomized point-based value iteration for POMDPs. *Journal of artificial intelligence research*, 24:195–220, 2005.

Allan W Stoner and Melody Ray-Culp. Evidence for Allee effects in an over-harvested marine gastropod: density-dependent mating and egg production. *Marine Ecology Progress Series*, 202: 297–302, 2000.

Steven Strogatz. *Nonlinear dynamics and chaos: with applications to physics, biology, chemistry, and engineering (studies in nonlinearity)*. CRC Press, 2015.

Samir Suweis and Paolo D'Odorico. Early warning signs in social-ecological networks. *PLoS ONE*, 9(7):e101851, 2014.

Yumi Tanaka, Jin Yoshimura, Chris Simon, John R Cooley, and Kei-ichi Tainaka. Allee effect in the selection for prime-numbered cycles in periodical cicadas. *Proceedings of the National Academy of Sciences*, 106(22):8975–8979, 2009.

Patrick C Tobin. Managing invasive species. *F1000Research*, 7, 2018.

Lev S Tsimring. Noise in biology. *Reports on Progress in Physics*, 77(2):026601, 2014.

Chengyi Tu, Paolo D'Odorico, and Samir Suweis. Critical slowing down associated with critical transition and risk of collapse in crypto-currency. *Royal Society open science*, 7(3):191450, 2020.

Ingrid A van de Leemput, Marieke Wichers, Angélique OJ Cramer, Denny Borsboom, Francis Tuerlinckx, Peter Kuppens, Egbert H van Nes, Wolfgang Viechtbauer, Erik J Giltay, Steven H Aggen, et al. Critical slowing down as early warning for the onset and termination of depression. *Proceedings of the National Academy of Sciences*, 111(1):87–92, 2014.

Erik A van Doorn and Philip K Pollett. Quasi-stationary distributions for discrete-state models. *European journal of operational research*, 230(1):1–14, 2013.

Nicolaas Godfried Van Kampen. *Stochastic processes in physics and chemistry*. Elsevier, 1992.

Robert C Venette and William D Hutchison. Invasive insect species: global challenges, strategies & opportunities. *Frontiers in Insect Science*, 1:1, 2021.

Vito Volterra. Population growth, equilibria, and extinction under specified breeding conditions: a development and extension of the theory of the logistic curve. *Human Biology*, 10(1):1–11, 1938.

Irina Vortkamp, Sebastian J Schreiber, Alan Hastings, and Frank M Hilker. Multiple attractors and long transients in spatially structured populations with an Allee effect. *Bulletin of mathematical biology*, 82(6):1–21, 2020.

WE Wallner. Global gypsy–the moth that gets around. In *Exotic pests of eastern forests conference proceedings*. US Forest Service and Tennessee Exotic Pest Plant Council, 1998.

Douglas J White. A survey of applications of Markov decision processes. *Journal of the operational research society*, 44(11):1073–1096, 1993.

C Wissel. A universal law of the characteristic return time near thresholds. *Oecologia*, 65(1): 101–107, 1984.

N Wouters, Vasilis Dakos, Martin Edwards, MP Serafim, PJ Valayer, and HN Cabral. Evidencing a regime shift in the North Sea using early-warning signals as indicators of critical transitions. *Estuarine, Coastal and Shelf Science*, 152:65–72, 2015.

Rong Zhou and Eric A Hansen. An improved grid-based approximation algorithm for POMDPs. In *IJCAI*, pages 707–716. Citeseer, 2001.